The Dissertation Committee for William D. Piñeros Gonzalez
certifies that this is the approved version of the following dissertation:

Novel Inverse Methods For Crystal Self-Assembly

Committee:

Thomas T. Truskett, Co-Supervisor

Dmitrii E. Makarov, Co-Supervisor

Ron Elber

Graeme Henkelman

Richard A. Jones

Novel Inverse Methods For Crystal Self-Assembly

by

William D. Piñeros Gonzalez

DISSERTATION

Presented to the Faculty of the Graduate School of

The University of Texas at Austin

in Partial Fulfillment

of the Requirements

for the Degree of

DOCTOR OF PHILOSOPHY

THE UNIVERSITY OF TEXAS AT AUSTIN

May 2018

To the fleeting, the irretrievable, the immaterial...

Acknowledgments

I would like to thank first and foremost my mother Gloria Gonzalez for providing continued support throughout all these long years of education. Without her hard work and dedication to my well being, none of this work would have been possible. Gracias por todo tu esfuerzo y sacrificio mamita. I also thank my siblings and other family members for their presence and moral support.

I would also like to acknowledge my adviser Thomas T. Truskett for having accomodated the unique circumstances of my graduate career and having provided his unwavering support throughout the lengthy doctoral process. In this light, I would like to acknowledge Avni Jain as well for having provided the necessary basis for prompt degree advancement. Additionally, I would like to acknowledge the many faculty and staff who have supported me through my education and whose confidence and guidance built the necessary foundation for productive personal growth. I acknowledge in particular those professors whose research, comments and feedback in my undergraduate years eased my start into research and graduate school.

Finally, I thank the people who have supported me in many ways, both material and immaterial, for these past few years, including Kyle K. G. Smith, Ryan B. Jadrich, and Beth A. Lindquist. Lastly, I acknowledge the

many steps, states, and circumstances that, for what it may, yield the present conclusion.

> You won't believe what happened. I saw a car with the license plate ARW 357. Can you imagine? Of all the millions of license plates in the state, what was the chance that I would see that particular one tonight? Amazing!
>
> -Richard P. Feynman

Novel Inverse Methods For Crystal Self-Assembly

Publication No. _____

William D. Piñeros Gonzalez, Ph.D.
The University of Texas at Austin, 2018

Supervisors: Thomas T. Truskett
Dmitrii E. Makarov

Inverse design methods are a promising new strategy to aid the discovery of materials with targeted properties. In this thesis, we employ two novel inverse design methods and apply it to the study of crystal self-assembly in two dimensions. In particular, we introduce a novel zero temperature (ground state -GS) analytical method and find effective interactions that stabilize targeted lattices by means of a constrained non-linear optimization. We demonstrate advantages of this new formulation by designing a square lattice to display increasing energetic differences over relevant lattice competitors and show that such constraints correlate with crystal thermal stability. However, these constraints also reduce density range representation of the target lattice in its phase diagram and suggests an inherent tradeoff in the constrained strategy. Having established a link between crystal property and constraint type, we design the snubsquare lattice by means of energetic constraints over close competitors and show this is in contrast to the design of the kagome lattice

which required no such constraints. We then test the limits of the GS method and design the open and challenging truncated square (TS) and truncated hexagonal lattices (TH). Unlike the previous targets, these lattices require the inclusion of a large pool of competitor micro-phases that greatly complicate optimization. Nevertheless, we show the system is still solvable by judicious use of constraints and decision variables.

Next, we use a novel relative entropy minimization approach (RE) and the GS method to explore the design space of particles interacting via a potential featuring a single attractive well. Specifically, we design a square, honeycomb and kagome lattice and show that we are able to infer a set of 'design rules' from generalities of the resulting interactions in both methods. We validate these rules by designing the challenging TS and TH lattices and show that optimized interactions readily promote target assembly from the fluid state. Finally, we expand the RE method to accommodate multi-component systems and inverse design a variety of crystal binary mixtures featuring triangular, square as well as other intricate and open motifs. We demonstrate how binary systems can help achieve equivalent single component structures but with simpler underlying interactions. Further, we analyze the binary assembly process and find that self interactions act as a 'primer' that place particles in the correct local positions while cross interactions, through system coupling, act as the 'binder' that lock particles into the correct binary structure.

Table of Contents

List of Tables

List of Figures

Chapter 1

Introduction

Manufacture of matter with specific constituent spacing and morphology below micrometer scales stands as a frontier challenge for next generation material design and application. While matter at the macroscale possesses constant, size-independent properties determined by the underlying chemical composition, particles with characteristic lenghtscales in the order of nanometers (e.g. colloidal systems) provide a novel way to design matter with emergent, functionalized material properties. [1–4] For instance, ultra-adhesive strength is achieved in gecko feet by nano-sized structural proteins that protrude and increase contact surface area. [5, 6] More technical possibilities arising from synthesic systems include novel applications as sensors [7–9], catalysts [10–12], filtration agents [13, 14], amongst other exotic mechanical or chemical applications. [1, 4] Additionally, the small lengthscales spanned by these systems lie in the order of visible light wavelength and can lead to potential novel uses as photonic band gap materials, luminescence enhancers and other important electronic or light mediated processes (e.g. plamonics). [15–19]

However, the promise of achieving many of these attractive material features is limited by the ability to engineer materials with the level of preci-

sion, ordering and uniformity required at these nanometer scales. While top-down fabrication techniques that can exert such direct manipulation of constituents to pre-determined configurations are currently available e.g. lithography, these are generally too slow and expensive for industrial wide-scale application. [20,21] Furthermore, the majority of these methods are limited to surface patterning and layer depositions, making the manufacture of desirable three-dimensional, isotropic materials highly challenging for scaled applications. [22] While new efforts are being introduced to overcome these difficulties, such as direct laser writing on sub-micron substrates, these methods still require multiple fabrication steps, can be substrate dependent, and overall pose similar complex limitations as standard lithographic techniques. [22,23]

Alternatively, self-assembly, or the spontaneous ordering of particles into well-ordered, stable structures with specified geometry and configuration, offers a promising solution in manufacturing materials at the desirable but challenging nanometer scale. In particular, colloidal systems are known to spontaneously arrange into well-ordered configurations as determined by underlying component interactions and environmental conditions. [1, 2, 24, 25] These interactions can be either of isotropic or anisotropic nature, and are usually mediated by component surface chemistry, solvent effects, component mixture as well as more general coulumbic, Van der Waals and entropic-driven (e.g. depletion) forces. [26–28] Moreover, assembly can be controlled externally by factors such as concentration gradients, applied magnetic or electric fields and temperature. [1,29] In this light, nano-particles provide a promising case

where advanced synthetic methods offer access to a large design space where constituents can be manufactured to great detail in composition, size, and molecular decoration. [30, 31] Furthermore, nano-particles can be tailored to display specific anistropic interactions by means of directional 'sticky' interactions, patchy surfaces [32–36] elongated morphology such as rods or stars [4], as well as other specific polyhedral core particle geometries (cubes, tetrahedrons, etc). [37–39] In addition to nano-particles, other comparable colloidal systems such as block-copolymers [40,41], dendritic polymers, etc. [28,42–44] can also be self-assembled into quasicrystals, ordered stripe phases, percolated networks and bilayered micelles that mimic better-known natural self-assemblying structures such as cell membranes. [3, 45–47]

Given the vast available design space in these colloidal systems, achieving effective design strategies that permit rational, predictive control over the self-assembly process is critical in linking structure-dependent properties into realizable materials. To this end one can consider a *forward* approach whereby realizable structures are discovered by intuition or combinatorial exploration in an Edisoninan, trial and error fashion. While this procedure provides an empirical route for feasible discovery, its passive nature undermines a directed design principle necessary for targeted material design. Instead, one can consider an *inverse* approach, whereby a desirable system property or structure is cast as an explicit design goal and solved via a constrained optimization problem of the system variables. [48–53] This approach can then reveal necessary system component or interactions to achieve the targeted system prop-

erties. [54–57] In this light, one can envision inverse design methodology as a means to uncover "design rules" of the system, and thereby provide a rational guide in manufacturing materials of desirable morphologies, functionality or other properties.

A classic example of an inverse design problem is the stabilization of specific crystal phases from pair-particle interactions at the ground (zero temperature) state. Specifically, one seeks to promote self-assembly of a targeted crystal phase by optimizing underlying tunable parameters $\boldsymbol{\theta}$ that determine the effective, isotropic particle interactions of a model pair-potential $\phi(r;\boldsymbol{\theta})$. Using this approach, workers have reported a wide variety of achievable structures such as square [58,59], honeycomb [59,60] kagome [61–63] in two dimensional systems, as well as simple cubic [64], wurzite [65] and diamond [64–66] for three dimensional lattices. Moreover, resulting pair potentials were shown to successfully promote target self-assembly in molecular simulations and calculated phase diagrams displayed rich poly-morphic lattices throughout its packing fraction range. [67] Additionally, it was demonstrated that designing a structure of lower dimensionality was able to yield interactions that stabilized equivalent, higher dimensional structures but at reduced computational cost. [59]

More generalized inverse designs methods are also possible with the use of so-called machine learning techniques. In this approach, the target property or structure is realized by optimizing parameters of some underlying physical model by means of statistical inference extracted from simula-

tion. [53, 68, 69] Recently this group introduced one such method via maximum likelihood derivation and showed it to be equivalent to a relative entropy coarse graining minimization problem (RE). [70–74] In RE, a desirable target phase is achieved by optimizing interaction parameters $\boldsymbol{\theta}$ directly from a molecular simulation framework. As such, RE optimization is an "on-the-fly" technique that directly ties parameter optimization to configurational statistics from a simulation. Furthermore, a succesful RE optimization ensures target self-assembly and automatically encodes against competing phases as it requires formation of the target structure directly from the fluid state. Indeed, RE has been successful in stabilizing a wide variety of two and three dimensional crystal phases [74, 75] including specific quasi-crystal or Frank-Kasper phases [76] and other more complex assemblies like fluid clusters and mesoporous phases [77, 78]. In this light, machine learning techniques such as RE demonstrate the power of statistically informed optimization and provide an additional tool in realizing rational designed systems.

Having briefly highlighted important inverse design methods and results, in this thesis we seek to expand on this body of knowledge and make use of novel inverse design methods to address important crystal design challenges. In particular, we introduce a novel analytical ground state method and make use of RE methodology to explore the following major themes in the corresponding chapters as elaborated below.

1.1 Novel ground state optimization for constrained inverse design

As discussed above, it is well known that optimizing particle interactions can achieve a desirable target structure at a specific state point. Less known is the extent that an interaction can also be explicitly optimized to stabilize the crystal over a wide density range in its phase diagram or alter its thermal stability. To what extent is it then possible to design phase properties of a target crystal given objective goals or specific constraints in the inverse design optimization? In order to answer this question, in chapter 2 we first introduce a novel analytical ground state problem in the form of a non-linear constrained optimization problem and show that it can be solved numerically using established gradient based methods. Using this improved method, we systematically design a square lattice to display increased energetic constraints over rationally selected lattice competitors and explore its resulting phase stability. We show that more heavily constrained optimizations lead to enhanced thermal stability of the target, but they also narrow its density range representation in the resulting phase diagram. We rationalize this trade-off as the result of sharpened interaction features that strongly favor target coordination shell positions at optimal values, but also rapidly penilize target densities for which these shells are placed away from their optimal position.

Having gained valuable insight in controlling target crystal phase stability, we show in chapter 3 that, using similar energetic constraints, it is possible to differentiate and stabilize targets with morphologically close competitors.

In particular, we contrast the design strategy used to stabilize a snubsquare lattice with that of a simpler kagome lattice. While the kagome lattice can be stabilized with a simple objective goal, snubsquare requires explicit energetic constraints over close competitors in order to achieve successful stabilization. Lastly, in chapter 4 we test the limits of our novel ground state method by designing the intricate and very open truncated square and truncated hexagonal crystal lattices. In doing so, we demonstrate that in addition to their inherent difficulty as low packing structures, we must also account for numerous competitor stripe micro-phases that greatly complicate the problem. However, judicious use of constraints prevent the problem from becoming intractable, and solutions yield interactions that succesfully promote assembly of the target structures.

1.2 Realizable two dimensional crystal structures from single well interactions

While most reported crystal design targets have been stabilized with a wide variety of pair-potential functional forms including multiple wells and strictly repulsive convex profiles, none do so with a potential featuring a single well profile. Understanding the single well interaction is an interesting problem due to its ubiquity in numerous experimental colloidal systems, in addition to its natural manifestation in atomic or molecular systems such as those described by the well-known Lennard-Jones potential. [79–82] As such, in chapter 5, we seek to characterize design properties of a single well in-

teraction and find a wide variety of crystal structures that can be stabilized by such potentials. In particular, standard square, honeycomb and kagome lattices are stabilized using the ground state method of chapters 2-4 as well as the "on-the-fly" RE method. Using these two very distinct and independent optimizations allows us to compare observed results for generalities. We show observed interaction features from both methods indeed reveal general similarities and allows us to postulate a set of "design rules" for single well interactions. We validate these rules by applying them in the design of the challenging truncated square and truncated hexagonal lattices and show the optimized interactions promote proper target assembly.

1.3 Inverse-design of multi-component systems

Virtually all the inverse design work presented so far deals exclusively with single component systems. While a varitety of experimental multi-component work, specifically binary mixtures, are reported to diversify and stabilize unique crystal structures in colloidal particles [83–86], relatively little is known theoretically for comparable multi-component systems. In particular, introducing two or more components expands the available parameter space and may allow to realize novel structures or simplify existing equivalent single component systems. As such, in chapter 6 we expand the power of RE methodology to include multi-component interactions and design a wide variety of unique and novel crystal morphologies. Specifically, we report nine binary structures featuring square and triangular motifs as well as more intricate and open crystals

featuring dodecagonal and octadecagonal motifs. We show how partitioning the sub-lattices of the global structure into separate components can simplify and stabilize otherwise equivalent and challenging single component systems. We also demonstrate how local component structure is driven by self interactions while the larger, overall assembly depends on coupled system interactions. Together, these results highlight the advantages inherent to inverse design principles.

Chapter 2

Breadth versus depth: Interactions that stabilize particle assemblies to changes in density or temperature

2.1 Introduction

Several recently introduced computational methods for inverse design focus on optimization of interparticle interactions to stabilize a targeted ground-state configuration with the assumption of an isotropic pair potential $\phi(r, \{\alpha_i\})$ with variable parameter set $\{\alpha_i\}$. Such approaches have found various interactions that stabilize two-dimensional square, honeycomb and kagome lattices [58, 60, 61, 63] as well as the three-dimensional diamond crystal structure. [65, 66] Furthermore, it was demonstrated that particles with the optimized interactions indeed assembled into the targeted lattice phases at higher temperature using molecular simulations [58, 60, 66].

In this same vein, the Truskett group have used inverse methods to design convex-repulsive, isotropic pair potentials of the following form [59, 64]

$$\phi(r/\sigma) = \epsilon\{A(r/\sigma)^{-n} + \sum_{i=1}^{2} \lambda_i(1-\tanh[k_i(r/\sigma-\delta_i)]) + f_{\text{shift}}(r/\sigma)\}H[(r_{\text{cut}}-r)/\sigma]. \tag{2.1}$$

that stabilize open crystal structures. The final optimized potentials qual-

itatively resembled effective pair interactions observed in various soft colloidal systems (e.g., star polymers, ligand-passivated nanocrystals, microgels, etc.). [28] Here, σ and ϵ represent characteristic length and energy scales respectively; H is the Heaviside function; $\{A, n, \lambda_i, k_i, \delta_i\}$ are variable parameters (i.e., α_i), one of which is fixed to ensure $\phi(1) = \epsilon$; $r_{\rm cut}$ is a cut-off radius; $f_{\rm shift}$ is a quadratic function $f_{\rm shift}(r/\sigma) = P(r/\sigma)^2 + Qr/\sigma + R$ added to enforce $\phi(r_{\rm cut}/\sigma) = \phi'(r_{\rm cut}/\sigma) = \phi''(r_{\rm cut}/\sigma) = 0$. Using a simulated annealing optimization approach, parameters for this potential that stabilize, over a very wide range of density, square and honeycomb lattices in two dimensions [59] as well as simple cubic and diamond ground-state structures in three dimensions were determined. [64] Complete phase diagrams were also calculated for the three-dimensional systems, [67] which illustrated rich and complex phase equilibria with the targeted assemblies exhibiting good thermal stability relative to other competing crystal lattices.

One basic question that has not yet been addressed is, which features of a pair potential would tend to maximize the melting temperature of a given target structure? Moreover, how would encoding high thermal stability into the interactions affect the corresponding range of densities for which the target structure is favored? In other words, is there a natural compromise between designing for robustness to changes in temperature versus volume? Such questions are challenging to answer directly via inverse methods because they would require incorporating full molecular simulations (for a wide range of model parameters and thermodynamic conditions) into the optimization problem, which

is computationally unfeasible at present. A pragmatic alternative is to search for features of the ground-state behavior that, while easier to compute than higher temperature properties, correlate with thermal stability of the target phase. In the present work, we find that placing constraints on the minimum chemical potential advantage that the target structure would exhibit over selected equi-pressure competing lattices at zero temperature helps determine optimized interactions with higher target-phase melting temperatures.

The specific structure that we target via ground-state inverse optimizations in this work is the two-dimensional square lattice ground state, which has attracted considerable theoretical interest in recent years, [59, 87–89] and the class of pair potentials we consider are those described by eq. 2.1. The stable equilibrium ground-state structure can be established by determining the global minimum of the potential energy U at fixed density and zero temperature or the minimum of the chemical potential μ at fixed pressure and zero temperature (amongst other possibilities that follow from classical thermodynamics [90]). Following other works, [59, 62, 64, 91] we adopt the latter fixed pressure framework for our optimizations for convenience because any coexistence between the target structure and another lattice also requires equality of pressure between phases. Through our optimizations, we test how the maximum achievable range of density for stability of the square-lattice ground state is affected by constraining the differences between its chemical potential at a prescribed state point and those of selected competing lattice structures at the same pressure. To do this systematically requires the solution of a series of

optimization problems, each utilizing different constraints. Given the considerable computational expense of using stochastic optimizers (e.g., simulated annealing, genetic algorithms, etc.) for even a single optimization, we instead formulate each optimization problem of interest as a constrained mixed-integer nonlinear problem, and we solve it numerically using the General Algebraic Modeling System (GAMS) [92]. We then explore the consequences of our imposed chemical potential advantage of the target ground state for the resulting thermal stability (i.e., melting temperature) of the resulting lattices.

2.2 Methods

In this section, we describe how we formulate and solve the inverse design problem of interest in this work: finding isotropic pair interactions that maximize the density range over which the targeted square lattice is the ground-state configuration given a constraint on its chemical potential advantage over selected competing lattices. We further detail the implementation of molecular dynamics (MD) simulation methods for estimating the melting point to characterize the corresponding thermal stability of the designed lattice structures.

2.2.1 Inverse Design of the Pair Potential

2.2.1.1 Optimization Problem Formulation

We formulate the design optimization problem following the general paradigm

$$\begin{aligned} \underset{\text{decision variables}}{\text{maximize}} \quad & f(\mathbf{x}) \\ \text{subject to} \quad & g_i(\mathbf{x}) \end{aligned}$$

where $f(\mathbf{x})$ is an objective function and $g_i(\mathbf{x})$ are constraint equality or inequality equations with variables $\mathbf{x}$. The mathematical forms of $f(\mathbf{x})$ and $g_i(\mathbf{x})$ define the type of problem to be solved (e.g., if integer variables or nonlinear functions are necessary, etc.). For the inverse design calculations of interest here, the set of equations g_i incorporate any desired constraints to be imposed on the interparticle pair potential and f is formulated to ensure optimization of the desired thermodynamic property. To optimize for specific ground states, one needs to consider not only the target lattice l_t of the design, but also other lattices $\{l\}$ that naturally compete with it for thermodynamic stability (the procedure to determine the pool of competing lattices is discussed separately in the next section). Using eq.(2.1) as the model pair potential, we ultimately seek potential parameters $\{A, n, l_i, k_i, d_i\}$ (i.e. the decision variables) that maximize the density range for which the target lattice l_t has a chemical potential lower than lattices in $\{l\}$ at the same pressure such that a minimum specified chemical potential advantage of the target structure over select competitors at a given state point.

Specifically, to incorporate the pair potential of eq.(2.1), we introduce constraint equations that ensure the potential is appropriately normalized, repulsive, convex, and continuous (we implicitly nondimensionalize energies by ϵ, lengths by σ and omit parameter notation below for brevity). The normality condition is given by

$$\phi(1) = 1 \tag{2.3}$$

and the other constraints are given by

$$\phi(\mathbf{r}) > 0 \tag{2.4a}$$

$$-\phi'(\mathbf{r}) > 0 \tag{2.4b}$$

$$\phi''(\mathbf{r}) > 0 \tag{2.4c}$$

and

$$\phi(r_{\text{cut}}) = 0 \tag{2.5a}$$

$$\phi'(r_{\text{cut}}) = 0 \tag{2.5b}$$

$$\phi''(r_{\text{cut}}) = 0 \tag{2.5c}$$

We set $r_{\text{cut}} = 2.27183$ as motivated by previous work considering square lattices designed via this potential form. [59] As a practical matter, $\mathbf{r}$ is discretized over a finite set of points in $(0, r_{\text{cut}})$; we use ten uniform points in $\phi(\mathbf{r})$, and 60 points distributed in a 1:6:5 ratio from ranges [0.2,0.8), [0.8,1.2], (1.2,r_{cut}) for $\phi''(\mathbf{r})$, which we find sufficient to enforce the constraints. It is not necessary to include the constraint on $\phi'(\mathbf{r})$ so long as the other constraints are fulfilled.

Next, we specify the equations describing the physics of the ground state. The first is for the internal energy per particle, which can be expressed

$$U_l = \frac{1}{2} \sum_{i}^{r_{i,l} \leq r_{\text{cut}}} n_{i,l} \phi(r_{i,l}(\rho_l)) \tag{2.6}$$

Here, $r_{i,l}(\rho_l)$ are the density-dependent coordination distances for each lattice l and $n_{i,l}$ are the number of neighbors at those distances. [93] The pressure P_l of lattice l is related to its density ρ_l by the virial expression

$$P_l = -\frac{1}{4} \rho_l \sum_{i}^{r_{i,l} \leq r_{\text{cut}}} n_{i,l} r_{i,l}(\rho_l) \phi'(r_{i,l}(\rho_l)) \tag{2.7}$$

For our purposes, the relevant density of a competing lattice l, ρ_l, is that which leads to equality of pressure with the target lattice l_t of density ρ_t. In other words $\rho_l(\rho_t)$ can be determined from knowledge of ρ_t via the relation $P_l(\rho_l) = P_t(\rho_t)$, and thus from eq. 2.7, we have

$$\rho_l \sum_{i}^{r_{i,l} \leq r_{\text{cut}}} n_{i,l} r_{i,l}(\rho_l) \phi'(r_{i,l}(\rho_l)) = \rho_t \sum_{i}^{r_{i,t} \leq r_{\text{cut}}} n_{i,t} r_{i,t}(\rho_t) \phi'(r_{i,t}(\rho_t)) \tag{2.8}$$

The chemical potential of a ground-state lattice l is, in turn, given by

$$\mu_l = U_l(\rho_l) + P_l(\rho_l)/\rho_l \tag{2.9}$$

Lastly, an auxiliary equation is used

$$r_0^2(\rho_l) \leq r_{\text{cut}}^2 \tag{2.10}$$

where $r_0(\rho_l)$ represents the nearest neighbor distance for competing lattices at density ρ_l. This helps tighten the optimization formulation by keeping density within a reasonable range.

An objective function $f(\mathbf{x})$ that fulfills our optimization goals must also be specified. We choose such an objective function to evaluate to a finite scalar value $f(\mathbf{x}) \to f$ and to be conducive to maximizing the range of densities $\Delta\rho_t = \rho_{t,f} - \rho_{t,i}$ for which the target lattice exhibits a chemical potential lower than that of the competing lattices. This is then defined as

$$f = \sum_{\rho_t} \prod_{l} H[\mu_l(\rho_l(\rho_t)) - \mu_t(\rho_t)] \tag{2.11}$$

where the sum is over discretized target lattice densities (each spaced a distance δ apart), $\rho_l(\rho_t)$ is computed from eq. 2.8, and H is again the Heaviside step function.

An additional constraint equation,

$$\min\{\mu_l(\rho_l(\rho_{t,o}))\} - \mu_t(\rho_{t,o}) \geq \Delta \tag{2.12}$$

is introduced to specify the *minimum* acceptable chemical potential difference Δ between the target lattice at an intermediate density point $\rho_{t,o}$ and selected competing lattices at the same pressure. Here, we use $\rho_{t,o} = 1.39$, which was found in an earlier study [59] to be in the middle of the density range of stability for a square lattice designed for $\Delta = 0$ and the same pair potential form. In practice, we have found that the post-optimization chemical potential difference between the target lattice and its closest selected competitor $\Delta\mu \equiv \min\{\mu_l(\rho_l(\rho_{t,o}))\} - \mu_t(\rho_{t,o})$ is approximately equal to the constraint Δ in all cases.

2.2.1.2 Numerical Solution Strategy

We implemented the optimization problem described above in GAMS [92], using the BONMIN [94,95] mixed-integer nonlinear programming (MINLP) solver with IPOPT [96] as the non-linear sub-solver. This choice of solver permits us to use integer valued functions such as in eq.(2.11) (i.e. the Heaviside function) as well as the remaining non-linear functions present in the potential and system physics formulation.

In practice, each optimization begins by inputting an initial guess for the pair potential parameter set that does not violate the constraints of eq.(2.3)-(2.5) and specifying a narrow target lattice density range $[\rho_{t,i}, \rho_{t,f}]$ containing $\rho_{t,o}$ to consider.

If the maximum attainable value of f is realized in the optimization (i.e the maximum number of feasible density points $\Delta\rho_t/\delta = (\rho_{t,f} - \rho_{t,i})/\delta$ is achieved), the boundaries of the density range are widened and the previously attained potential is used as the initial guess for a new optimization. This procedure is repeated until the optimization returns $f < \Delta\rho_t/\delta$, indicating that the maximum density range of stability for a given chemical potential constraint Δ was attained in the previous optimization. We carry out the optimizations described above for different values of Δ to explore how an imposed chemical potential advantage of the target lattice affects the maximum attainable $\Delta\rho_t$. As discussed in the results section, there is a maximum value of Δ above which a feasible solution does not seem to exist for any density range. While found values are not verifiably global due to the local nature of

the optimizer, they are optimal to the best of our efforts.

In addition to the explicit constraints described above, only pair potentials that result in mechanically stable target ground-state structures (as determined from phonon spectra analysis) were considered. Spontaneous assembly of particles interacting via the optimized potentials from the fluid state into the target structure upon temperature quenching was also verified at $\rho_{t,o}$ using Monte Carlo simulations (see supplemental material).

2.2.1.3 Competing Lattice Determination

In previous work done by the Truskett group on inverse design of targeted lattices, [59,64] pair potentials that simply maximized the density range of stability of the desired structure ($\Delta = 0$) were sought. For that type of optimization, it was necessary to choose a finite pool of competitive structures to compare with the target lattice, ideally those with the lowest values of chemical potential at the pressures of interest (which are not generally known in advance). The composition of this competitive pool was determined from an iterative procedure. An initial set of structures was selected (e.g., Bravais lattices plus a small number of non-Bravais lattices or tilings) based on intuition and knowledge obtained from earlier simulation studies on similar pair potentials. An optimization was then performed using the chosen competitive pool, followed by a forward calculation of the ground-state phase diagram with the optimized pair potential for densities in the targeted range. Any new structures that appeared were subsequently added to the previous competitive

pool, and a second optimization with the updated list of competitive structures was completed. This process–updating the competitive pool and optimizing the pair potential considering the expanded list of possible lattices found in forward calculations–was repeated until no new competing lattice structures emerged.

In the present study, we repeat similar optimizations but with the added requirement of a minimum chemical potential difference between the target and selected competitors. The hypothesis is that such a constraint will find potentials displaying enhanced thermal stability of the targeted phase. Note that one cannot enforce a fixed chemical potential difference between the target lattice and *all* possible competitors. To understand why, consider a representation of lattice structure defined by a set of primitive and basis vectors $\{v\}$. If $\{v\}$ can be modified continuously in some way (without adding or removing particles), e.g., by a set of suitable parameters $\{\Theta\}$, then $\{v(\{\Theta\})\}$ will then define a hyperspace of continuously connected lattices with the target structure l_t representing a specific point in this space. For ground-state systems of a given pair potential at a specific pressure, state quantities such as μ depend on the lattice structure (i.e. $\mu(\{v\})$) such that μ itself can be represented as a hypersurface of continuously connected lattices $v(\{\Theta\})$. Thus, one can always find structures in the neighborhood of the target lattice on the hypersurface with chemical potentials arbitrarily close to that of the target.

Considering this, it is clear that one cannot enforce a nonzero minimum chemical potential difference Δ between the target and *all* possible competi-

tive structures. However, one can meaningfully constrain the μ hypersurface in the optimization by enforcing a minimum chemical potential difference Δ between the target and a chosen set of lattices $\{l_g\}$ that define 'flag points' on the landscape. This helps achieve a standardized and well defined constraint depth that is feasible for the optimization. Indeed, a similar approach was introduced by Zhang et al for a related $\Delta\mu$ optimization and justified under similar premises. [62]

We provide an example for concreteness. The chosen target square lattice can be represented as a point in a larger Bravais subspace spanned by oblique primitive vectors $\{v_B(\{\Theta\})\}$ with $\{\Theta\}$ consisting of an aspect ratio b/a and primitive vector angle θ. Thus, the square lattice is represented by $v(1, \pi/2)$, while other Bravais lattices like the triangular lattice are given by $\{v(1, \pi/3)\}$ and so on. The corresponding $\mu(\{v\})$ landscape for this Bravais subset is then a function of $(b/a, \theta)$ (i.e. $\mu(\{v(b/a, \theta)\})$. The flag-point lattices we choose for enforcing the depth constraints here are the triangular lattice and a rectangular lattice which capture independent variations along the θ and b/a directions in the neighborhood of the target.[1] Similar subspace arguments can be made to account for elongated triangular (ET) and snub-square (SS) non-Bravais lattices, where the former can be transformed into square by a row-shift and the latter by a rotation of a single tile around its next neighboring square tiles. Other tilings or non-Bravais lattices can, in principle, be important for

[1]For an example of the resulting chemical potential hypersurface in a Bravais subspace, please see appendix F .

target lattice stability, but we did not find others that were relevant in the present square-lattice design problem.

Given the above considerations, our final competing pool consisted of lattices determined from the iterative forward procedure, some of which (those which naturally belonged to a subspace that continuously deformed into the square lattice) were also chosen as flag-point lattices. From the Bravais subspace, the final competing pool consisted of triangular, rectangular (REC) $b/a = 1.17$, and oblique (OBL) $b/a = 1.1$, $\theta = 1.09$ lattices, with triangular and REC also serving as flag points for the chemical potential constraint. Similarly, for the other relevant non-Bravais subspaces, the competitive pool included one SS lattice ($b/a = 1.0$) and three ET lattices ($b/a = 1.07$, $b/a = 1.20$, and $b/a = 1.23$), with all but the last ET lattice serving as flag points for the chemical potential constraint.

2.2.2 Melting Temperature Estimations

2.2.2.1 Z-method

The Z-method is a microcanonical molecular dynamics (MD) simulation strategy for estimating the melting point of a crystal that does not require free energy calculations. [97] The approach is based on the idea that a crystal remains metastable upon raising the temperature until it reaches its superheating limit, where it is hypothesized to have the same internal energy as the liquid at the equilibrium melting temperature T_m. The name is due to the fact that the estimate comes from the Z-shaped (zig-zag) graph that one

observes for the system in the temperature T vs pressure P plane as it transforms from the solid phase upon raising the energy at constant volume. It has been applied for a variety of model systems and has been repeatedly tested for both accuracy and variability. [98–100] For our purposes here, where we seek only estimates of melting temperatures to compare the widely varying thermal stabilities of targeted assemblies designed under various constraints, the Z-method provides an adequate guide.

Energy sweeps for the Z-method are carried out as follows. Initial particle positions are set in a perfect square lattice, and initial velocities are chosen from a random distribution and scaled to achieve a desired initial kinetic energy. For a series of progressively increasing energies, microcanonical MD simulation trajectories of $N = 1024$ particles (and a periodic square cell of length $V^{1/2}$ chosen to set $\rho = N/V = 1.39$) are initiated with a time step value of 0.001. After an initial pre-equilibration period at each energy, averages of static quantities like temperature T and pressure P are taken every 1000 time steps for at least 10^6 steps. Near the transition region, averages for liquid and solid properties are taken separately with the phase being determined by the translational order parameter τ

$$\tau(k) = \frac{1}{N} \sum_{i=1}^{N} \cos\left(\mathbf{k} \cdot \mathbf{r}_i\right) \tag{2.13}$$

Here, $\mathbf{r}_i$ denotes particle positions vectors and $\mathbf{k}$ is a reciprocal lattice vector. We chose $\mathbf{k} = \frac{2\pi}{l}(1, 1)$ for this purpose, where l denotes the lattice constant value at density ρ. We use $\tau \geq 0.5$ to indicate solid configurations and

$\tau \leq 0.1$ to denote liquid configurations. These assignments were additionally supported by monitoring the mean square displacement of the particles as a function of time.

Reported estimates of T_m are averages of the temperature of the superheating limit of the solid obtained from twelve independent energy sweeps.

2.2.2.2 Hysteresis method

As further corroboration of the estimates obtained from the Z-method described above, we also carry out melting point estimations by the hysteresis method. This method is based on analysis of superheating and supercooling processes in the framework of nucleation theory and validated through molecular dynamics simulations. [101,102] The basic approach is to carry out a simple heating and cooling sweep of the system near the melting point to determine the temperature of superheating T_+ and supercooling T_-. The melting point T_m is then estimated from

$$T_m = T_+ + T_- - \sqrt{T_+ T_-} \tag{2.14}$$

As such, we carry out Monte Carlo simulations in the canonical ensemble for $N = 400$ particles in a periodic square cell of length $V^{1/2}$ adjusted to fix density at $\rho = N/V = 1.39$. Simulations are started from the crystal phase and heated until melting is achieved. The system is then cooled from the liquid back into the crystal. The T_+ and T_- points are obtained from the resulting hysteresis loop in an energy vs temperature diagram.

2.3 Results and Discussion

Using our described ground state optimization procedure, we were able to obtain pair potential parameters for eq. 2.1 that satisfied all of our objective goals. That is, we found potentials that a) were convex repulsive, b) maximized the density range $\Delta\rho_t$ for which the square lattice is the stable structure and c) were such that the target at density $\rho_{t,o}$ displayed a specified minimum chemical potential advantage $\Delta\mu$ over the flag-point competitors (as elaborated in the methods section). The resulting relationship between $\Delta\rho_t$ subject to increasing values of $\Delta\mu$ for the optimized potentials is plotted in Figure 2.1.

As seen, there is a clear negative correlation between $\Delta\mu$ and $\Delta\rho_t$. While the exact values of $\Delta\rho_t$ may change based on the choice of non-linear subsolver (also given local nature of the solutions), test runs using a different subsolver showed values that yielded a very similar trend (not shown). In other words, there appears to be a clear compromise with this potential form between designing for high stability at a given density and designing for stability with respect to changes in density. There also appears to be a limit with this potential form to how stable one can make the square lattice ground state at $\rho_{t,o}$ relative to the flag-point lattices ($\Delta\mu \approx 0.23$). For instance, we were only able to find solutions consistent with larger $\Delta\mu$ than those shown in Figure 2.1 if we allowed the pair potential to violate the convexity constraint.

In terms of judging the overall quality of the optimizations, we can compare to one result from a previous study [59], where a simulated anneal-

ing algorithm was used to find parameters for the potential of eq. 2.1 that maximized the range of densities for which the square lattice was the stable ground-state structure (with no chemical potential constraint). In that paper, $\Delta\rho_t = 0.39$ was found for the optimized potential, which displayed a minimum chemical potential advantage of $\Delta\mu \approx 0.01$ over the flag-point lattices considered here. This can be compared to that of the potential obtained in this study with a $\Delta\mu = 0.01$ constraint, which exhibits a 50% wider density range, $\Delta\rho_t = 0.58$. While reported solutions are not verifiably global, the fact that such a large improvement in the objective function was obtained points to one of the advantages that the present rigorous framework has over heuristic optimization approaches like simulated annealing (a global optimizer in principle).

We now explore how features of the optimized interparticle potentials[2] help to explain the observed trade-off associated with designing for a large chemical potential advantage of the target ground-state structure at a given density versus designing for target stability over a wide range of density. In Figure 2.2, the pair potentials corresponding to $\Delta\mu$=[0.01-0.23] are shown. While no pronounced features can be expected for strictly convex-repulsive interactions, two important aspects of the potential do manifest. As $\Delta\mu$ increases, so does the steepness of the core repulsion (for $r \lesssim 0.8$) as well as the rate of radial decay towards the cut-off point (for $r \gtrsim 1.2$). The latter part can be seen more clearly in the log-log inset where intermediate features of core

[2]For a full list of potential parameter values, see appendix F

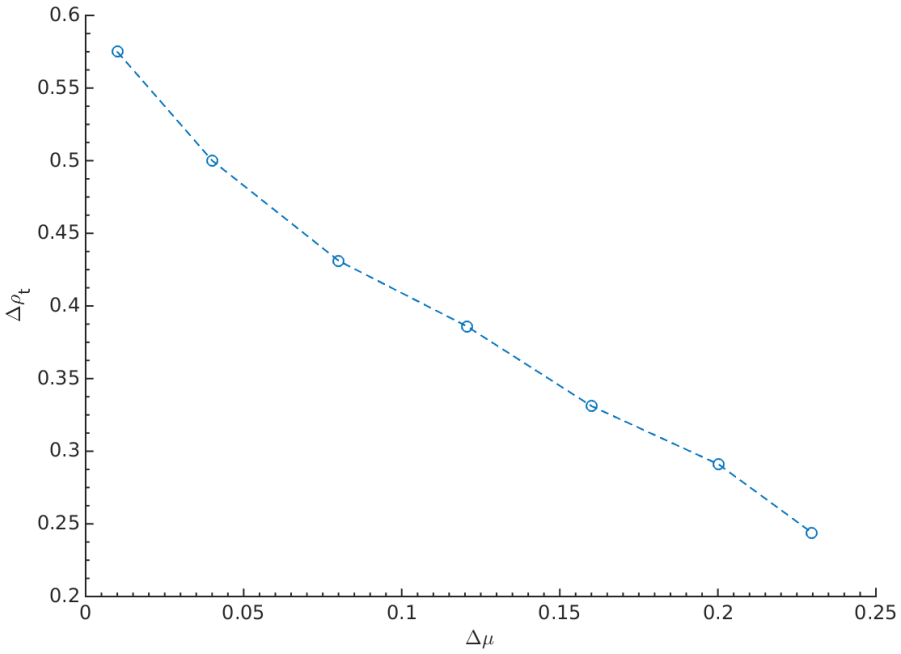

Figure 2.1: The width of the density range $\Delta\rho_t$ for which the square lattice is the stable ground-state structure for optimized parameters of the pair potential in eq. 2.1 versus the minimum chemical potential advantage $\Delta\mu$ of the square lattice ground state at $\rho_{t,o}$ over the flag-point lattices at that pressure. Blue circles indicate results using the MINLP solver BONMIN with IPOPT as the non-linear subsolver. Dashed lines are guides to the eye.

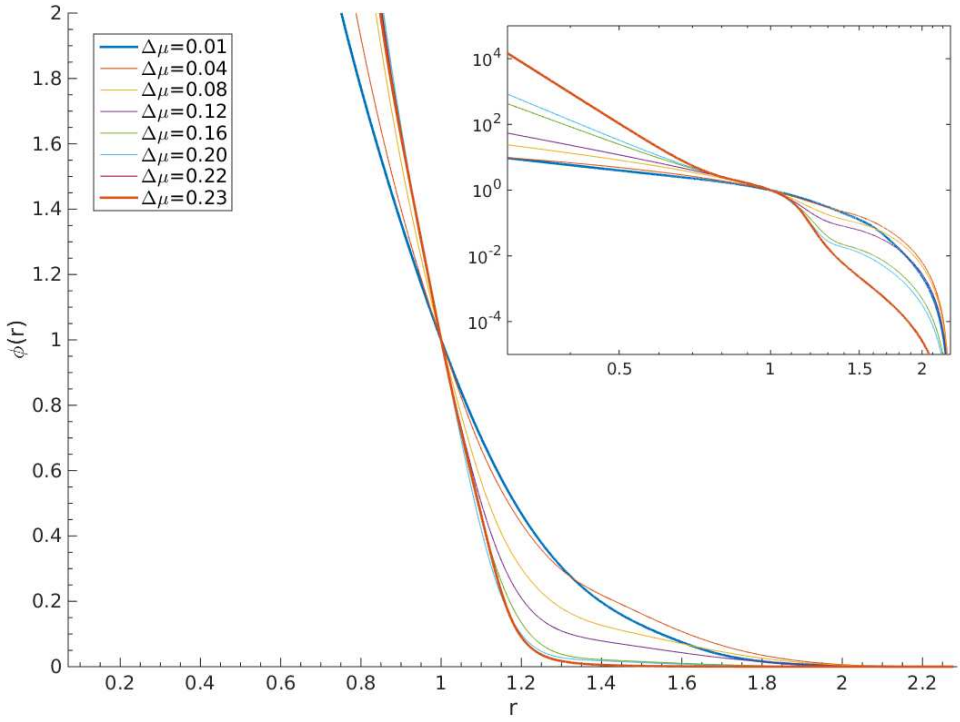

Figure 2.2: Optimized pair potentials $\phi(r)$ for different chemical potential constraints as a function of radial distance up to the cut-off at r_{cut}=2.27183. The inset shows a log-log plot of the same potentials.

repulsion and radial decay can be seen to lie approximately between the two extrema potentials corresponding to $\Delta\mu = 0.01$ and $\Delta\mu = 0.23$. As we discuss next, this sharpening of radial-dependent features with increasing $\Delta\mu$ is what provides the chemical potential advantage of the target over its competitors, but at the cost of target lattice stability at other densities.

To look closer into the relation between pair potential form and target stability, it is helpful to recall that the chemical potential expression for a ground state system is given as $\mu_l = U_l + P_l/\rho_l$. Using the energy and pressure expressions in (2.6) and (2.7), it is possible to recast this expression as

$$\mu_l = \sum_i^{r_{i,l} \leq r_{\text{cut}}} n_{i,l} \left[\frac{\phi(r_{i,l}(\rho_l))}{2} - \frac{r_{i,l}(\rho_l)\phi'(r_{i,l}(\rho_l))}{4} \right] = \sum_i^{r_{i,l} \leq r_{\text{cut}}} n_{i,l} \psi(r_{i,l}(\rho_l)) \tag{2.15}$$

where $\psi(r)$ has been defined as

$$\psi(r) \equiv \frac{\phi(r)}{2} - \frac{r\phi'(r)}{4} \tag{2.16}$$

As such, we see chemical potential depends not only on the pair potential but also on its gradient. Analyzing the radial dependence of $\psi(r)$ will thus help to understand how the various lattice coordination shells at their respective radial separations contribute to the chemical potential and how they bias the functional form of the optimized potentials leading to the observed negative correlation between $\Delta\mu$ and $\Delta\rho_t$.

We illustrate these points by plotting $\psi(r)$ for optimized interactions corresponding to the limiting cases of strongly ($\Delta\mu = 0.23$) and weakly ($\Delta\mu =$

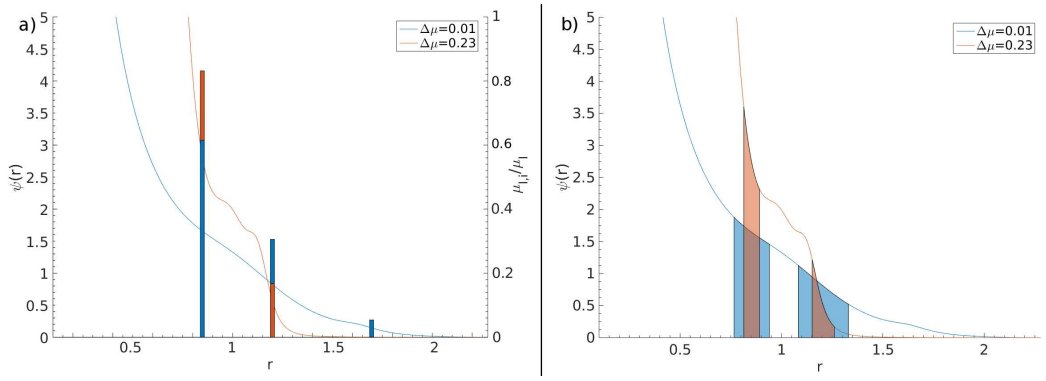

Figure 2.3: a) The function $\psi(r)$ of eq. 2.16 for optimized potentials with $\Delta\mu = 0.01$ (blue) and $\Delta\mu = 0.23$ (red), respectively. Bars indicate fractional contributions of each of the first three coordination shells to the total chemical potential for the square lattice at optimized density $\rho_o = 1.39$. Bars are located at the respective coordination-shell distances. The contribution for the third coordination shell of the $\Delta\mu = 0.23$ potential is not visible at this scale ($\sim 10^{-4}$). b) $\psi(r)$ for the $\Delta\mu = 0.01$ (blue) and $\Delta\mu = 0.23$ (red) optimized pair potentials. Shaded areas indicate the ranges of the first and second neighbor distances (from left to right respectively) of the target lattice for densities where it is the stable ground-state structure.

0.01) constrained chemical potential advantage of the square lattice ground state over the flag point structures. The plot in figure 2.3a) compares both $\psi(r)$ and the fractional coordination-shell contributions to the chemical potential of the square lattice for the two potentials. As can be seen, interactions obtained with the larger $\Delta\mu$ constraint impart greater emphasis on first-shell contributions that translate into potentials with harder cores and faster decays at these distances. These $\psi(r)$ features help the square lattice realize a lower chemical potential than the triangular lattice whose more densely packed first-coordination shell lies at a separation similar to that of the square lattice. Equally important is the shoulder-like region that decays between the square lattice's first and second coordination shells. The role of this shoulder is to destabilize the closely competitive rectangular and elongated triangular lattices that have second coordination shells at separations within the shoulder region[3] and thus contribute to their higher values of chemical potential compared to that of the square lattice.

The potential shape trends obtained from optimizations with the high $\Delta\mu$ constraint described above can be contrasted to the muted features that manifest when a smaller $\Delta\mu$ constraint is applied (which leads to considerably larger $\Delta\rho_t$). Shown in figure 2.3b) is also $\psi(r)$ for the two cases, but now presented along with shaded areas to indicate the range of first- and second-coordination shell distances of the corresponding stable square lattices. The

[3]For a list of $\mu_{l,i}/\mu$ values of selected lattice competitors shells up to the third coordination, see appendix F

key point is that small changes in coordination distances (due to changes in density) would have very different consequences for the chemical potential of the $\Delta\mu = 0.23$ system as compared to the $\Delta\mu = 0.01$ system due to their different forms for $\psi(r)$. For the $\Delta\mu = 0.23$ system, small changes in density and coordination distances will produce pronounced changes in $\psi(r)$ and hence the chemical potential. As a result, the specific shape that provided great chemical potential advantage for the square lattice at $\rho_{t,o}$ is no longer able to favor the structure at even modestly lower or higher densities. In contrast, the slower varying form of $\psi(r)$ for the $\Delta\mu = 0.01$ system, while providing reduced chemical potential advantage at $\rho_{t,o}$, is able to keep the square lattice stable over a wider density range. The inverse relationship in figure 2.1 emerges as a natural consequence of this trade off.

Moving on to understand how designing potentials for large $\Delta\mu$ for the square lattice ground state at $\rho_{t,o} = 1.39$ affects the thermal stability of the target structure, we use the Z-method and the hysteresis method to estimate the corresponding melting temperatures T_m at that density. As can be seen in Figure 2.4, the potentials optimized with larger $\Delta\mu$ constraints also show higher T_m irrespective of the estimation method. For instance, while the $\Delta\mu$=0.01 system has a melting point at around T_m=0.02, the melting point for the $\Delta\mu$=0.23 potential is approximately T_m=0.2–an order of magnitude greater. A slightly more pronounced but largely similar result is found from the hysteresis method ($T_m = 0.02$ to $T_m = 0.22$ at $\Delta\mu = 0.01$ to $\Delta\mu = 0.23$ respectively). Considering the $\psi(r)$ analysis presented above, this trend

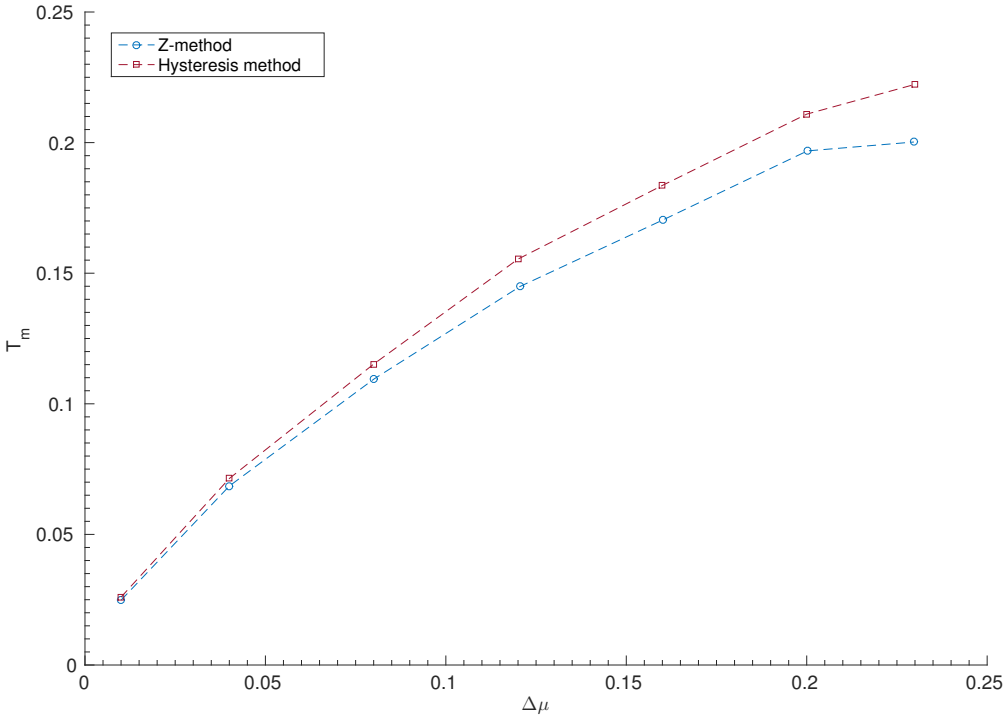

Figure 2.4: Estimated melting point of the targeted square lattice $\rho_{t,o} = 1.39$ as a function of the minimum chemical potential advantage $\Delta\mu$ of the square lattice ground state at $\rho_{t,o}$ over the flag-point lattices at that pressure. Results obtained from the Z-method and the hysteresis method, respectively. Temperature in units of ϵ/k. Dashed lines are guides to the eye.

makes intuitive sense. Potentials designed with larger $\Delta\mu$ constraints impose greater penalties to target lattice deformation, and hence a higher average energy is required to move particles from their perfect lattice positions. This apparently translates directly to a higher melting point for the structure. A similar argument can be made based on the discussion of the μ hypersurface in the methods section. Since $\Delta\mu$ captures an effective 'well depth' for the target structure, imposing higher $\Delta\mu$ has the effect of creating greater 'restoring forces' on the target (i.e. higher eigenvalues of the μ Hessian). [62] This results in increased mechanical stability at the ground state and a correspondingly higher melting point as shown here.

Finally, an important question arises when comparing back to Figure 2.1. Since we probed the melting points along a path where both 'range' ($\Delta\rho_t$) and 'depth' ($\Delta\mu$) change simultaneously, how does T_m change if we hold a particular depth constant and vary the range, or vice versa? From our discussion so far, we expect that depth alone will determine the thermal trend while the range will be largely inconsequential. Indeed, test runs where we probed systems with the same depth but different ranges yielded scatter around a mean value, whereas holding range constant and varying depth produced melting points consistent with 2.4 (not shown). Thus, for our inverse optimized pair potential, $\Delta\mu$ of the target in the ground state appears to strongly correlate with the thermal stability of the assembly, while the corresponding density range of stability has no such clear connection to the melting temperature.

2.4 Conclusion

We have used inverse methods of statistical mechanics to gain new insights into the trade-off between designing interactions for stability of a target structure with respect to changes in temperature versus density. Specifically, we have explored the consequences of constraining the minimum chemical potential advantage of a target square lattice ground state at a prescribed density $\rho_{t,o}$ over select competitors ($\Delta\mu$ or 'depth' on the μ landscape) while designing potentials that maximize the range of density where the target ground state is stable ($\Delta\rho_t$). The resulting constrained nonlinear optimization problem was solved numerically. For the isotropic, convex-repulsive pair interactions considered here, pair potentials designed with a larger $\Delta\mu$ constraint exhibited a narrower range of density stability $\Delta\rho_t$. The reasons for this compromise are apparent when examining the radially-dependent forms of the optimized pair potentials and their gradients. To enable high stability at a given density, features in the potential and its derivative must align with specific coordination shells to help produce the desired differences in chemical potential. When such features are present, however, the resulting target structures can lose stability with even modest changes in density.

We have also verified, via MD and Monte Carlo simulations, that potentials exhibiting ground states designed with larger $\Delta\mu$ constraints have higher melting temperatures at the target density. Preliminary tests further suggests that it is $\Delta\mu$ alone, and not $\Delta\rho_t$, that correlates with T_m. Both results are in accord with the idea that $\Delta\mu$ constraints ensure restoring forces on the μ

hypersurface that resist deformation (and ultimately melting) of the target structure.

2.5 Author Contributions

Work presented in this chapter was published in 2016 [103]. W.D.P carried out GAMS optimization, molecular simulations and performed analysis. M.B. provided original input into GAMS software and application. T.M.T designed and funded the research.

Chapter 3

Designing convex repulsive pair potentials that favor assembly of kagome and snub square lattices

3.1 Introduction

In the previous chapter, we introduced a novel ground state optimization strategy by formulating the problem as an analytical nonlinear program that can be solved numerically. Using this approach, we studied the consequences of designing interactions that stabilize the target structure over a wide density range while requiring that it maintain a minimum chemical potential advantage $\Delta\mu$ over select competing lattices. Interestingly, this chemical potential constraint led to the discovery of new interactions that increased target structure thermal stability (albeit at the expense of stability with respect to changes in density).

Here, we build on this optimization framework and consider two new and contrasting design targets for self assembly from particles with convex repulsive potentials: the kagome and the equilateral snub square lattices. While both target structures have been previously demonstrated to self-assemble using patchy particles [33, 36], polygons [39] or binary mixtures [104], this work is the first to address them using isotropic convex repulsive interactions in a

single component system. In particular, assembly of the kagome lattice is of interest in magnetic materials due to its unusual properties arising from geometrical frustration [105,106]. Materials exhibiting a kagome lattice are known to be difficult to synthesize experimentally, and though there are now a few isotropic model potentials known to stabilize this structure [61–63, 107], none of them are of the simple convex repulsive type considered here. Additionally, the kagome lattice presents an attractive design target for an isotropic potential in one respect: the spatial distributions of particles in its coordination shells are symmetric. In fact, we show here that one can design convex repulsive interactions that stabilize the kagome lattice ground state over a wide range of density, and that particles with these interactions readily self-assemble into the kagome lattice from the fluid upon cooling.

The equilateral snub square lattice, on the other hand, presents a significantly more challenging design target for an isotropic pair potential. First, the neighbors in the coordination shells surrounding each particle in this lattice have an asymmetric spatial distribution. The difficulties in stabilizing such asymmetric arrangements with an isotropic potential have been discussed previously in an insightful paper by Zhang et al., [62] and, to our knowledge, have yet to be overcome in a design application with an isotropic, convex repulsive pair potential. The second complication is that the snub square lattice is very similar to the elongated triangular lattice, sharing the same specific area at close packing and identical numbers of neighbors in the first two coordination shells (reminiscent of diamond and wurtzite lattices in three dimensions). Fi-

nally, the highly coordinated first shell of the snub square lattice (with five neighbors) also puts it in close competition with the common triangular lattice (with six neighbors). In this work, to successfully overcome these hurdles in designing interactions that assemble particles into the snub square lattice, we enforce a minimum chemical potential advantage of the target structure over select competing lattices during the potential optimization. We consider a weak and a strong constraint and find that, consistent to previous work of the last chapter, the latter leads to enhanced thermal stability of the designed snub square structure [103].

3.2 Methods

3.2.1 Inverse Design of the Pair Potential

The inverse design optimization we use here is formulated analytically as a nonlinear program in which one seeks parameters of the pair potential of Eq.2.1 that (1) make it convex repulsive and (2) maximize the range of density for which the target structure is the ground state (i.e., has lower chemical potential than equi-pressure competing lattices). This optimization can be cast in a way that also includes a constraint that ensures that the target structure, at a given density ρ_0, exhibits a minimum prescribed chemical potential advantage $\Delta\mu$ over those lattices in a select pool of 'flag-point' competing structures, a strategy shown in chapter 2 to enhance the target's thermal stability. Additionally, this analytical formulation offers solution strength and computing time advantages that are more difficult to achieve with familiar

stochastic approaches (e.g. simulated annealing, genetic algorithms, etc).

In the previous chapter, we considered the pair potential cut-off, r_{cut}, to be a fixed parameter. As such, we constrained the second derivative of the potential using the inequality

$$\phi''(\mathbf{r}) > 0 \tag{3.1}$$

where $\mathbf{r}$ was discretized as a fixed distribution of pair separations between 0 and r_{cut}. Here, we allow for r_{cut} to itself be a decision variable in the optimization that can vary between $r_{\text{c,min}}$ and $r_{\text{c,max}}$. Including r_{cut} as a decision variable allows the optimizer to use an additional degree of freedom to adjust near-feasible solutions to conform to our interaction constraints (i.e., normality and convexity). Additionally, having a r_{cut} as a decision variable ensures that the optimization has the flexibility to extend the pair interaction to include sufficient coordination shells to stabilize a desired target. Considering these advantages, we restrict Eq. 3.1 to apply between 0 and $r_{\text{c,min}}$, and then we add an equation,

$$\phi''(\mathbf{r}_v) > 0, \tag{3.2}$$

where $\mathbf{r}_v$ is represented by ten points evenly distributed between $r_{\text{c,min}}$ and $r_{\text{c,max}}$. More specifically, $\mathbf{r}$ in eq. 3.1 is evaluated at fifty points between 0 and $r_{\text{c,min}}$ distributed in an approximately 1:6:5 ratio from ranges $[0.3, 0.8)$, $[0.8, 1.2)$, and $[1.2, r_{\text{c,min}})$ (modified slightly as to best fit individual targets). This generalization reduces to the originally considered sixty fixed points in $\mathbf{r}$ if r_{cut} is assigned a constant value. For optimizations targeting the kagome lattice

with no $\Delta\mu$ constraint and the snub square lattice with the weak constraint $\Delta\mu = 0.01$, we assigned r_{cut} to constant values of 3 and 2, respectively. For the optimization targeting the snub square lattice with the strong constraint $\Delta\mu = 0.04$, we employed a variable r_{cut} from $r_{\text{c, min}} = 1.8$ to $r_{\text{c, max}} = 2.5$ and obtained an optimized value of $r_{\text{cut}} = 1.80082033$.

3.2.2 Competing Lattices

In carrying out pair potential optimizations, one compares the chemical potential of the target lattice to that of lattices in a small pool of competing structures. For our initial optimization, this competitive pool comprised Bravais and non-Bravais lattices which commonly occur in the phase diagram of two-dimensional systems with soft, repulsive interactions [103]. Once an optimized pair potential was obtained considering this initial competitive pool, a forward calculation was carried out to determine its ground-state phase diagram. Any new structures that appear in this phase diagram with chemical potentials comparable to the target lattice were added to the competitive pool, and a new optimization was performed. This procedure was repeated until no new competitive lattices were discovered in the forward calculation of the ground-state phase diagram for the optimized potential.

In order to design interactions with enhanced thermal stability of the target structure, potential optimizations can also be carried out with a constraint that enforces a minimum chemical potential advantage $\Delta\mu$ of the target at density ρ_0 over a small pool of equi-pressure lattices that serve as 'flag

points' on the μ hypersurface [103]. Ideally, one chooses flag-point lattices to be natural competing structures, some of which may be related to the target by a simple disturbance of the former's ideal configuration. More information and examples on how the choice of flag-point lattices for a given target might be determined are provided in the previous chapter.

For the present study, the final competing pools for different target structures are as follows, where an asterisk indicates a lattice is also used as a flag-point competitor for the chemical potential constraint. For the kagome target with no explicit $\Delta\mu$ constraint, the resulting competing lattices included elongated triangular, triangular, equilateral snub square, honeycomb, rectangular ($b/a = 2.01$), 'kagome-B' (i.e. a kagome with non-uniform aspect ratio), and distorted-honeycomb. Interestingly, twisted kagome, a related kagome structure by rigid rotation of the triangular motifs, did not arise explicitly as a competitor in the forward calculations but might prove necessary as a flag-point competitor in a $\Delta\mu$ constraint optimization. For the equiliateral snub square target for which a weak ($\Delta\mu = 0.01$) and strong ($\Delta\mu = 0.04$) chemical potential advantage constraint was enforced, the competing lattices included elongated triangular*, triangular*, honeycomb*, square*, elongated triangular* ($b/a = 1.15$), rectangular ($b/a = 1.17$), snub square ($b/a = 1.005$) and distorted snub square. For full details on kagome-B, distorted-honeycomb and distorted snub square lattices, please see Appendix A.

3.2.3 Monte Carlo Quenches

The assembly of target structures from the optimized potentials was tested via quenches from sufficiently high temperature fluid states in canonical Monte Carlo simulations utilizing periodic boundary conditions. We use implicit reduced units for all quantities.

For the kagome lattice, a system of $N = 1200$ particles and a simulation cell with dimensions adjusted to fix density at $\rho = 1.40$ were first equilibrated in the fluid state at $T = 0.023$ and then isochorically quenched in two steps: first to $T = 0.01$ and subsequently to $T = 0.005$. For the equilateral snub square forming potentials, similarly sized systems became kinetically trapped in defective structures during isochoric Monte Carlo quenches from the fluid, but smaller systems readily assembled into the designed target structure. For this lattice, we report results with $N = 64$ particles with simulation cell size adjusted to fix density to $\rho = 1.425$. The pair potential designed using the chemical potential constraint $\Delta\mu = 0.01$ could be equilibrated in the fluid state at $T = 0.0655$, and it was subsequently quenched to $T = 0.0309$ to induce assembly of the snub square lattice. The potential designed using the chemical potential constraint $\Delta\mu = 0.04$ exhibited a snub square structure with enhanced thermal stability, and thus the equilibration of the fluid state was carried out at the higher temperature of $T = 0.1$. For this system, assembly from the fluid state was observed in a two step quench, first cooling to $T = 0.482$ and then to $T = 0.0309$ to refine the structure.

3.3 Results and Discussion

Using the optimization strategy described in Section 3.2, we were able to find a convex repulsive potential $\phi(r)$ that maximized the density range $\Delta\rho$ for which the kagome lattice was the ground state with a value of $\Delta\rho = 0.415$. In one sense, this may not seem surprising. As alluded to in the Introduction, structures such as the kagome lattice with symmetric spatial distributions of particles in their coordination shells tend to be more amenable to stabilization with an isotropic pair potential. This favorable predisposition, however, does not guarantee the existence of a desired interaction form. In fact, Eq. 2.1 with optimized parameters provided in Tables 3.1 and 3.2 is, to our knowledge, the only purely convex repulsive pair interaction reported to stabilize the kagome lattice, and our ability to easily find it is a testament to the robustness of the design approach. The other pair potentials known to stabilize this structure do so via incorporation of other features at specific separations (e.g., attractive wells, concave shoulders, etc.) [61–63, 107], which may be more challenging to realize in practice.

How can a seemingly featureless convex repulsive pair interaction select a structure as specific as the kagome lattice over its competitors? As can be seen in Fig. 3.1a), the principal features of the designed kagome potential lie within the radial range of $0.5 \lesssim r \lesssim 2$, where it transits from a core ($r \lesssim 0.5$) into an approximately linear ramp (i.e. the force, $-\phi(r)'$ is nearly constant value at these points as shown by the dashed line in the figure). The implications of this form can be more clearly appreciated by considering a

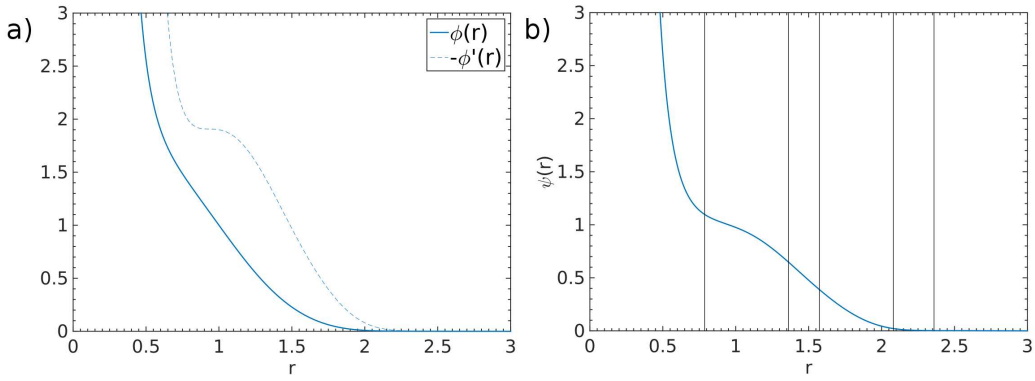

Figure 3.1: a) Pair potential $\phi(r)$ and force $-\phi'(r)$ of Eq. 2.1 with parameters optimized to maximize the range of density for which the ground state is the kagome lattice. b) Plot of $\psi(r)$ of Eq. 2.16 with kagome lattice coordination shell distances indicated by vertical black lines located for the optimization density $\rho = 1.40$.

function $\psi(r)$ which we previously showed in chapter 2 is related not only to the pair potential but also to the chemical potential of a ground-state lattice:

$$\mu_l = \sum_{i}^{r_{i,l}<r_c} n_{i,l}\psi(r_{i,l}(\rho_l)) \tag{3.3}$$
$$\psi(r) \equiv \frac{\phi(r)}{2} - \frac{r\phi'(r)}{4}$$

where $r_{i,l}$ denotes the i^{th} coordination shell distance for a lattice of type l at density ρ_l. In short, $\psi(r)$ helps understand what radially-varying 'weights' (due to the form of the pair potential) would multiply the occupation numbers $n_{i,l}$ in a given lattice l to determine the coordination shell contributions to its chemical potential μ_l.

A plot of $\psi(r)$ for the kagome potential is shown in Fig. 3.1b) at a density ($\rho = 1.4$) near the middle of the target lattice's stable range on the

Table 3.1: A, n and r_c parameters for the convex repulsive pair potential $\phi(r)$ of Eq. 2.1 found to maximize the density range for which kagome and equilateral snub square lattices are the ground states. SS-A and B refer to parameters for two snub square favoring potentials optimized with $\Delta\mu$ constraint values of 0.01 and 0.04, respectively.

	A	n	r_c
kagome	0.01978	5.49978	3.00000
SS-A	2.55737	1.53719	2.00000
SS-B	26.26595	1.75476	1.80082

Table 3.2: Same as table 3.1 but for the remaining l_i, k_i, d_i parameters.

	l_1	k_1	d_1	l_2	k_2	d_2
kagome	-0.06066	2.53278	1.94071	1.06271	1.73321	1.04372
SS-A	0.10022	6.24964	1.48785	0.15066	7.72221	1.12084
SS-B	1.00266	3.41639	1.52736	-13.85332	3.92417	0.68249

ground-state phase diagram. Perhaps the most prominent feature of this function is the shoulder that it exhibits for separations in the range $0.6 \lesssim r \lesssim 1.35$ before decaying to close zero by $r \sim 2.2$. In particular, this shoulder shape helps penalize the heavily coordinated first shell of competitors such as triangular and snub square lattice (6 and 5 neighbors respectively) throughout the kagome lattice density range by keeping the relative contribution from this shell nearly constant. Similarly, the decaying tail destabilizes more evenly spread shells from competitors like the rectangular lattice while making $\psi(r)$ small and smooth enough to diminish the contribution from the more heavily coordinated third shell in the kagome lattice (6 neighbors). Together, these features help establish the kagome lattice as the stable structure and explain

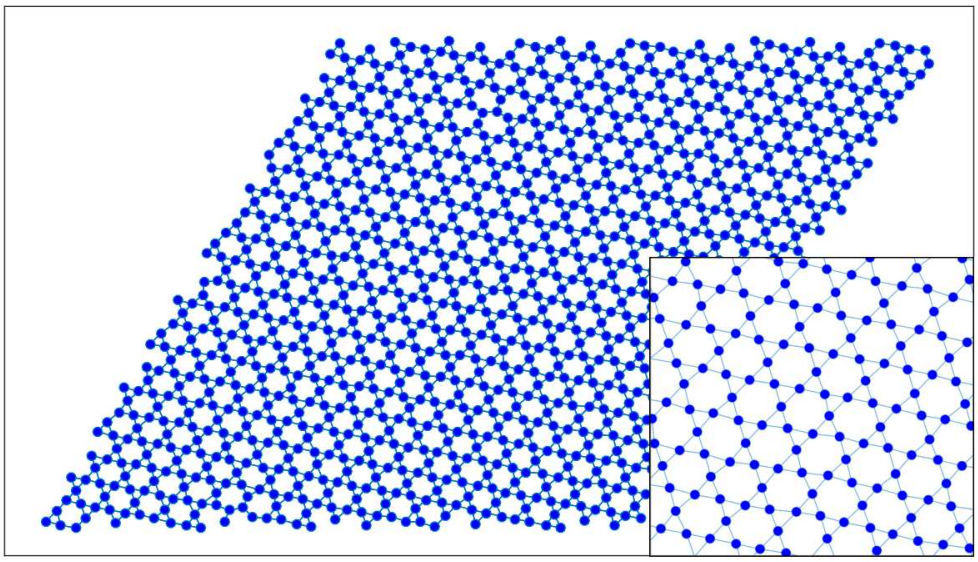

Figure 3.2: Configuration snapshot from a Monte Carlo simulation of a kagome lattice that self assembled from a fluid of the optimized potential (discussed in text) upon quenching to $T = 0.005$ at $\rho = 1.4$ Inset depicts a zoomed in view of a representative region. See Section 3.2 for simulation details.

the wide density range achieved as per our design goal.

To verify thermal stability of the kagome lattice with the optimized potential, we carried out Monte Carlo simulations (as described in Section 3.2) from the disordered fluid state for which the kagome lattice readily assembled upon quenching. In Figure 3.2, we show a representative configuration of the quenched structure. As can be seen, only very minor imperfections are present in the assembled kagome lattice, arising from the usual misalignment of the nucleated crystal relative to the periodically replicated simulation cell.

We can more concretely quantify the order displayed by the assembled

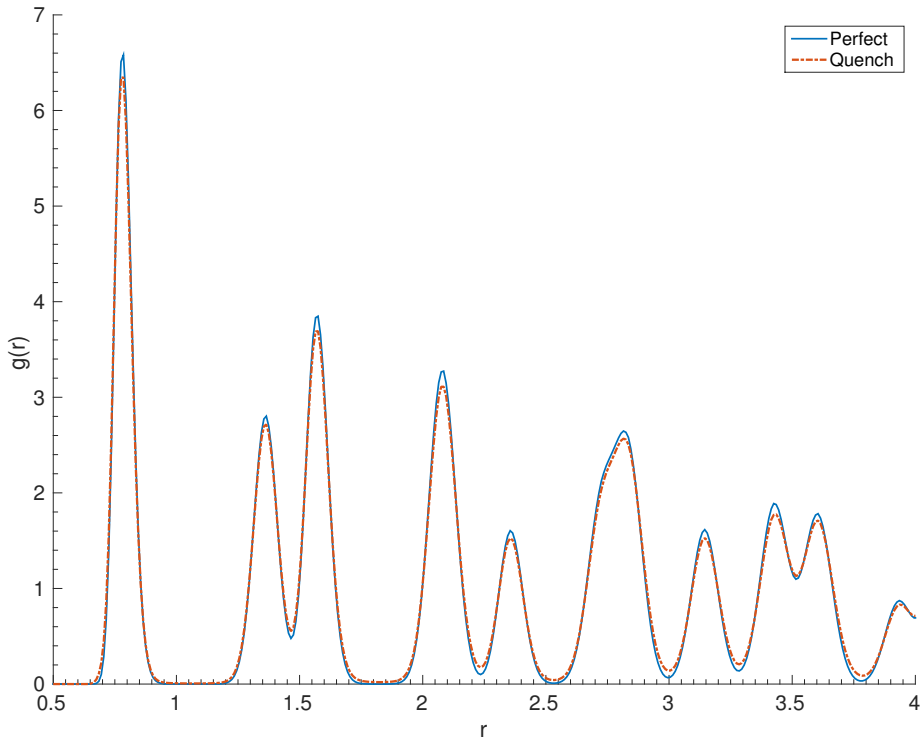

Figure 3.3: Radial distribution function of the perfect equilibrium kagome crystal (solid blue line) and the kagome crystal assembled from a fluid quench (dashed red) at $T = 0.005$.

kagome lattice by comparing its radial distribution function $g(r)$ to that of an equilibrated perfect crystal at the same temperature. As shown in figure 3.3, the quenched structure very nearly matches the perfect ordering in all coordination shells. Further supporting this observation, the potential energy difference between the quenched-assembled and equilibrated perfect crystal structures was less than 0.05%. Overall, these results show that our designed convex repulsive pair potential thermodynamically favors the kagome lattice, a structure which readily self assembles from the fluid state upon cooling.

Moving on to our next design target, we present results for the significantly more challenging equilateral snub square lattice. The inherent difficulty is discovering an isotropic pair potential, and especially a convex repulsive interaction, that can not only selectively lower the chemical potential of this target relative to similar triangular and elongated triangular lattices, but also stabilize the snub square structure despite the asymmetric spatial distribution of neighbors in its coordination shells.

As described in Section 3.2, to help ensure a significant free energy gap relative to competitors, we enforced a nonzero chemical potential advantage $\Delta\mu$ constraint for the target lattice over appropriately selected 'flag-point' lattices in the ground state. Additionally, considering previous results in chapter 2 where the severity of such a $\Delta\mu$ constraint correlated with the thermal stability of the designed target structure, we explored the behaviors of assemblies that resulted from optimizations with weak and strong constraints ($\Delta\mu = 0.01$ and $\Delta\mu = 0.04$, respectively). The potential parameters obtained from this

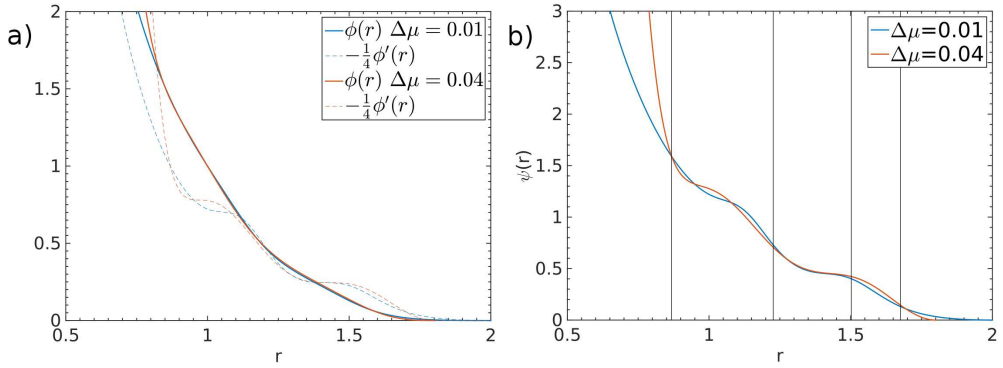

Figure 3.4: a) Pair potential $\phi(r)$ and force $-\phi'(r)/4$ (divided by four here to fit graph) of Eq. 2.1 with parameters optimized to maximize the range of density for which the ground state is the equilateral snub square lattice, subject to a chemical potential advantage constraint $\Delta\mu = 0.01$ (blue) and $\Delta\mu = 0.04$ (red) of the target structure over select 'flag-point' competitors. b) Plot of $\psi(r)$ of Eq. 4 for these pair potentials. Vertical black lines indicate snub-square lattice coordination shell distances at optimization density $\rho = 1.425$.

procedure are provided in tables 3.1 and 3.2. To our knowledge, these are the only isotropic and convex-repulsive interactions that have been reported to stabilize the equilateral snub-square lattice.

Considering the difference in constraints used to obtain these potentials, it is insightful to consider plots of optimized $\phi(r)$ and the corresponding auxiliary function $\psi(r)$ as shown in Figure 3.4. As can be seen in the potential plot (solid line), both pair potentials show a 'core' ($r \lesssim 0.8$) and a 'two-ramp' repulsion in the ranges $0.8 \lesssim 1.25$ and $1.25 \lesssim r \lesssim 1.65$ (i.e. near constant force–see dashed plots), respectively that together result in a two-plateau structure for $\psi(r)$. In analogy to the optimized kagome interaction, the first plateau is situated such that the target lattice's second coordination

shell falls after the first plateau, ensuring that the first coordination shell is more strongly weighted than more distant shells in the chemical potential. The second plateau also plays a critical role–It penalizes competing lattices relative to the snub square by creating a high value of $\psi(r)$ at distances corresponding to their third coordination shell, which raises the chemical potential of competitors with more third-shell neighbors (e.g., the triangular lattice has six neighbors in its third shell versus only one for the snub square lattice). Note also that the elevated $\Delta\mu = 0.04$ constraint led to steeper radial decays in $\psi(r)$ near the core and potential cut-off regions as well as sharpened plateau regions in comparison to the potential obtained with $\Delta\mu = 0.01$.[1] These trends are consistent with previous results on designing potentials to stabilize square lattices, where increasing the $\Delta\mu$ constraint led to similarly sharpened interaction features that more heavily penalized competing structures. Such features also led to enhanced target lattice thermal stability, which is consistent with our current results as we discuss next.

As detailed in Section 3.2, Monte Carlo simulations of particles interacting with these optimized pair potentials were able to assemble into the snub square lattice from the higher-temperature fluid. While larger systems displayed sluggish assembly kinetics, smaller systems readily assembled into the the designed structure. When compared at the same temperature, potentials designed with $\Delta\mu = 0.01$ and $\Delta\mu = 0.04$ showed structural differences

[1] See appendix B for a qualitative sensitivity analysis of the SS-A potential as a representative example

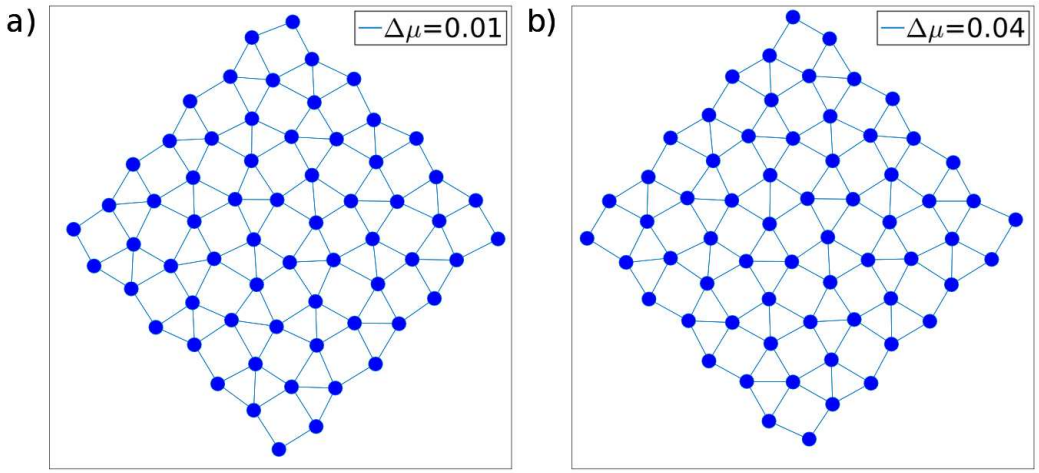

Figure 3.5: a) Configuration snapshots from Monte Carlo simulations of equilibrium snub square lattices that self assembled from the fluid upon quenching to $T = 0.0309$ at $\rho = 1.425$. Two cases, for pair potentials obtained via optimizations with chemical potential advantage constraints (a) $\Delta\mu = 0.01$ and (b) $\Delta\mu = 0.04$ of the target structure over select 'flag-point' competitors are shown and discussed in the text. See Section 3.2 for simulation details.

that point to enhanced thermal stability of the latter. As shown in Figure 3.5, assembled lattices of the potential designed with the stronger constraint (panel b) displayed less irregularity in the characteristic triangular and square tiling motifs than those with the weaker constraint (panel a).

These differences are better appreciated in the radial distribution functions for both potentials where significantly sharper resolution of coordination shells is achieved for the $\Delta\mu = 0.04$ potential as can be seen in Figure 3.6. This is poignant in the difficult to stabilize third shell of the snub square lattice where a *single* neighbor particle is expected to reside. This third shell neighbor corresponds to the third peak in the radial distribution, which as seen, is broader and somewhat overlapped with that of the fourth peak for the $\Delta\mu = 0.01$ potential, whereas it is well resolved for the $\Delta\mu = 0.04$ case. A similar trend likewise holds for longer range order ($r \sim 3$) where neighboring peaks coalesce for the $\Delta\mu = 0.01$ system, while they remain distinguishable for the $\Delta\mu = 0.04$ potential. Of course, peak resolution improves at lower temperatures for both potentials, but that this distinction can be observed for the higher temperature presented here ($T = 0.0309$) is a testament of the superior thermal stability obtained by the interaction designed with a higher $\Delta\mu$ constraint. Another indication is (naturally) the melting temperature itself, where the first melt temperature exhibited by the $\Delta\mu = 0.04$ interaction in Monte Carlo simulations was 23% higher than for the $\Delta\mu = 0.01$ potential for the same density (not shown). As expected from the previous chapter on designing square lattices, however, the trade off of this improved thermal stability was

the substantially reduced density range of stability for the ground state $\Delta\rho$, which was over four times lower for the $\Delta\mu = 0.04$ system as compared to the $\Delta\mu = 0.01$ potential (0.05 vs 0.23 respectively).

3.4 Conclusion

We have extended our recently introduced inverse design approach to find, to our knowledge, the first isotropic, convex repulsive pair potentials that favor assembly of two contrasting two-dimensional structures: the kagome and the equilateral snub square lattice.

The kagome lattice's symmetric distribution of neighbors in its coordination shells make it particularly amenable to stabilization by an isotropic potential. For this structure, we use our optimization framework to design a strict-convex repulsive pair potential that maximizes the density for which the target is the ground state. We find that particles interacting via this potential readily self assemble into a kagome lattice from the fluid state upon cooling in Monte Carlo simulations.

On the other hand, designing isotropic, convex repulsive pair potentials that favor the equilateral snub square lattice is more challenging due to the asymmetric distribution of neighbors in its coordination shells and the presence of several closely related competing structures. To help address these challenges, and thereby provide a significant free energy gap between the snub square lattice and competitors, we required that the target ground-state structure maintain a minimum chemical potential advantage $\Delta\mu$ over select com-

petitors during the parameter optimization. We find that, while larger systems of particles display sluggish assembly kinetics, smaller systems of particles interacting with the optimized potentials readily assemble into the snub square lattice from the fluid. As expected, based on previous work designing potentials for square lattices of chapter 2, a stronger $\Delta\mu$ constraint in the optimization led to enhanced thermal stability of the resulting snub square lattice but a significantly reduced density range for which it was the stable ground state.

3.5 Author Contributions

Work presented in this chapter was published in 2016 [108]. W.D.P carried out GAMS optimization, molecular simulations and performed analysis. M.B. provided valuable GAMS application access and feedback. T.M.T designed and funded the research.

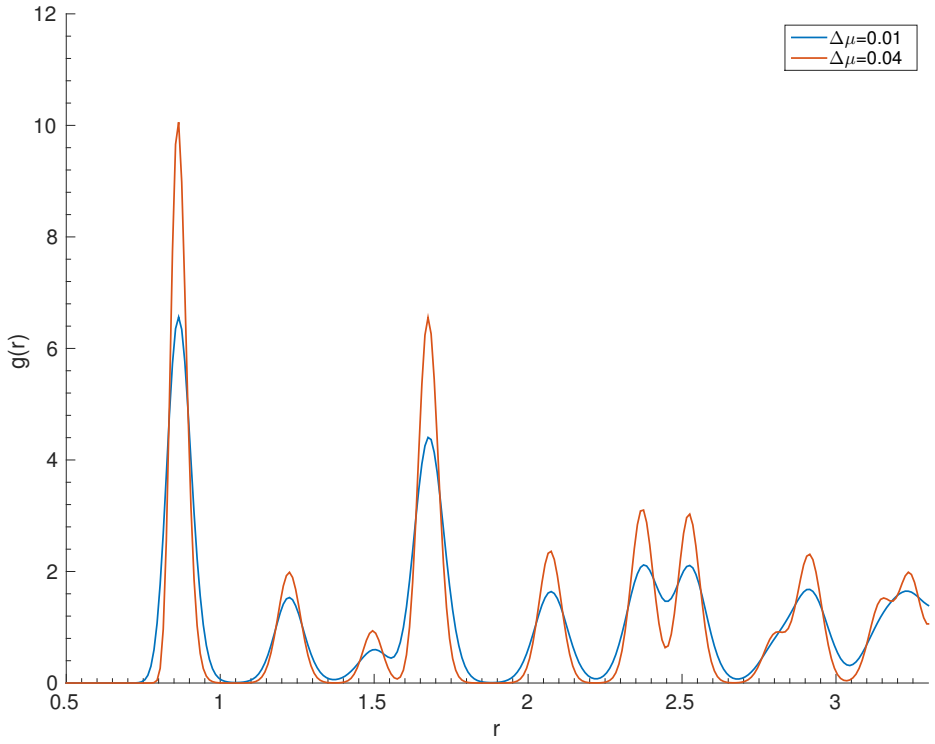

Figure 3.6: Radial distribution functions of equilateral snub square lattices that assembled from a fluid quench at $T = 0.0309$. The two cases shown are with pair potentials obtained via optimizations with chemical potential advantage constraints $\Delta\mu = 0.01$ (blue) and $\Delta\mu = 0.04$ (red) of the target structure over select 'flag-point' competitors. Both distributions have excellent agreement with those of their respective perfect equilibrium snub square crystals (not shown).

Chapter 4

Designing Pairwise Interactions that Stabilize Open Crystals: Truncated Square and Truncated Hexagonal Lattices

4.1 Introduction

In this chapter, we continue employing the ground state method introduced in chapter 2 to test the extent to which isotropic, repulsive pair potentials can be designed to stabilize ground states of particles organized in low-density periodic lattice structures (e.g. ordered porous morphologies). We further use Monte Carlo simulations to study whether particles interacting via the designed pair potentials can readily assemble into the target structures from the fluid following a rapid temperature quench. Porous materials such as these, more commonly stabilized by directional attractive interactions (e.g., physical 'bonds' between patchy colloids [33, 34, 39]), can find application in optical [15, 18, 20], chemical storage [13, 14], and separation [10] technologies. Thus, the discovery of new ways to assemble them from a wide variety of material building blocks and interaction types remains an active area of research.

The specific periodic structures that we focus on in this investigation are the 2D truncated square (TS) and truncated hexagonal (TH) lattices, which are characterized by central octagonal or dodecagonal motifs, respectively,

that resemble 'pores' of empty space within the matrix of surrounding lattice particles. The TH lattice exhibits one of the lowest packing fractions for a 2D close-packed system ($\eta \approx 0.39$) which is approximately half that of the close-packed square lattice and two thirds that of the close-packed honeycomb lattice; the packing fraction of the TS lattice is approximately 12% lower than that of the honeycomb lattice if the two are compared in their respective close-packed states.

4.2 Methods

4.2.1 Design Model

Our design model is framed around an analytical formulation of the inverse ground state problem for a target lattice in terms of constraints on the interparticle interactions [provided by form of the pair potential, $\phi(r;\{\alpha\})$] and an objective function choice. For this work, we define $\phi(r;\{\alpha\})$ as

$$\begin{aligned}\phi(r/\sigma) = \epsilon\{A(r/\sigma)^{-n} + \sum_{i=1}^{N_h} \lambda_i(1 - \tanh[k_i(r/\sigma - d_i)]) \\ + f_{\text{shift}}(r/\sigma)\}H[(r_c - r)/\sigma]\end{aligned} \tag{4.1}$$

where A, n,λ_i, k_i, d_i are design parameters (i.e. $\{\alpha\}$), N_h is the number of hyperbolic tangent terms used in the pair potential, H is the Heaviside function, r_c is the cut off radius, and $f_{\text{shift}}(r/\sigma) = P(r/\sigma)^2 + Qr/\sigma + R$ is a quadratic shift function added to enforce $\phi(r_c/\sigma) = \phi'(r_c/\sigma) = \phi''(r_c/\sigma) = 0$. In what follows, $N_h = 2, 3$ for the TS and TH lattice, respectively. We require $\phi(r/\sigma) > 0$ and $\phi'(r/\sigma) < 0$ to ensure a monotonically decreasing (i.e., purely repulsive) pair

potential which is flexible and can mimic the various soft-repulsive effective (i.e., center-of-mass) interactions that can be observed between, e.g., solvated star polymers, dendrimers, micelles, microgel particles, etc. Of course, additional (or simply different) constraints could be explored in future studies for designing assemblies of specific material systems. For notational convenience, we implicitly nondimensionalize quantities by appropriate combinations of ϵ and σ.

As described in detail in chapters 2 and 3 with interactions of this type, one can analytically formulate a nonlinear program whose numerical solution provides pair potential parameters that minimize the objective function $F = \sum_j(\mu_t - \mu_{l,j})$. Here, μ_t is the zero-temperature $[T = 0]$ chemical potential of the target lattice at a specified density ρ_0, and $\mu_{l,j}$ is that of an equi-pressure lattice j from a specified set of competitive 'flag-point' structures (discussed below); the sum is over all such flag-point competitors. In this work, we search for parameters that stabilize the target structure ground state over the widest range of density $\Delta\rho$, while ensuring a chemical potential advantage of the target relative to each flag-point competitor that is greater than a minimum specified threshold (here, we use $\mu_t - \mu_{l,j} \leq -0.01$). For specific information on the program formulation, including the equations used and their numerical solution using solvers consult chapter 2.

4.2.2 Competing Pool Selection

To use the strategy discussed above for designing a pair potential $\phi(r;\{\alpha\})$ that stabilizes a given target structure in the ground state, one first needs to establish a finite (preferably small) pool of the most competitive alternative structures at zero temperature and the same pressure. To do this, we adopt an iterative procedure. First, we carry out a preliminary optimization comparing the chemical potential of the target to others in an initial pool comprising a few select lattice and mesophase structures (e.g., stripes) known to be competitive for systems with isotropic, repulsive interactions. [103, 108] We then carry out a 'forward' calculation that considers more comprehensively equi-pressure competitors. For classes of competing structures that contain free parameters, the values of those parameters are determined by minimizing the chemical potential (using GAMS) under the optimized pair potential (for details see appendix A). Any structures that are revealed by this calculation to be more stable than the target lattice are added to the competing pool to be used in the next iteration of the pair potential optimization. This process is repeated until no new structures that closely compete with the target are found in the ground-state phase diagram calculation of the optimized potential.

Unlike for previous ground-state optimizations targeting denser structures, [59, 64, 103, 108] the structures within the competing pools for the low-density TS and TH lattices are too numerous to list in detail (totaling 60+). Instead, it is more insightful to consider competitors as general classes of stripe motifs with a variety of internal degrees of freedom. This is shown more clearly

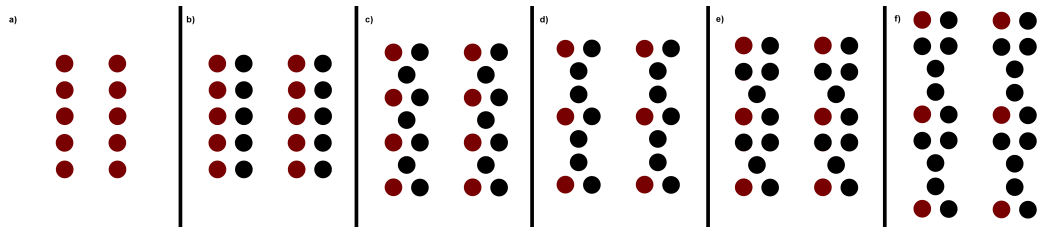

Figure 4.1: Competitor stripe classes schematic (a-f). Red particles denote repeating lattice cell and black particles any additional basis. Implicit in each class are numerous possible degrees of freedom, including inter-stripe distance, shears along stripe axis, as well as motif rotations and distortions. Together, these stripes with numerous internal degrees of freedom could be said to represent microphase competitors.

in schematic figure 4.1 where competitor classes are illustrated in each panel (a-f) and red particles represent fundamental lattice cells. For example, panel a) shows two stripes of particles separated by a given distance. Possible degrees of freedom include this separation distance as well as shears along the stripe axis, which in this case produce rectangular or oblique lattices. Panels b-f denote similar stripe-like classes, but now with increasing number of particles per cell (black particles) and more specific motifs. Relevant degrees of freedom here include the distance between stripes, shears along the stripe axis, but also more specific possibilities (e.g., motif distortions or rotations). Altogether, these six classes represent stripe microphases that constitute most of the strong competitors found for both design targets of this study. In what follows, we list the final competitor pools for each target as a tally of competitors belonging to each class as well as any general or specialized competitor not included in this set.

For the TS lattice target, the final pool of competitors included the following standard periodic lattices that are *not* part of the aforementioned stripe classes: square, hexagonal[1], honeycomb, snub square, snub trihexagonal, and distorted kagome (2 competitors). The 'stripe-class' competitors for the TS lattice included four structures from class a), three from class b), five from class c), four from class d), and one from class e). For the TH target, the non-stripe class competitors included the following standard lattices: square, hexagonal, honeycomb, snub trihexagonal, TS, and snub square with aspect ratio $b/a = 1.8$. The stripe-class competitors for the TH lattice included seven structures from class a), seven from class b), seven from class c), five from class d), and seven from class f). Additionally, two specialized competitors arose for the TH lattice; one was a cluster of five particles repeating across an open oblique lattice (figure G.1) and another was an open decagonal motif with a particle in the center (figure G.2).

Finally, note that while all competitors were ensured to have chemical potentials greater than those of the target with the optimized interactions, only representative members of each stripe class and other lattices (so-called 'flag-point' lattices of previous chapters) can be effectively used in objective function evaluations for this formulation and in ensuring the minimum required chemical potential advantage of the target described above. For these targets, the particular identity of a stripe class flag-point competitor is not too

[1]While square and hexagonal could be said to belong to class 1 stripes as per our chart, these standard lattices are sufficiently common and important to be listed separately by name for clarity

important as long as the overall flag-point set spans one member of each class. On the other hand, standard lattices (e.g. hexagonal) or uniquely specialized competitors like the decagonal motif structure for TH or snub trihexagonal for TS enter directly as flag-point competitors by default.

4.2.3 Monte Carlo Simulations

To explore the feasibility of self assembly from fluids of particles interacting via the optimized pair potentials, Monte Carlo simulations were carried out in the canonical ensemble as follows. For the potential optimized for the TS lattice, a system of $N = 100$ particles (in a periodically replicated simulation cell with dimensions chosen to fix the number density, $\rho_0 = 1.03$) was isochorically heated to a high temperature, melting the perfect crystal to form a fluid. The fluid was then isochorically quenched from high temperature back to a crystal at $T = 0.0091$. The crystal was then further cooled to $T = 0.005$ for structure refinement and computation of the radial distribution function. For the potential optimized for the TH lattice, a system of $N = 96$ particles (in a periodically replicated cell with dimensions set to fix $\rho_0 = 1.075$) was melted from the perfect crystal to form a fluid. Two dozen identical fluid configurations were seeded with a small frozen crystal of 21 particles pinned into perfect lattice positions. These configurations were then quenched from high temperature to $T = 0.06$ over 4 million Monte Carlo steps. For systems displaying assembly of the target structure, the seed particles were subsequently unpinned, and the whole system was allowed to relax for $90,000$ Monte Carlo

steps for computation of the radial distribution function.

4.3 Results and Discussion

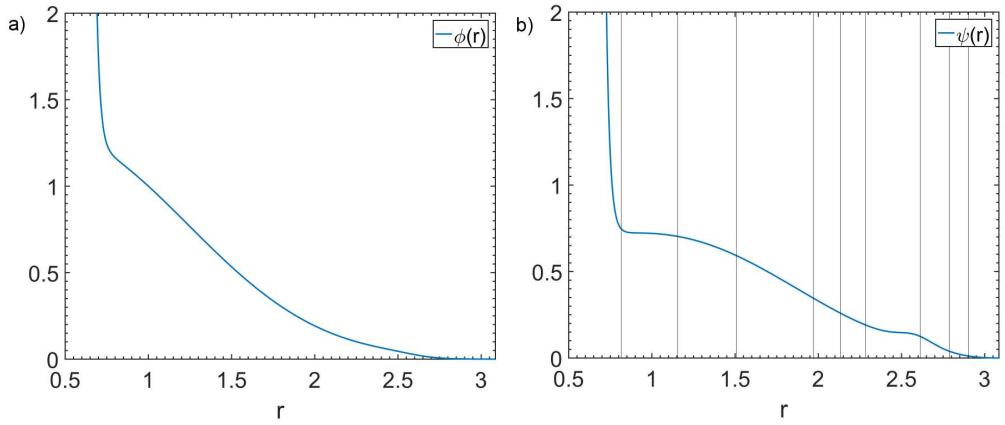

Figure 4.2: a) Repulsive pair potential $\phi(r)$ designed to stabilize the TS lattice as the ground-state structure, and (b) $\psi(r)$ obtained from $\phi(r)$ via eq. 4.2. Black vertical lines indicate positions of the first nine coordination shells of the TS crystal at the midpoint of its stable density range ($\rho = 1.03$). The parameters of the optimized pair potential are presented in tables G.1 - G.4 of appendix G

.

Using the problem formulation described in section 4.2, we were able to solve for parameters of the monotonically decreasing pair potential $\phi(r)$ (given by eq. 4.1) that maximize the density range over which the TS lattice is the stable ground state structure (here, $0.98 \leq \rho \leq 1.08$), while also ensuring that the ground state exhibits, at $\rho_0 = 1.03$, a chemical potential advantage of at least $\Delta\mu = 0.01$ over equi-pressure flag-point competitors. Importantly, the latter ensures a significant free energy separation of the target from var-

ious closely competing stripe microphases. The resulting pair potential $\phi(r)$ is shown in figure 4.2a, and the list of optimized potential parameters is provided in tables G.1 - G.4 of appendix G. As can be seen, $\phi(r)$ has a simple, ramp-like form with a steeply repulsive core at $r \sim 0.7$. This is interesting because particles interacting via a similar hard-core plus linear-ramp repulsion are known to exhibit rich ground-state behavior as a function of density and the parameters of the pair potential, [87, 88] displaying a variety of periodic crystalline structures (including some with nonequivalent lattice sites or multiple particles per unit cell) as well as a random quasicrystal.

As discussed in detail in previous chapters, to understand the stability of ground-state structures, it is helpful to consider the function $\psi(r)$

$$\psi(r) \equiv \frac{\phi(r)}{2} - \frac{r\phi'(r)}{4} \tag{4.2}$$

which determines the zero-temperature chemical potential μ_l of lattice l via the relation $\mu_l = \sum_i^{r_{i,l}<r_c} n_{i,l}\psi(r_{i,l}(\rho_l))$, where $r_{i,l}$ denotes the i^{th} coordination shell distance for that lattice at density ρ_l. In short, $\psi(r)$ quantifies the radially-varying 'weights' (due to the form of the pair potential) that multiply the occupation numbers $n_{i,l}$ in a given lattice l to determine the coordination shell contributions to its chemical potential.

A plot of $\psi(r)$ is shown in figure 4.2b with vertical black lines corresponding to the first nine coordination shell positions of the TS crystal at the midpoint of its stable density range $\rho = 1.03$. As seen, $\psi(r)$ displays two characteristic plateau features: the first for separations in the range $0.7 \lesssim r \lesssim 1.3$

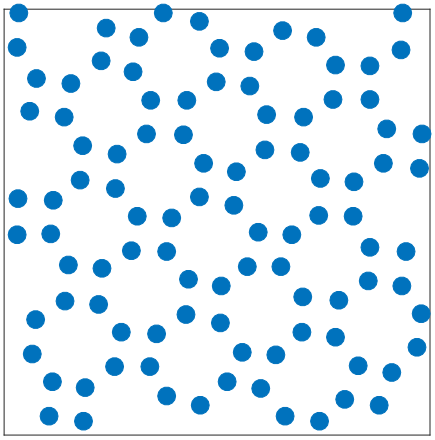

Figure 4.3: Monte Carlo simulation configuration for a system of particles interacting via the potential optimized for the TS lattice at $T = 0.005$ and $\rho_0 = 1.03$. As described in the text, this lattice self-assembled upon isochoric quenching to these conditions from a high temperature fluid.

and the second for $2.4 \lesssim r \lesssim 2.7$. The function of these plateaus can be qualitatively understood as follows. The first plateau helps to destabilize standard Bravais and non-Bravais lattices (e.g., hexagonal and snub square patterns) which have relatively high coordination numbers (six and five in the first shell, respectively)–and, hence, higher contributions to the chemical potential–at these distances. The second plateau helps destabilize more closely related competitors that otherwise share or closely track the coordination shells of the TS lattice. For instance, the seventh shell of the target TS lattice is positioned right at the point where the second plateau starts to decrease ($r \sim 2.6$) so that related shells for many of the stripe competitors at slightly smaller separations are destabilized more harshly. Lastly, the strongly repulsive 'core' serves to

destabilize competitors whose first shell is at a shorter distance than that of the TS lattice. Despite these features, note that the resulting $\psi(r)$ is still relatively smoothly varying, which–as discussed in previous chapters–is consistent with a target designed to display stability over a broad density range.

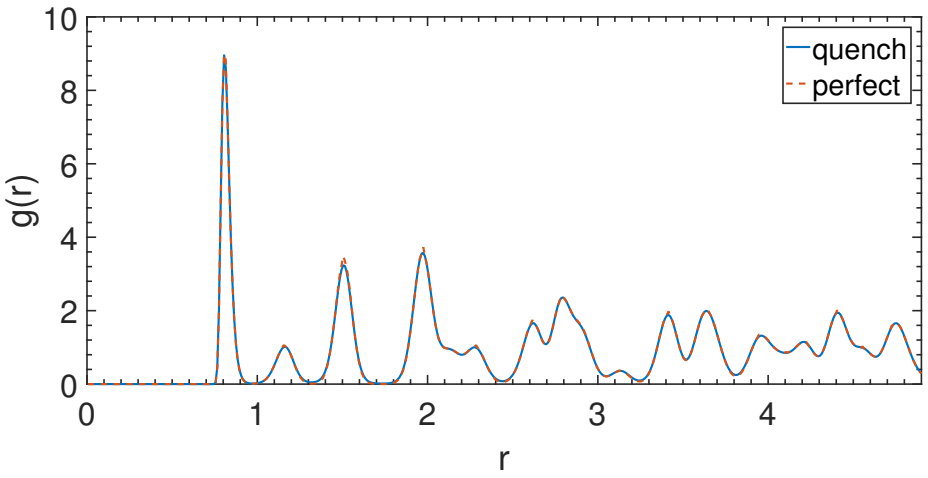

Figure 4.4: Radial distribution function $g(r)$ for the TS lattice at $T = 0.005$ and $\rho_0 = 1.03$: (solid blue line) assembled via quenching from a high temperature fluid and (red dash line) equilibrated starting from the perfect lattice configuration.

Carrying out Monte Carlo simulations of particles interacting via the optimized pair potential as described in section 4.2.3, we verify the TS crystal can indeed readily assemble from the fluid phase upon isochoric cooling. A representative configuration of the assembled structure is displayed in figure 4.3, showing that–aside from the usual minor defects due to the misalignment of the crystal and the boundaries of the periodically replicated simulation cell–a near defect-free TS lattice is obtained. The quality of the assembly is

characterized more systematically (see figure 4.4) by comparing the radial distribution function $g(r)$ at the final temperature of the quench to that of an equilibrated crystal initiated from the perfect configuration at that temperature. As can be observed, $g(r)$ of the assembled system matches well with that of the equilibrium crystal. Note in particular the well resolved second peak, a shell where just a single neighbor is expected to reside. The fact that the assembled structure accurately captures it highlights the robustness of the optimized interactions.

The second target structure considered in this study, the TH crystal, provided a significantly more difficult design challenge. Despite the fact that the underlying structural motif of the TH lattice is similar to that of the TS lattice (see discussion below), we found that solution of the design problem for the more open TH lattice required consideration of nearly 50% more competing structures as well as a more flexible pair potential (i.e., inclusion of a third hyperbolic tangent term in eq 4.1). While the pair potential $\phi(r)$ obtained from the optimization indeed stabilizes the TH crystal ground state, it does so only over a very narrow density range ($1.07 \leq \rho \leq 1.08$) and by assuming a more complex repulsive form (see figure 4.5a and the associated parameters in tables G.1 - G.4 of appendix G). Note for instance the presence of two step-like features in $\phi(r)$ that are superimposed on a ramp-like repulsion similar to that of the optimized pair potential for the TS lattice. As shown in figure 4.5b, this form gives rise to two sharp peaks in $\psi(r)$ at $r \sim 1.2$ and $r \sim 2.4$, which border a plateau region from $0.7 \lesssim r \lesssim 1.15$ and a broad hump from

$1.35 \lesssim r \lesssim 2.35$. Each of these features are important for stabilizing the TH lattice relative to its competitors and can be understood as follows.

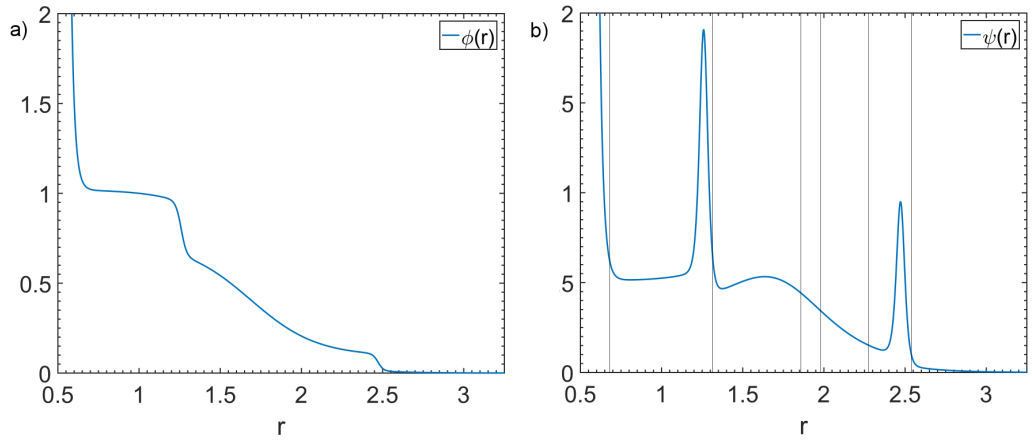

Figure 4.5: a) Repulsive pair potential $\phi(r)$ designed to stabilize the TH lattice as the ground-state structure, and (b) $\psi(r)$ obtained from $\phi(r)$ via eq. 4.2. Black vertical lines indicate positions of the first six coordination shells of the TH crystal at the midpoint of its stable density range ($\rho = 1.075$). The parameters of the optimized pair potential are presented in tables G.1 - G.4 of appendix G.

An analysis of coordination shell distances and occupation numbers shows that the plateau and broad hump features in $\psi(r)$ destabilize standard Bravais and non-Bravais competitors (hexagonal, snub square, honeycomb, etc) relative to the TH lattice because the former have more highly coordinated shells at those distances, and thus larger associated contributions to the chemical potential. It also shows that the sharp peak in $\psi(r)$ at $r \sim 1.2$ destabilizes stripe classes a-c) (refer to figure 4.1), which have first and second shell separations that closely track, but are slightly less than, those of the TH lattice. This is especially true for class c) stripes that have triangular motifs

similar to those in the target structure. The main role of the sharp peak in $\psi(r)$ at $r \sim 2.4$ is to penalize class d) and f) competitors whose first few shells share the same 'Y' shaped motif with the TH lattice (effectively shadowing TH shell distances) and thus can only be explicitly destabilized at these larger distances (more distant shells) where they display their stripe character. Lastly, note that the strongly repulsive 'core' acts as an extra destabilizing factor for stripe competitors with first shells that are slightly closer in than those of the TH lattice.

To further understand why the TH lattice presents such significant design challenges not encountered for the TS lattice, consider figure 4.6. Whereas the TS lattice (left) can be considered a class d) stripe structure (red rectangles) spanned by its internal motif (gray rectangle) with a specific inter-stripe distance, the TH lattice (right) cannot. Instead, the TH lattice displays a 'staggered' arrangement of the internal motif. Translated into our design process, this means that while the TS lattice must only be stabilized against deformations of its motif and interdistance stripe configuration, the TH lattice must instead compete with whole classes of highly variable stripe configurations that mimic its underlying motif structure and make ring closure–the staggered configuration–difficult to realize. This means narrow distinctions amongst many very closely related competitors that can only be meaningfully destabilized by sharply varying interactions (and the corresponding peaks seen in $\psi(r)$) that greatly complicate the optimization process. Consistent with this, the only other pair potential designed to stabilize the TH lattice [74] also

exhibits such step-like features.

Design challenges aside, we were able to verify self-assembly of the TH lattice from fluid configurations of particles interacting with the optimized pair potential via isochoric Monte Carlo temperature quenches. In this case, as described in section 4.2.3, assembly of the target structure (on computational time scales readily accessible via simulation) required the addition of a small seed crystal during the quenching process. As expected, success of crystallization depended largely on simulation time, with larger crystals or longer runs resulting in higher crystallization yield. For results shown here, we used a seed size (21 particles) such that approximately 50% of parallel runs quenched into the crystal structure during the course of the simulation (see figure G.3 in appendix G for an illustration). Shown in figure 4.7 are the initial and final configurations of one such seed run. The radial distribution of the assembled structure is provided in fig 4.8 and compared to that of a similar run started from the perfect crystal configuration at the final temperature and density. The excellent agreement shown demonstrates the success of the designed interaction for stabilizing the TH lattice.

4.4 Conclusion

Using the efficient method of chapter 2 for discovering interactions that favor a targeted ground-state crystal, we were able to determine repulsive, new isotropic interactions that stabilize open 2D TS and TH crystal lattices, respectively. For the TS crystal, the optimized interactions stabilized the

target structure in the ground state over a wide range of density, and particles interacting via the designed potential were shown to readily self-assemble into the TS crystal in isochoric Monte Carlo temperature quenches from a high-temperature fluid.

The open TH crystal proved to be a far more challenging design target, and its solution required consideration of significantly more competing structures as well as a more flexible repulsive pair potential. We demonstrated that while the TS crystal can be interpreted as a specific example of a stripe microphase, the TH crystal requires comparison against a highly varied field of stripe microphase competitors, and that the ring closure for the TH lattice required explicit staggering of underlying motifs that demanded very specific, sharply targeted interactions that greatly elevated the complexity of the problem. Despite this added difficulty, we found that particles with the designed interactions self-assemble into the TH crystal in isochoric Monte Carlo temperature quenches from a high-temperature fluid seeded with a small target crystal.

4.5 Author Contributions

Work presented in this chapter was published in 2017 [109]. W.D.P carried out GAMS optimization, molecular simulations and performed data analysis. T.M.T designed and funded the research.

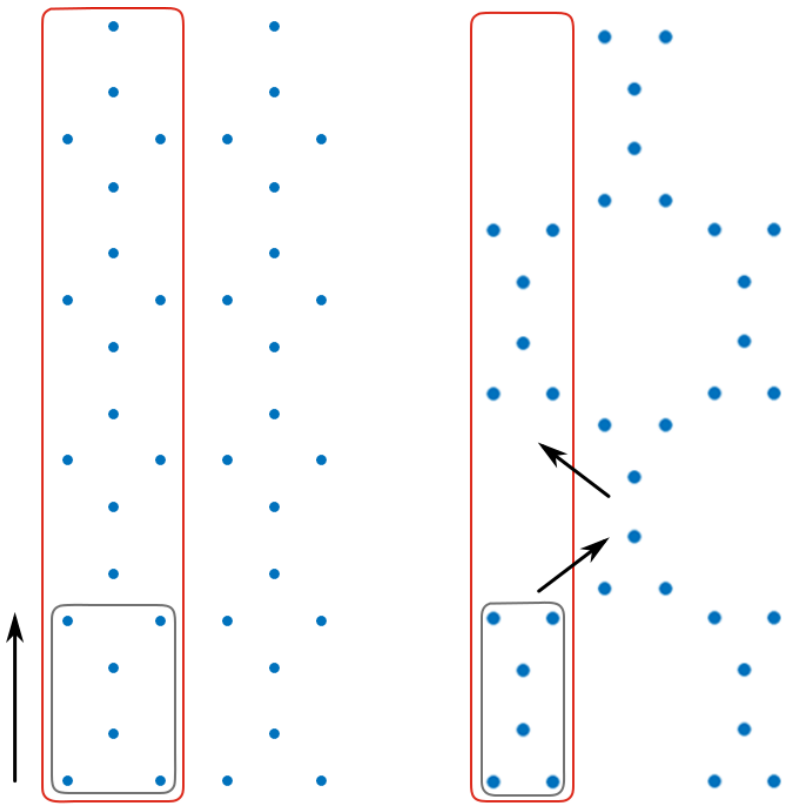

Figure 4.6: Design targets in the scope of stripe structures. While TS and TH lattices have similar motifs (bottom gray rectangles) only the TS lattice can be cast as parallel stripes (left red box) spanned by the underlying motif. A similar approach to forming the TH lattice (right red rectangle) leaves out spaces in the stripe as per the staggered arrangement of the TH motif.

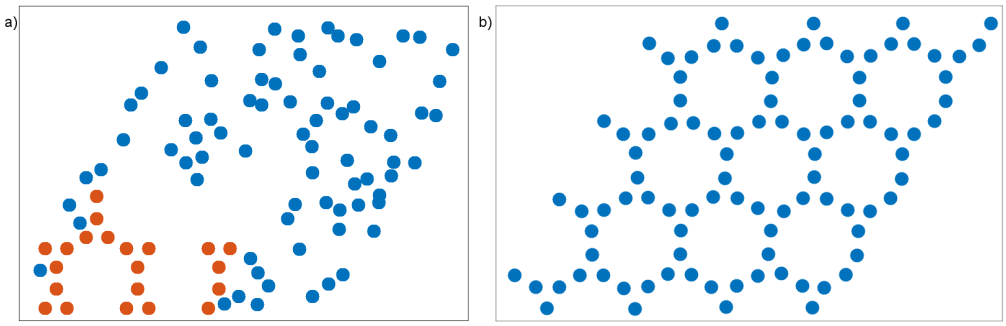

Figure 4.7: a) Initial configuration of a high temperature fluid at $\rho = 1.075$, seeded with a small frozen TH crystal. Periodic boundary image chosen such that a complete seed is visible at bottom left section of the simulation cell. b) Configuration of assembled crystal after quenching to $T = 0.06$ and equilibrating as described in the text.

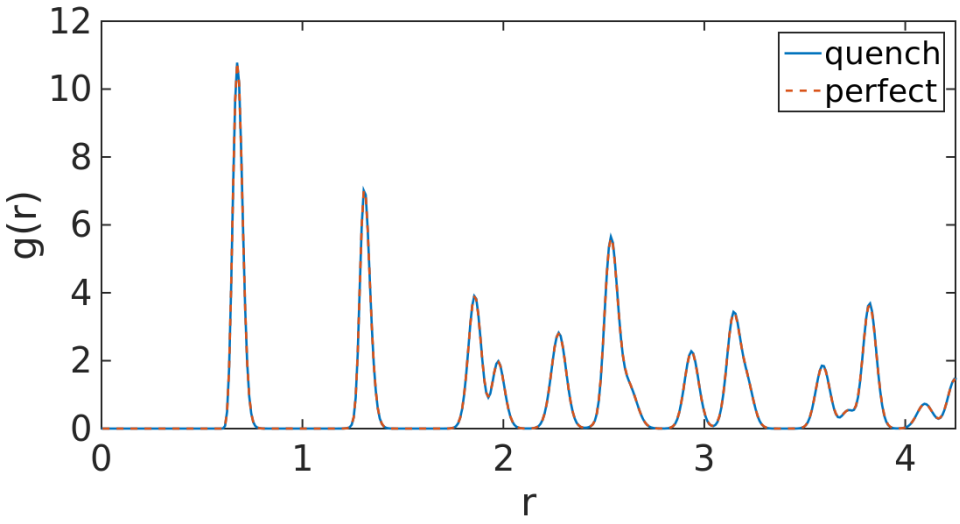

Figure 4.8: Radial distribution function $g(r)$ for the TH lattice at $T = 0.06$ and $\rho_0 = 1.075$: (solid blue line) assembled via quenching from a high temperature fluid and (red dash line) equilibrated starting from the perfect lattice configuration.

Chapter 5

Design of two-dimensional particle assemblies using isotropic pair interactions with an attractive well

5.1 Introduction

In addition to the ground state method of chapters 2 - 4, an alternative inverse design method based on relative-entropy (RE) maximization was recently shown [74, 75] by the Truskett group to be capable of discovering interactions that promote *spontaneous assembly* of a target lattice from the disordered fluid upon cooling. Notably, the RE optimization computes interactions "on-the-fly" based on structures accessed in a simulation and thus avoids the need to explicitly identify possible competing structures in advance. As a result, the RE approach has been able to help design isotropic interactions that favor unusually open ordered phases (e.g., truncated hexagonal [74] and truncated tri-hexagonal [75] lattices, which naturally compete with a variety of stripe-phase structures that are difficult to identify *a priori*) as well as disordered hierarchical structures (e.g., porous mesophases [75, 78] and cluster fluids [75, 77], which are not easily designable with GS-based optimization strategies). However, because RE maximization does not require identification of competing structures, it cannot provide direct insights into how the

optimized interactions stabilize the target relative to its competitors.

In this chapter, we use both GS and RE optimization strategies to investigate a thus far unanswered question: which open two-dimensional crystal structures can be stabilized by an isotropic pair interaction comprising a repulsive core and a single attractive well? Interactions of this form are ubiquitous in nature, e.g., those present in noble gases and liquid metals [110], the former of which have thermodynamic properties that are well captured by the familiar Lennard-Jones model [79, 93]. Single-well (effective) interactions can also arise in colloidal systems where, e.g., depletion interactions, van der Waals forces, and screened Coulomb interactions are present and can be tuned via the material selections made for the particle core, surface-passivating polymers or ligands, co-solutes, and the solvent. [31, 80, 81, 111] Given the diverse contexts in which single-well interactions naturally emerge and can even be systematically modified, it is of interest to theoretically explore how the combination of a repulsive core and an attractive well might be chosen to favor various targeted crystal structures.

Specifically, in this chapter we study the inverse design of isotropic, single-well pair potentials to stabilize 2D crystal structures (square, honeycomb, and kagome) using GS and RE methodologies and show that from generalities of the obtained interactions it is possible to infer a set of 'design rules' involving single well interactions. We then use these 'design rules' to stabilize the challeging truncated square and truncated hexagonal lattices.

5.2 Methods

5.2.1 Ground State Optimization

5.2.1.1 Analytical Formulation

In this method, we seek an isotropic, single-well interparticle pair potential $\phi(r;\{\alpha\})$ that stabilizes a target lattice l_t as the ground state over (at least) a narrow density range. Broadly speaking, we formulate the design as an analytical nonlinear program and determine the pair potential parameters $\{\alpha\}$ via its numerical solution using GAMS (General Algebraic Modeling System) [92, 112, 113].

For the model pair interaction, we choose the functional form $\phi(r;\{\alpha\})$,

$$\phi(r)/\epsilon = \begin{cases} A/r^n \exp\left(-r^2/\sigma_0\right) + \sum_i^2 B_i \exp\left(-(r-r_i)^2/\sigma_i\right) + f_{\text{shift}}(r) & r < r_{\text{c}} \\ 0 & r \geq r_{\text{c}} \end{cases} \tag{5.1}$$

where $r = r/\sigma$, A, n, σ_0, B_i, r_i and σ_i are design parameters (i.e. $\{\alpha\}$), r_c is the cut-off radius and $f_{\text{shift}}(r) = Pr^2 + Qr + R$ is a quadratic shift function added to enforce $\phi(r_{\text{c}}) = \phi'(r_{\text{c}}) = \phi''(r_{\text{c}}) = 0$. Location of the potential minimum $r_{\min}$ is fixed as

$$\phi'(r_{\min}) = 0 \tag{5.2}$$

and an appropriate well profile is achieved by means of the following constraint equation

$$\begin{aligned} \phi'(\mathbf{r}_l) < 0 \quad r < r_{\min} \\ \phi'(\mathbf{r}_r) > 0 \quad r > r_{\min} \end{aligned} \tag{5.3}$$

where $\mathbf{r}_i$ denotes an appropriately distributed set of radial points left$(i = l)$ or right$(i = r)$ of $r_{\min}$. The magnitude of the minimum was fixed such that

$\phi(r_{\min}) = -\epsilon$. Finally, we constrain B_1 and σ_0, σ_2 as

$$\begin{aligned} B_1 &< 0 \\ \sigma_1 &> 2\sigma_0 \\ \sigma_1 &> \sigma_2 \end{aligned} \tag{5.4}$$

To simplify notation, quantities are implicitly nondimensionalized from this point forward in terms of the usual (dimensionally appropriate) combination of parameters, including the energy scale ϵ, the length scale σ, or the Boltzmann constant k_B.

We compute quantities of interest over a narrow density range using the canonical ensemble. In particular, we consider a grid of densities $\{\rho_j\}$ that spans a range $\Delta\rho = 1.21 - 1.23$ to compute the potential energy U of the target lattice and equidensity competing structures,

$$U(\rho_j) = \frac{1}{2}\sum_{r}^{r_c} n_i \phi(r_i; \rho_j) \tag{5.5}$$

where the sum is over all lattice-dependent coordination shells n_i at distances r_i up to the pair-potential cut-off. Similarly, the potential energy for phase-separated competitors $U_{\rm PS}$ was computed as [90]

$$U_{\rm PS}(\rho_j) = (1-x)(U_2 - U_1) - U_1 \tag{5.6}$$

where x is the molar fraction for the crystal phase l_1, $U_{\rm PS;}(\rho_j)$ is the total system energy at net density ρ_j and U_i is the potential energy for crystal l_i at density ρ_i (see appendix C for derivation of this equation). Due to the narrow density range, energies of phase separated structures at only the midpoint

density of the range ρ_m were sufficient to consider for optimization purposes. Stability of the target lattice relative to these competitors for the remainder of density points within the range was verified by means of forward ground-state phase diagram calculations, as discussed below.

Finally, we define an objective function F that maximizes the sum of the energy differences of the target and competitors at the midpoint density $\rho_m = 1.22$ as

$$F = \sum_{l_i} U_{l_i}(\rho_m) - U_t(\rho_m) \tag{5.7}$$

where $U_t(\rho_m)$ denotes the target's energy and $U_{l_i}(\rho_m)$ the energy of a competitor lattice l_i. Stability of the target lattice for the remaining grid points $\{\rho_j\}$ was ensured by constraining the energy differences for every competitor l_i as

$$U_{l_i}(\rho_j) - U_t(\rho_j) > 0 \tag{5.8}$$

Below, we discuss how structures that closely compete with the target are identified.

5.2.1.2 Competing Structures

The pool of closely competing structures for the GS optimization was determined in the following way. First, an initial competing pool comprising lattices commonly stabilized by isotropic potentials was chosen, and the optimization was performed based on comparisons of the target lattice with that pool. The resulting optimized pair potential was then used to a carry out a 'forward calculation' in which the stability of the target lattice was deter-

mined relative to a comprehensive list of possible competing lattices (including those with variable parameters chosen via optimization using GAMS as well as lattices co-existing at different densities). Any structures found to be more energetically stable than the target were then added to the competing pool for a subsequent optimization. This process was repeated until the forward calculation of the optimized pair potential yielded no new competitors and established the target as the energy minimum, a point at which the optimization procedure was considered converged and completed. The detailed calculation procedure for single phases has been explained in detail in previous chapters. A discussion of how to consider phase-separated crystals is provided in appendix C.

Following this approach, the final competing pools for square, honeycomb and kagome lattices were determined to be as follows:

Square target: hexagonal, kagome, snub hexagonal, snub square, elongated triangular, and rectangular ($b/a = 1.17$) lattices, as well as phase-separated lattice structures comprising square and hexagonal lattices which we denote by (square lattice density)/(hexagonal lattice density) and the corresponding square lattice molar fraction: (1) 1.1479/1.4344, 0.7040; (2) 1.2675/0.7008, 0.9518; (3) 1.2512/0.7095, 0.9665; (4) 1.1833/1.44961, 0.83636; (5) 1.2279/0.7050, 0.9912.

Honeycomb target: hexagonal, square, kagome, snub hexagonal, elongated triangular, rectangular ($b/a = 1.59$) lattices, and three specialized

competitors, two of which resembled a distorted honeycomb and a staggered elongated triangular (see figure H.1 in appendix H). There was a single phase-separated structure composed of honeycomb and hexagonal crystals which we denote by (honeycomb density)/(hexagonal density) and honeycomb molar fraction: 0.49180/1.86031 0.18861.

Kagome target: hexagonal, square, snub hexagonal, elongated triangular, honeycomb, kagome ($b/a = 1.02$), and twisted kagome lattices, as well as a specialized competitor resembling rows of staggered rectangular boxes (see figure H.2 in appendix H). No phase-separated competitors were found for this target.

5.2.2 Relative Entropy Optimization

Relative entropy course graining relies on maximizing the probability of achieving a desired equilibrium configurational ensemble by optimizing a set of parameters $\boldsymbol{\theta} = \{\theta_1, \theta_2, ..., \theta_m\}$ of the interaction pair potential $u(r|\boldsymbol{\theta})$. This can be achieved by direct ("on-the-fly") optimization in a simulation, [74] where potential parameters are periodically updated as

$$\boldsymbol{\theta}^{i+1} = \boldsymbol{\theta}^i + \gamma \int_0^\infty dr r[g(r|\boldsymbol{\theta}^i) - g_{\text{tgt}}(r)][\boldsymbol{\nabla}_\theta u(r|\boldsymbol{\theta})]_{\boldsymbol{\theta}=\boldsymbol{\theta}^i} \tag{5.9}$$

where i indicates iteration step, $g(r|\boldsymbol{\theta}^i)$ is the current radial distribution function, $g_{\text{tgt}}(r)$ is the target lattice radial distribution function and γ is an adjustable scalar parameter to ensure stability and convergence of the optimization. Detailed derivation of this update procedure is available in previous

work [74, 75]. In this paper, we use $u(r|\boldsymbol{\theta})$ consisting of Akima splines whose knots are the parameters. We constrain the splines to display the features of a single attractive well with a minimum located at $r_{\min}$. If we consider a set of scalars $\mathbf{r} = \{r_1, r_2, ..., r_{\mathrm{m}}\}$ as denoting the position of the Akima knots, the well constraint is easier to implement by considering the parameters $\boldsymbol{\theta} \equiv \theta(\mathbf{r})$ as differences of the pair potential

$$\theta(r_k) = -[u(r_{k+1}) - u(r_k)] \tag{5.10}$$

where the sign has been inverted to resemble a force term and for simulation convenience. The desired interaction form can then be achieved by constraining positions to the left ($\mathbf{r}_l$) and right ($\mathbf{r}_r$) of the minimum as

$$\begin{aligned} \theta(\mathbf{r}_l) > 0 \quad \mathbf{r}_l < r_{\min} \\ \theta(\mathbf{r}_r) < 0 \quad \mathbf{r}_r > r_{\min} \end{aligned} \tag{5.11}$$

Lastly, the minimum position itself is free to vary and is updated as follows

$$\begin{aligned} &\text{if } u(r_{\min})^{i+1} > 0 \quad \text{and } |u(r_{k+1})^{i+1}| < |u(r_{\min})^{i+1}| \quad \text{then } r_{\min} = r_{k+1} \\ &\text{if } u(r_{\min})^{i+1} < 0 \quad \text{and } |u(r_{k-1})^{i+1}| < |u(r_{\min})^{i+1}| \quad \text{then } r_{\min} = r_{k-1} \end{aligned} \tag{5.12}$$

where $|...|$ indicates absolute value, the $i+1$ superscript indicates the next iteration round, and k subscripts indicates the knot position immediately to the left $(k-1)$ or right $(k+1)$ of the $r_{\min}$ position at the ith iteration. Derivation of this result is provided in appendix D.

5.2.3 Molecular Simulations

5.2.3.1 Molecular Dynamics For Relative Entropy Optimization

The Relative Entropy (RE) optimization is implemented with the GROMACS 4.6.5 molecular dynamics package [114, 115]. Briefly, a system of particles ($N = 200 - 1000$) interacting via a single-well spline pair potential is simulated in the canonical ensemble using a periodically replicated rectangular simulation cell with aspect ratio chosen to accommodate the target lattice. The system is initiated in the target lattice at $T = 1$, melted via a run of 2×10^6 time steps at $T = 1.5$, and then slowly cooled back to $T = 1$ (over 5×10^6 time steps). Radial distribution function statistics $g(r)$ are collected over the last 10^6 time steps and compared to the target's structure $g_{\text{tgt}}(r)$. The spline potential is then updated per Eq. 5.9 and the process is iterated in this manner. In practice, $\gamma = 0.005 - 0.01$ is sufficient for all crystal target structures considered here. Convergence is typically achieved in about 100-200 iterations, and optimization is considered complete once the self-assembled crystal remains stable up to $T = 1.5$.

5.2.3.2 Monte Carlo Simulations

Monte Carlo simulations were used to test for stability of target lattices of particles interacting via the potentials obtained from the ground-state optimizations. In particular, systems of N particles ($N = 64$, 40, 108 for square, honeycomb, and kagome targets, respectively) interacting via Eq. 5.1 with their respective ground-state optimized parameters were simulated in the

canonical ensemble using a periodically replicated simulation cell with densities and aspect ratios chosen to best accommodate the target lattices. In each case, the target was melted to form a liquid at a high temperature and then either quenched (square lattice) or slowly cooled (over $\sim 5 \times 10^6$ Monte Carlo steps for the honeycomb and kagome lattices) to low temperature to check for assembly of the target crystal. For the square, honeycomb, and kagome lattices, the aforementioned high temperatures were $T = 0.5091$, 1.2091, and 2 and the low temperatures were $T = 0.1627$, 0.5, and 0.5. For the 24 Monte Carlo simulations we performed for the three targets, we observed ideal assembly in 50% (square), 17% (honeycomb), and 100% (kagome) of the runs.

5.3 Results and Discussion

As demonstrated below (see Fig. 5.1-5.5), we were able to discover, using the inverse design methodologies of RE and GS optimization and the Monte Carlo simulations described in Sec. 5.2, isotropic pair potentials with a single well that promote self-assembly of all targeted lattices. Below, we examine the resulting optimized pair potentials and briefly discuss them within the context of the 'design rules' that they suggest for this class of systems.

1. The interaction range must span a minimum number of coordination shells

This rule of thumb states the intuitive idea that the range of an isotropic interaction potential must be large enough to distinguish (and hence pro-

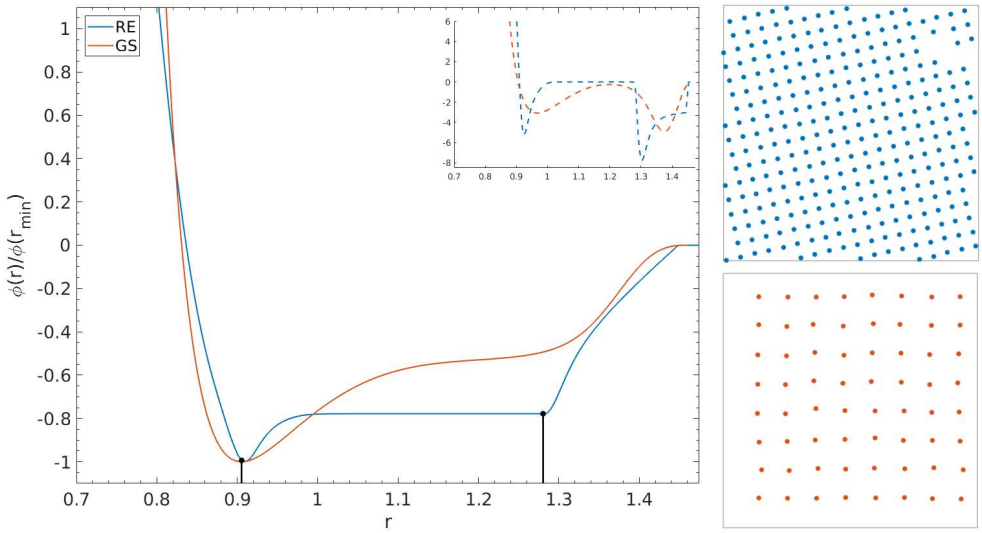

Figure 5.1: Left: Inversely designed pair potentials $\phi(r)/\phi(r_{min})$ (solid lines) for the square lattice from RE (blue) and GS (red) optimization strategies described in Sec. 5.2, where r_{min} denotes radial position of the well minimum. Normalized forces $-\phi'(r)/\phi(r_{min})$ are shown in the inset. Black vertical lines denote the ideal coordinate shell positions of the target structure at the optimization density. Potential parameters for the GS optimization are provided in appendix H. Top right: Configuration from a molecular dynamics simulated annealing run using the RE optimized pair potential. Bottom right: Configuration from a Monte Carlo quench of the GS optimized pair potential.

vide energetic advantage to) the target structure compared to its competitors. While only strictly true at zero temperature, we find that it provides a helpful guide for designing isotropic pair potentials to stabilize and promote assembly of our target lattices. Evidence of this rule's utility was recently demonstrated in an RE optimization study where the shortest range isotropic, repulsive pair potential for stabilizing each of a wide variety of two-dimensional lattices was determined. [74] In that work, it was shown that the square and honeycomb lattices could be stabilized by an interaction spanning only two co-

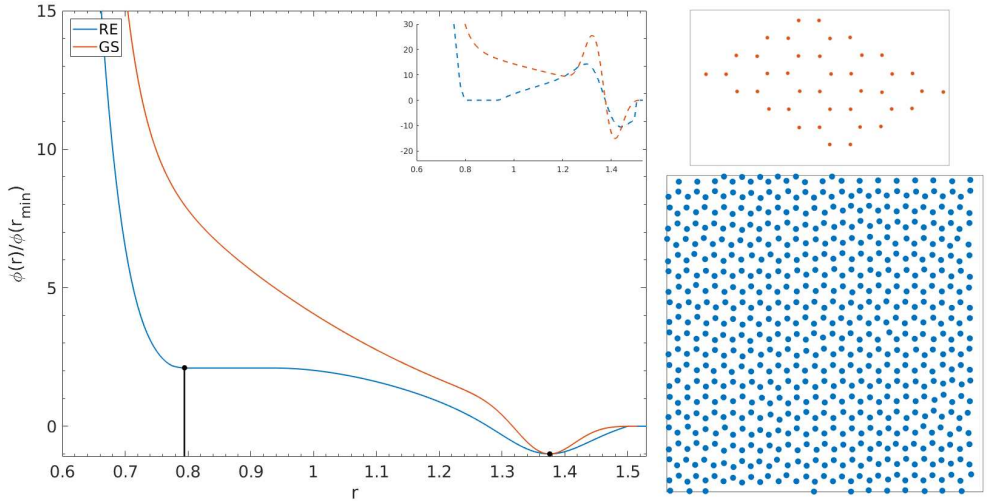

Figure 5.2: Left: Inversely designed pair potentials $\phi(r)/\phi(r_{min})$ (solid lines) for the honeycomb lattice from RE (blue) and GS (red) optimization strategies described in Sec. 5.2, where r_{min} denotes radial position of the well minimum. Normalized forces $-\phi'(r)/\phi(r_{min})$ are shown in the inset. Black vertical lines denote the ideal coordinate shell positions of the target structure at the optimization density. Potential parameters for the GS optimization are provided in the appendix H. Top right: Configuration from a molecular dynamics simulated annealing run using the RE optimized pair potential. Bottom right: Configuration from a Monte Carlo quench of the GS optimized pair potential.

ordination shells, while the kagome lattice required a potential spanning three shells. These results are consistent with the single-well pair potentials we obtain here from optimizations for the corresponding target lattices (see black bars denoting coordination-shell locations in figures 5.1, 5.2, and 5.3 for square, honeycomb and kagome lattices respectively). As discussed below, the single-well potentials designed to stabilize truncated square and truncated hexagonal lattices also span the minimum number of shells previously reported for these structures. [74] Consistent with this rule, our attempts to design single-well

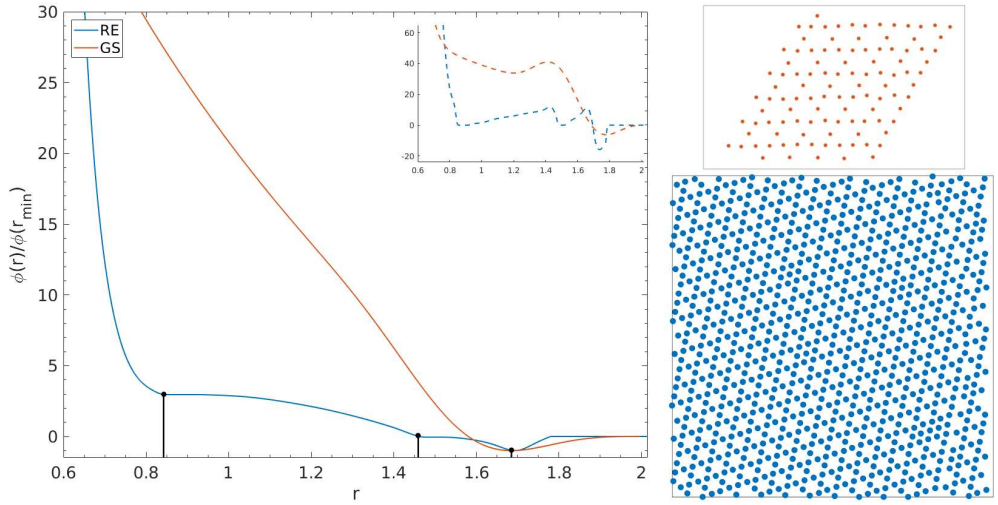

Figure 5.3: Left: Inversely designed pair potentials $\phi(r)/\phi(r_{min})$ (solid lines) for the kagome lattice from RE (blue) and GS (red) optimization strategies described in Sec. 5.2, where r_{min} denotes radial position of the well minimum. Normalized forces $-\phi'(r)/\phi(r_{min})$ are shown in the inset. Black vertical lines denote the ideal coordinate shell positions of the target structure at the optimization density. Potential parameters for the GS optimization are provided in the appendix H. Top right: Configuration from a molecular dynamics simulated annealing run using the RE optimized pair potential. Bottom right: Configuration from a Monte Carlo quench of the GS optimized pair potential.

pair potentials that stabilize any of these structures using shorter range interactions were unsuccessful, and simulations employing the resulting optimized potentials led to either amorphous (glassy) or competing crystalline structures. Consistency with this rule may also be found retrospectively in the other published works featuring the same design targets (e.g., square [58, 59, 103] and honeycomb [58–60]) and was briefly hinted at in another recent inverse design study [62]. Thus, while the results of the present study are not the first to suggest this design rule, they solidify the notion that a minimum interaction range

must typically be spanned by an isotropic potential to favor a target structure compared to its competitors, an observation which acts as the foundation for the next two rules.

2. The attractive well must be narrow, spanning only the most distant coordination shell(s) in the required range

Given the observation that an isotropic pair potential requires a minimal range to stabilize a given target structure relative to its competitors, one might ask whether one can expect that a simple (e.g., Lennard-Jones-like) pair potential with a wider range of negative energy (i.e., a wider well) that spans the first and more distant coordination shells in the target lattice can stabilize any of the open structures considered here. Based on the results of our inverse design study, the answer is no, save for the square lattice. The optimized potentials for the square lattice target (see figure 5.1) have their minimum in the first-neighbor shell, which may at first glance appear counterintuitive since the first shell of the closely competing triangular lattice has more neighbors (six versus four) and hence a more favorable first-shell contribution to the energy. However an energetic advantage of the square lattice is still accomplished with this interaction by having a well that is wide enough to reach the second neighbors of the square lattice but not the more distant second neighbors of the triangular lattice.

For the more complex honeycomb and kagome structures, we found that the attractive well feature had to be constrained to the last one or two (closely

spaced) shells of the interaction range (see plots in figure 5.2 and 5.3). If the pair potential wells were allowed to incorporate nearer coordination shells as well, the optimizations and subsequent forward calculations would inevitably find that phase-separated structures involving a more highly coordinated and hence more energetically stable (typically triangular) lattice were more favorable than the single-phase target structure. This was true for either GS or RE optimization strategies, and the qualitative similarity of the designed pair potentials (and corresponding forces shown in the figure insets) points toward the generality of this observation.

3. Nontrivial repulsive features (e.g., shoulders) are needed in addition to the attractive well in the pair potential to stabilize more complex targets

Given the constraints on the location and width of the attractive well discussed in the rules above, there is still a question of how simple the repulsive profile ($r < r_{min}$) can be in a single-well pair potential and simultaneously stabilize the target structure. As can be seen from the pair potentials and forces shown in figures 5.2 and 5.3 for the honeycomb and kagome lattices, nontrivial features in the repulsive interactions naturally emerge from the GS and RE optimizations for low-coordinated target structures. As emphasized in the previous inverse design studies using repulsive isotropic potentials of chapters 2 - 4, these features are tied to the location of coordination shells in competing lattices and necessary to stabilize target structures relative to more highly coordinated lattices, including the triangular crystal, which are

otherwise naturally favored by smooth, short-range repulsive interactions. Instead of shoulders, the presence of multiple positive wells in the potential (if allowed in the optimization) could also have the same effect. Importantly, the inclusion of a single well in the pair interaction does not obviate the need for shoulders or other nontrivial repulsive features in the potential for $r < r_{min}$.

Having identified the three qualitative rules above, we conclude by presenting their application to the design of the more challenging, highly open structures of the truncated square lattice and the truncated hexagonal lattice. Pair potentials stabilizing these structures with purely repulsive interactions were discussed in chapter 4 and have recently been reported using the RE [74, 75] method as well. However, due to the known complexity and tediousness involved in targeting these open structures with GS calculations (specifically, in identifying the large set of relevant competing structures which include a multiplicity of stripe phases), here we limit the pair potential discovery to the RE method. As such, following rule 1, we know in advance from the published studies the expected minimum interaction range to stabilize these targets. Next, we anticipate that the single well feature must lie towards the end of the interaction well and not be too broad as per rule 2. Finally, we expect the stabilization to require the introduction of multiple repulsive shoulders in the pair potential before the well, as per rule 3.

Our designed single-well interactions for these target structures are displayed in figure 5.4. Indeed, as can be seen, both potentials display the expected features as per the applied 'design rules' and, save for the single well,

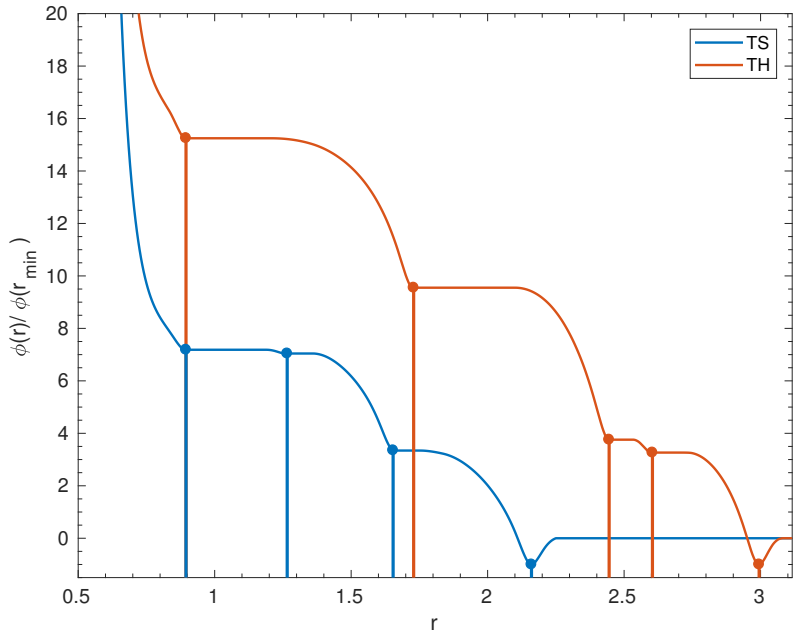

Figure 5.4: Inversely designed pair potentials $\phi(r)/\phi(r_{min})$ (solid lines) for truncated square (blue) and truncated hexagonal (red) lattices using the RE optimization strategy described in Sec. 5.2, where r_{min} denotes radial position of the well minimum. Vertical lines denote the respective coordinate shell positions for the targeted lattices at the optimized density.

closely resemble those published for the same targets in previous RE work (figure [3] [74]). The resulting self-assembled structures using the optimized interactions are shown in figure 5.5. Note that when we constrained the attractive well to be centered in a shell closer to the origin but still spanning the minimum interaction range (i.e. a broad well encompassing more than the outermost coordination shell(s)), the design strategy failed to stabilize any of these target structures, which further confirms the validity of design rule 2.

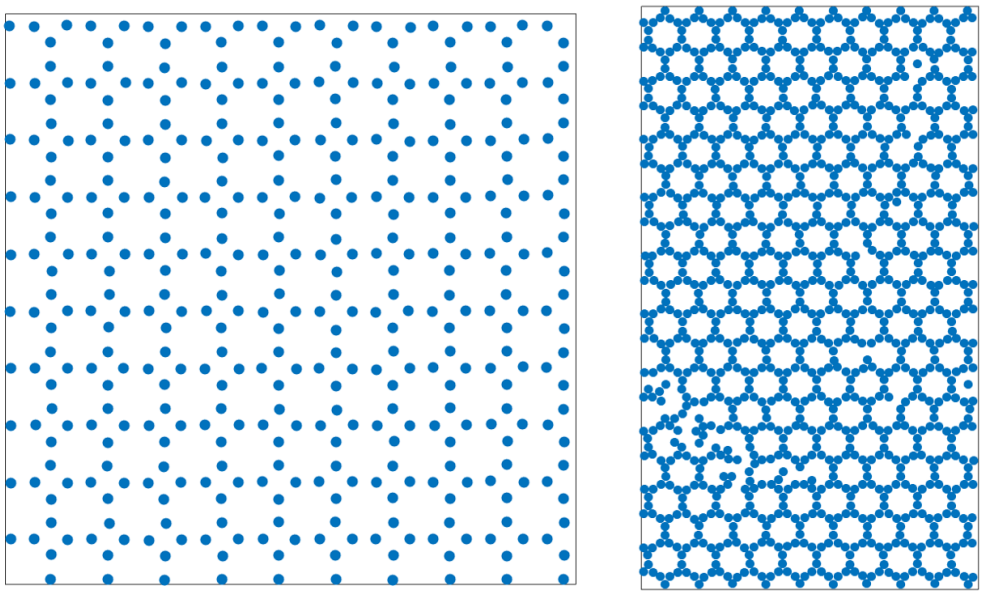

Figure 5.5: Configuration snapshots from molecular dynamics simulated annealing runs for systems of particles interacting through the RE optimized pair potentials of Fig. 5.4 for truncated square (left) and truncated hexagonal (right) target lattices.

5.4 Conclusions

Isotropic pair interactions comprising a repulsive core and a single attractive well are models for effective interactions that are ubiquitous in colloidal fluids and interesting for material design applications due to their possible tunability. Using GS and RE inverse design methods, we have inferred a set of 'design rules' that help to understand the properties of single-well pair potentials that can stabilize three distinct two-dimensional target lattices (square, honeycomb and kagome). These rules can be summarized as (1) the interaction range must span a minimum number of coordination shells

to differentiate the target structure from its competitors, (2) the well must be relatively narrow and located toward the end of the minimally required interaction range, and (3) nontrivial repulsive features (e.g., shoulders) in the potential spanning specific coordination shells in the target and competing lattices are required to impose energetic advantages to the target structure.

We further examined two challenging, low-coordinated target structures using the RE inverse design approach: truncated square and truncated hexagonal lattices. The optimized pair potentials, which displayed features consistent with the aforementioned design rules, readily assembled into the target structures upon cooling in computer simulations. Given their applicability across a wide variety of target structures, potential functional forms, and design methods, we believe these rules will be equally applicable to other crystal design targets in 3D, where transferability of 2D results to 3D targets are known to apply in repulsive systems [59] and greatly simplify the design process.

5.5 Author Contributions

Work presented in this chapter was published in 2017 [116]. W.D.P carried out GAMS and RE optimization, molecular simulations and performed analysis. R.B.J. provided the original RE code framework. T.M.T designed and funded the research.

Chapter 6

Inverse Design of Multicomponent Assemblies

6.1 Introduction

All presented work in this thesis so far demonstrates the large wealth of structures that can theoretically be assembled from single-component systems with isotropic interactions. However, multicomponent systems are also an attractive design choice given the additional degrees of freedom that expand the available design space. While this expansion increases the complexity of the optimization problem, it might also lead to interparticle interactions that, for a given target, have simpler (and perhaps more easily realizable) functional forms than those discovered under the constraint of a single-component design. Moreover, multicomponent systems can stabilize entirely new and exotic structures which are inaccessible to single-component systems. For instance, it is known that moving from single-component to binary colloidal systems significantly diversifies the list of crystal structures and motifs observed in experiment. [85, 86, 117] Similarly, recent theoretical and computational efforts demonstrate that binary mixtures can produce a wide variety of novel structures, some of which exhibit highly specific local orderings. [104, 118–121]

While the aforementioned cited work characterize structures resulting

from systematic study of particular interaction models chosen *a priori* (i.e., a forward approach), the use of inverse design to discover interactions that promote assembly of a specific target lattice in the extended component space remains to be demonstrated. Here, we adopt the latter strategy, extending the RE optimization strategy for inverse design of single-component materials interacting via isotropic interparticle potentials to multicomponent systems. By independently optimizing the self and cross interactions for species in a binary two-dimensional mixture, we demonstrate that this methodology can successfully discover pair potentials that readily self-assemble a variety of simple (intercalated square and triangular) lattices as well as more challenging target phases (stripes and highly open structures), many of which had not yet, to our knowledge, been observed to self-assemble for such systems. For select cases, we further compare the optimized binary interactions to those obtained from optimizations for the target structures assuming single-component systems. These comparisons help to understand the trade-offs associated with using binary systems for self assembly as well as the roles of self versus cross interactions in stabilizing various target lattices.

6.2 Methods

6.2.1 Relative Entropy Optimization

The RE course graining approach is a probabilistic optimization method that addresses an inverse design problem for self-assembly by systematically tuning the interparticle interaction potential $U(r|\boldsymbol{\theta})$ in a system of particles

via parameters $\boldsymbol{\theta} \equiv \{\theta_1, ...\theta_m\}$ to maximize the likelihood of forming a desired structure. One advantage of the approach is that it can perform "on-the-fly" optimization of particle interactions during the course of a simulation in order to promote thermodynamic stability (and, with a judicious choice for the simulation protocol, [74] kinetic accessibility) of the assembled target phase. Although RE optimization was originally applied to single-component systems, [74, 75] it can be readily extended to multicomponent materials. For a two-dimensional binary system with components A and B, we partition the energy and parameters in terms of self and cross interactions as $u(r|\boldsymbol{\theta}^{(k,k')})$ where $k, k' = A$ or B. Parameters $\boldsymbol{\theta}^{(k,k')}$ are then updated with a gradient ascent procedure as:

$$\boldsymbol{\theta}_{i+1}^{(k,k')} = \boldsymbol{\theta}_{i}^{(k,k')} + \alpha^{(k,k')} \int dr r[g^{(k,k')}(r|\boldsymbol{\theta}_{i}^{(k,k')}) - g_{\mathrm{tgt}}^{(k,k')}(r)][\boldsymbol{\nabla}_{\boldsymbol{\theta}} u(r|\boldsymbol{\theta})]_{\boldsymbol{\theta}\equiv\boldsymbol{\theta}_i^{(k,k')}} \tag{6.1}$$

where i indicates iteration step, $g(r|\boldsymbol{\theta}_i^{(k,k')})$ represents the simulated radial distribution function (RDF), $g_{\mathrm{tgt}}^{(k,k')}(r)$ is the target RDF, $[\boldsymbol{\nabla}_{\boldsymbol{\theta}} u(r|\boldsymbol{\theta})]_{\boldsymbol{\theta}\equiv\boldsymbol{\theta}_i^{(k,k')}}$ denotes the gradient of the pair potential, and $\alpha^{(k,k')}$ is a learning rate chosen to ensure simulation stability and convergence. While it may be possible to choose a single value of the learning rate parameter that is effective for all interaction types, we adopt independently tuned values for the three interaction types here to attain faster convergence. We define $u(r|\boldsymbol{\theta}^{(k,k')})$ as a set of Akima splines whose knots are computed from $\boldsymbol{\theta}^{(k,k')}$ as reported in Ref. 74. Lastly, the knot amplitudes are restricted to increase with decreasing values of r to ensure a monotonically decreasing (i.e., repulsive) pair potential. For

a derivation of the update expression presented in eq. 6.1 see appendix E.

6.2.2 Crystal Target Selections

A tiling can be described by the vertices formed by the underlying polygon tiles and denoted as $[n_1.n_2....]$ where n_i denotes the numbers of sides for the polygons that meet at each vertex. [122] For instance, in the case of a square lattice, each vertex is the meeting point of 4 squares tiles; in vertex notation this lattice is denoted by [4.4.4.4] or $[4^4]$ for short. Tilings consisting of k vertex types are said to be k-uniform and denoted similarly as $[n_1^1.n_2^1...;\ ...;\ n_1^k.n_2^k...]$. For a crystal composed of particles at the vertices of regular polygon tilings, the number of non-equivalent origins in the crystal then corresponds to the number of k vertices necessary to create the crystal. In this work, we only consider target lattices that are 1- and 2-uniform tilings in order to guarantee a single equivalent origin for each component in the binary mixture. In addition to regular polygon tilings, we consider a tiling consisting of an octadecagonal polygon and a star polygon with 3 corners with internal angle of $2\pi/9$–denoted as $[18^2.3_{2\pi/9}]$. Our chosen targets are shown in Fig. 6.1 a) through f) in formal vertex notation. Note that some realized crystals are based on a single underlying vertex (e.g., square $[4^4]$) but with the components arranged so as to create new structural motifs (e.g., intercalated rows of stripes) while still conserving origin equivalency. In such a case the actual vertex seen by the *individual* component may not be regular, but together with the other component, still span the original vertex of the

tiling.

6.2.3 Molecular Simulations

6.3 Results and Discussion

Following the RE optimization protocol elaborated in Sect. 6.2, isotropic interparticle potentials for binary mixtures that successfully self-assembled each of our nine binary crystal targets were designed. The optimized potentials and assemblies are shown for systems featuring triangular and honeycomb motifs (Fig. 6.2), squares and stripes (Fig. 6.3), and other more complex, open structures (Fig. 6.4). Most of the optimized potentials yield excellent particle assembly including the very open and intricate 'square truncated hexagonal' (STH) or 'octadecagonal star binary' lattices presented in Fig. 6.4.

Considering the designed interactions and the associated assembled structures shown in Fig. 6.2–6.4, two general observations can be made. First, targets featuring equivalent component sites yield comparable interactions for A and B components as should be expected based on symmetry. This can be seen, for instance, in the square binary or square stripe structures shown in Fig. 6.3 (top or middle, respectively), where exchanging component identities would yield near-identical configurations. Second, optimized AA, BB and AB pair potentials become longer ranged and exhibit more features (i.e., shoulders and plateaus) as the target structures become more open and complex. Compare, for instance, potentials for square binary in Fig. 6.3 (top) with those of STH in Fig. 6.4 (middle). The former are clearly short ranged and feature a

single shoulder, while STH interactions are longer ranged and exhibit multiple plateaus.

We also find evidence for two advantages of binary mixtures over single-component systems for self assembly: 1) the optimized pair interactions of a binary system can each be simpler than an analogous single-component interaction designed to stabilize the same *global* (or overall) structure, and 2) the expanded parameter space of a binary system can help to stabilize a richer variety of self-assembled structures than single-component systems. To illustrate the former, we consider the triangular honeycomb structure in Fig. 6.2 (bottom). The underlying tiling is 2-uniform as illustrated in Fig. 6.1c. Therefore, the global structure of the lattice can be naturally partitioned into two simpler sub-lattices: a honeycomb lattice (red particles) and a triangular lattice with a side length of three (blue particles). By allowing two components to occupy the two distinct types of lattice sites, relatively simple interactions can be combined to favor self-assembly of a rather complex target. By contrast, when the same *global* structure was targeted via a single-component optimization, the best resulting interaction was not only considerably more complex, but also self-assembly of the target structure was significantly less satisfactory than for the binary mixture (see Fig. I.1). As a second example, a previous study reported [62] that single-component assembly of a rectangular kagome lattice from a single-component system required an interaction possessing an abrupt attractive well within a larger repulsive profile, while the optimized binary interactions reported here for the same structure are purely repulsive

and limited to a few shoulder features; see Fig. 6.2 (middle).

With respect to binary mixtures increasing the diversity of possible self-assembled structures relative to single-component systems, the partitioning of a desired global structure into individual sub-lattices corresponding to each species not only allows for self-assembly of intricate structures such as STH and octadecagonal star binary lattices (Fig. 6.4), but it also opens up the possibility of segregating components in specific *local* structures using an otherwise simple global lattice structure. This is seen clearly in Fig. 6.3 where the same underlying square lattice is partitioned to form intercalated squares (top) or stripes with either a 1:1 (middle) or a 2:1 (bottom) ratio. As expected, we find that increasing the asymmetry of the particle arrangement (as is displayed from top to bottom in Fig. 6.3) generally requires more complex potentials in terms of both the interaction range and the number of shoulders. A similar argument applies to the triangular binary target, where it is known that a single-component hard-core fluid favors a *global* triangular lattice, but achieving assemblies possessing the specific relative AA and BB ordering characteristic of the target lattice requires the binary interactions shown in Fig. 6.2(top). In short, the above observations indicate that the enhanced design space of binary systems can enable the self-assembly of structures also available to single-component systems (but with *simpler* interactions) as well as the self-assembly of significantly *more complex* structures than those attainable in a single-component system.

Focusing on binary assemblies, we can also gain some insight into the

mechanisms for their global stabilization by comparing the underlying component interactions to those of single-component systems optimized to stabilize similar local structures. Specifically, equation 6.1 recognizes that the binary system can comprise independent self and cross interactions that are optimized to recreate the RDFs of the target lattice. However, the equation alone does not clarify the extent to which the binary assembly can be considered a trivial superposition of sub-structures that can be stabilized by component self interactions (e.g., approximately equal to those expected from the analogous single-component target structure) versus a more cooperative, or coupled, assembly relying on nontrivial cross interactions. In order to help address this question, we compare the optimized self interactions of the binary system to analagous single-component interactions that stabilize the same *local* structure.

We begin by considering the square binary, triangular binary, and triangular honeycomb targets shown in Fig. 6.3 (top), 6.2 (top) and 6.2 (bottom), respectively. The underlying single-component structure is that of a square lattice for square binary AA or BB components and a honeycomb lattice for the BB component of both triangular binary and triangular honeycomb structures. As such, we can plot these individual component interactions and compare them to single-component interactions known to stabilize these lattices. [74] This comparison is shown in Fig. 6.5 for the optimized square lattice (a) and the honeycomb lattice (b) interactions where potentials are normalized such that $\phi(r)/\phi(1) = 1$. As seen, the square binary AA(BB) interaction

is largely similar, though not identical, to its single-component equivalent in range and complexity. The BB interactions for the triangular honeycomb and triangular binary (Fig. 6.5 b)) also approximate those of the reported honeycomb potential, though the triangular binary BB interaction deviates more strongly from the single-component results. This larger discrepancy, as we will show below, is an indication that individual component interactions need not exactly match their ideal local target lattice counterpart in order to achieve proper global assembly.

To investigate the above deviation more closely, we use one of the self (AA or BB) interactions from the optimized binary system to carry out a single-component assembly simulation at the same temperature and box size as the binary system, where the other component has been removed from the simulation box. We then compare the resulting equilibrium assemblies to the expected perfect local lattice for that component. To this end, we choose the simpler square binary structure (Fig. 6.3 top) and the more elaborate STH structure (Fig. 6.4 bottom) as two contrasting test cases. As seen in Fig. 6.6a) (top right), the square lattice is the local structure for the A(B) component in the square binary target. However, as shown in the bottom right of a), particles interacting via the AA interaction form a largely amorphous configuration. Despite this, the corresponding RDF for the extracted binary interaction (blue) shows a good match between the first two target square lattice coordination shells positions (note that, for this case, the AA pair interaction only spans the first two target coordination shells).

Similarly for the STH target structure, the A component locally forms a stretched truncated square lattice. However, particles interacting with the AA potential in a single-component simulation assemble into stripe-like phases. Nonetheless, comparing RDF peak positions shows good agreement with the target in the first three coordination shells which spans the full interaction range. Lastly, looking at the STH BB component assembly in c), we expect square clusters in a square super-lattice arrangement, but simulations yield rhomboid clusters in a triangular super-lattice orientation instead. While the peak positions in the RDFs do not overlap as closely as in Fig. 6.6a,b, visual comparison of the target and the formed assembly shows that the mean inter-cluster distance is approximately the same in both cases. Together, these results demonstrate that individual component interactions cannot be expected to fully recreate the underlying local target structure in the binary target but only to ensure proper local particle positioning on average. This is why the optimized interactions need not (and generally will not) closely match corresponding single-component target interactions; the latter fail to fully stabilize the local target structures and more specific coupling between interaction types must play a key role.

To further unravel the requirements for assembly of binary structures, we performed optimizations where one of the three interaction types was fixed as a hard-core-like [Weeks-Chandler-Andersen (WCA)] potential, while the rest were optimized as usual.[1]In particular, we consider the square binary tar-

[1]WCA-like here is defined as the normal repulsive WCA pair potential but with the

get from Fig. 6.3 (top) and carry out optimizations controlled for annealing schedule and iteration step so as to isolate the effects of fixing the interaction relative to the fully optimized system. Results for the square binary structure, where either AA(BB) or AB interactions are fixed, are shown in Fig. 6.7 (top or bottom, respectively). In the first case, fixed AA interactions resulted in stronger AB and BB interactions that helped boost global structure stability– though clearly not as efficiently as the fully optimized system (compare AA RDF, top right). This contrast is more drastic when AB (the cross-coupling) is fixed, resulting in sharpened AA and BB interactions that nevertheless fail to restore original system stability (broadened peaks for all RDFs, bottom right). Fixing one of the individual interactions as hard-core-like and optimizing the others does not work at all in assembling in the more complex binary structures. For instance, when such a procedure was carried for the STH lattice, it resulted in phase separation for fixed AA or BB interaction, or stripe-like configurations for fixed AB interaction (see Fig. I.2). Similar results held for the square corral structure.

Together, these results help to highlight the individual roles of self and cross interactions, respectively, in binary assemblies. For simple global targets like the square binary lattice, stronger AB and BB optimized interactions can compensate for a hard-sphere-like AA interaction to result in a successfully self-assembled target structure. However, for more intricate local orderings

---

Lennard-Jones power exponents changed from 12-6 to 4-2 and scaled by a factor of 100 for softer repulsions.

like those in the STH lattice, sharpening remaining interactions is not enough to compensate for a neutral interparticle interaction, resulting in a failed global assembly. Similarly, fixing the cross interaction places a larger load on self-self interactions to achieve correct local positioning, but these cannot stabilize relative component ordering *by definition* and as such this strategy results in reduced overall global stability for simple and complex targets alike.

To summarize, the analysis of Fig. 6.6-6.7 strongly suggests that global binary assembly can be understood as follows: self interactions act as a 'primer' that help ensure that individual component particles assemble into the right positional order (coordination shells), while cross interactions 'bind' the locally ordered particles into their correct, target positions.[2] This is why, despite the self interactions failing to assemble the target local structure in an analogous single-component system, they nonetheless encode the relevant length scales present in the local structure. In fact, substituting the optimized single-component square lattice interaction (which necessarily contains the characteristic length scales of a square) for the self-interactions in the intercalated square binary system results in successful assembly of the target, with greatly enhanced local AA(BB) stability as seen in the RDFs in Fig. I.3. The analysis also highlights the importance of the interplay among the self and cross interactions for intricate structures, as it is through mutual coupling that the

[2]There may be some apparent awkwardness in the use of a 'binder' analogy for purely repulsive systems. However, as noted in previous works [74], for the assemblies considered here, the effective forces mutually reinforce and lock particles into the correct position making the 'binding' analogy more fitting

entire global structure is locked into place. This result also implies that the self interactions that establish a necessary *local* structure may be much simpler than those required for an equivalent single-component system, so long as full system interactions are in place. Indeed, while the stretched truncated square *local* structure in the binary square corral could be achieved by the BB component interaction only spanning four coordination shells, the equivalent single-component truncated square interaction required five shells and resulted in poorer assembly (see Fig. I.4).

6.4 Conclusions

In this work, we extended a recently introduced inverse design methodology, relative entropy optimization, to discover new isotropic interactions that favor the formation of targeted multicomponent phases. We have used this approach here to determine interactions for binary mixtures that stabilize a wide variety of two-dimensional lattice assemblies and, in doing so, have gained new insights into how adopting a multicomponent system can affect the overall prospects for self assembly. Although the expanded parameter space for design in multicomponent systems increases the complexity of the design problem, it helps discover simpler interparticle interactions (as compared to single-component systems) to assemble a desired target phase. It also allows for designed assembly of complex phases with structures that cannot be stabilized by single-component materials.

Mechanistically, our results suggest that optimized interactions between

like components in a binary mixture act as a 'primer' to help ensure that such species adopt, on average, the correct positional order for the target phase. Cross interactions, in turn, act as a 'binder' to further ensure that species conform to the precise local compositional order required by the target. For complex or open lattices, independent design of cross and self interactions is required to stabilize the desired assemblies.

In future work, it will be interesting to pursue related inverse design calculations for classes of materials whose self and cross interactions are effectively constrained in ways that can be encoded by fundamental physics or empirical mixing rules.

6.5 Author Contributions

Work presented in this chapter was published in 2018 [123]. W.D.P extended the RE formulation, carried out RE optimization, molecular simulations, and performed data analysis. B.A.L. provided feedback on manuscript writing and data results. R.B.J and B.A.L. provided original RE code framework. T.M.T designed and funded the research.

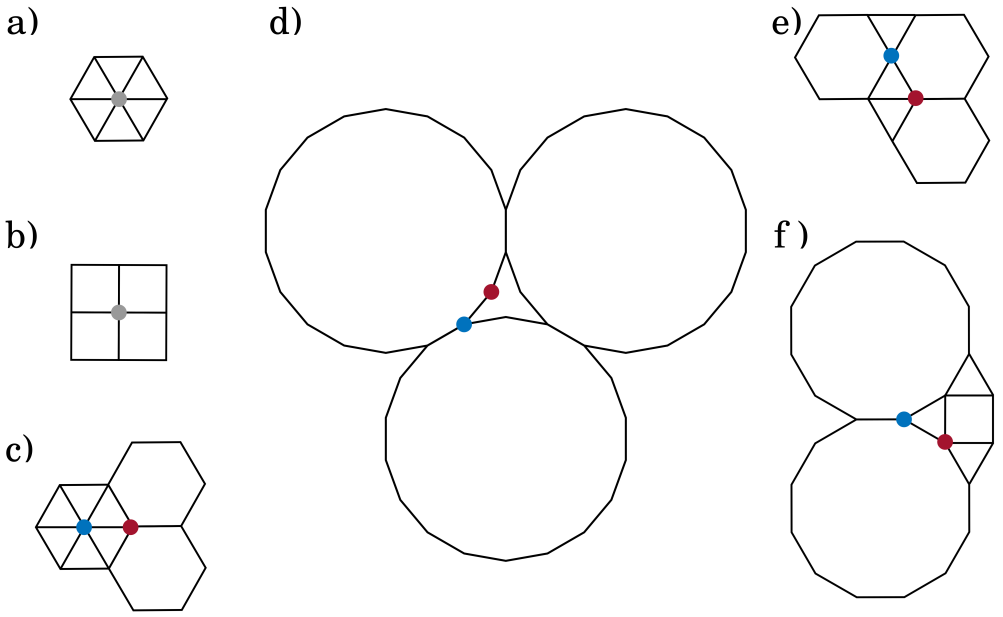

Figure 6.1: 1-uniform (grey dots) showing a) triangular $[3^6]$ and b) square $[4^4]$ vertices. The a) vertex is used to generate the triangular binary crystal while b) can be used to generate square binary, intercalated component rows forming single or double stripes as well as a structure consisting of a large open square with a component in the corners and the other at the sides (dubbed "square corral"). 2-uniform (blue and red dots) vertices showing c) $[3^6; 3^2.6^2]$ dubbed "triangular honeycomb" due to internal (blue) triangular and surrounding (red) hexagonal shapes d) $[18^2.3_{2\pi/9}]$ or "octadecagonal star binary" due to the octadecagonal and star polygons motifs e) $[3.6.3.6; 3^2.6^2]$ or "rectangular kagome" and f) $[3.12.12; 3.4.3.12]$ dubbed "square truncated hexagonal" due to the square super-orientation of the dodecagon shape in the tasselated structure.

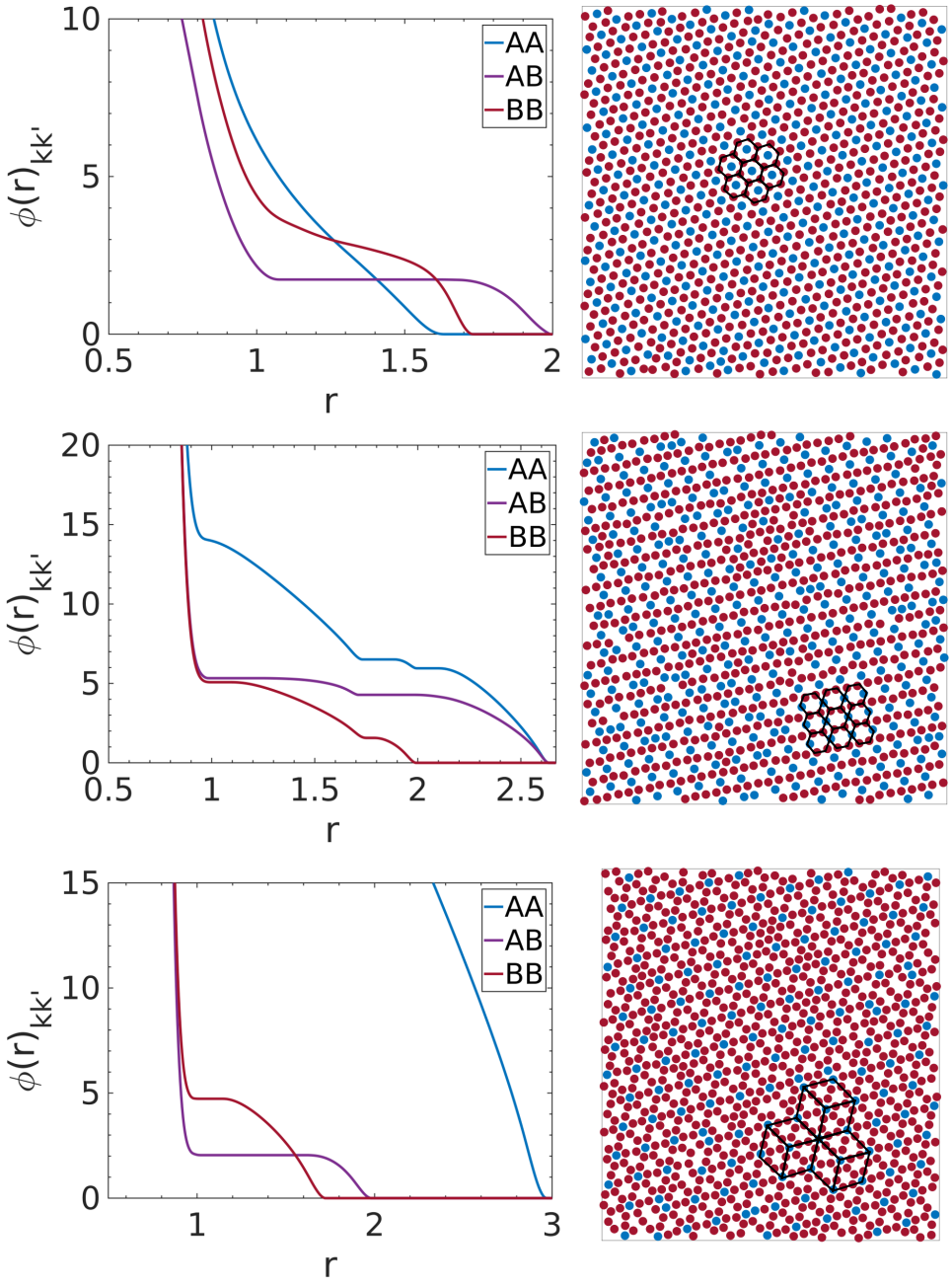

Figure 6.2: Optimized pair potentials and representative particle configurations for the triangular binary ($[3^6]$-top), rectangular kagome ($[3.6.3.6; 3^2.6^2]$-middle), and "triangular honeycomb" ($[3^6; 3^2.6^2]$-bottom) lattice assemblies. Black lines are drawn to highlight the ideal crystal structures.

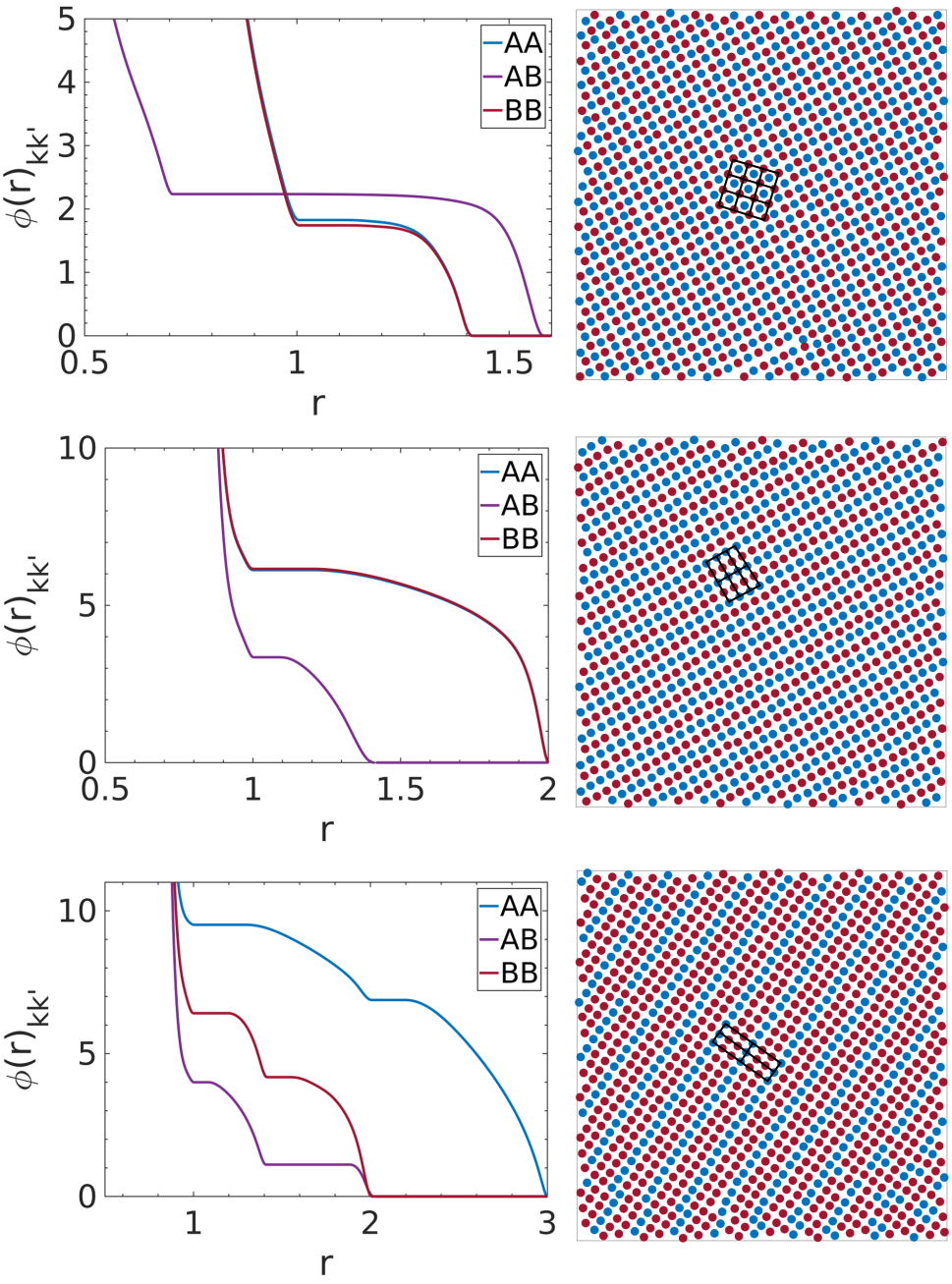

Figure 6.3: Optimized pair potentials and representative particle configurations for the square binary (top), square single stripe (middle), and square double stripe (bottom) lattice assemblies. Black lines are drawn to highlight the ideal crystal structures.

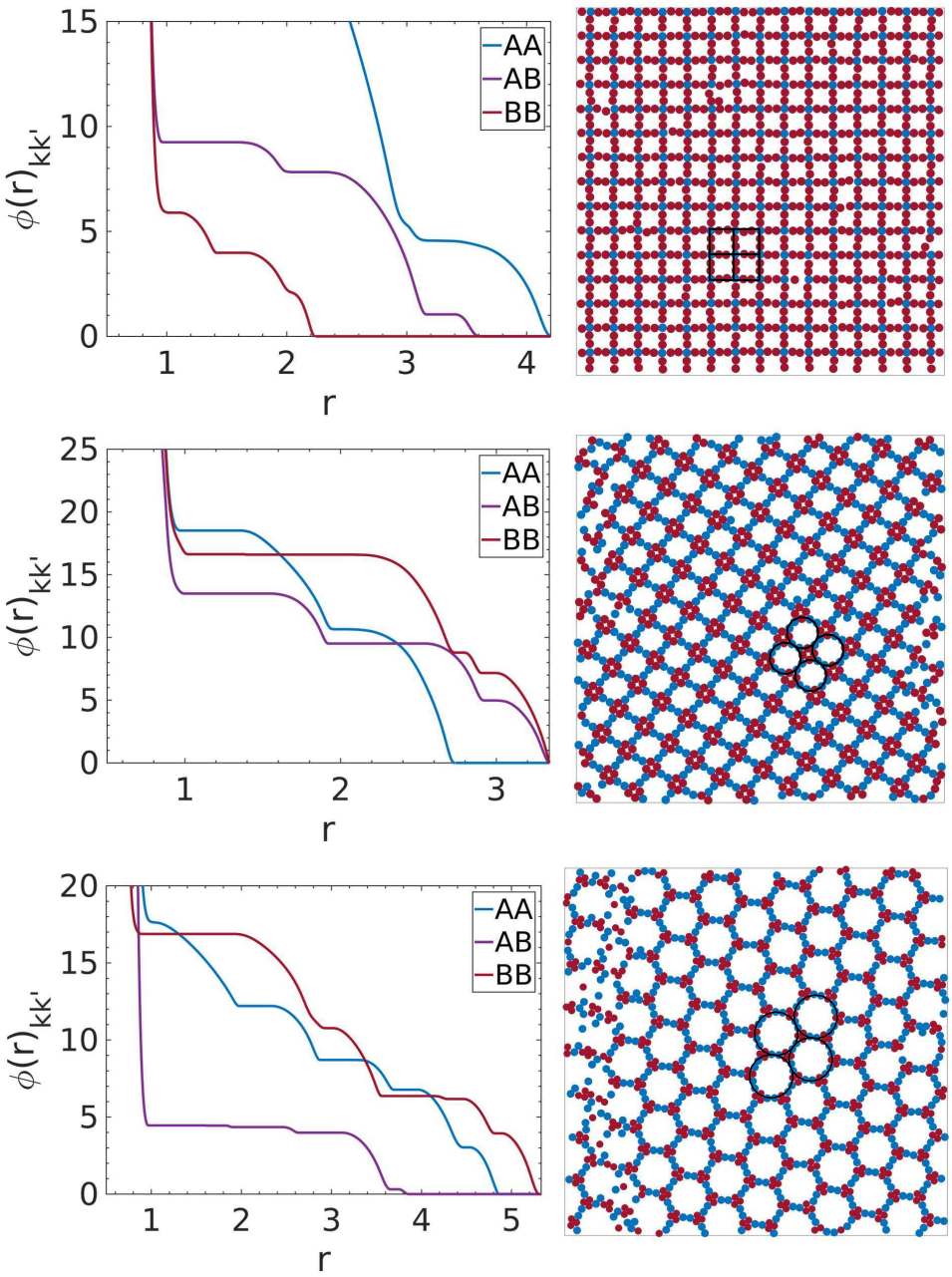

Figure 6.4: Optimized pair potentials and representative particle configurations for the square corral (top), square truncated hexagonal ([3.12.12; 3.4.3.12]-middle), and octadecagonal star binary ($18^2.3_{2\pi/9}$ - bottom) lattice assemblies. Black lines are drawn to highlight the ideal crystal structures.

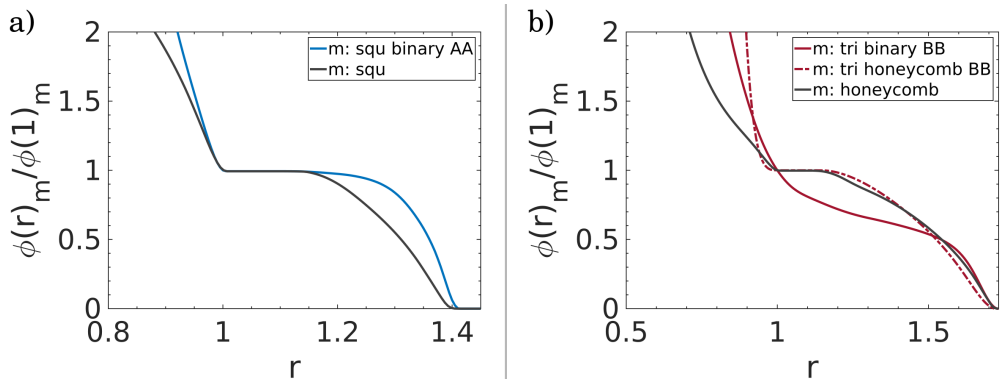

Figure 6.5: a) AA component of the optimized pair interaction for the square binary structure (blue) compared to that reported [74] for the single-component square structure (black). b) BB component of the optimized pair potential for the triangular binary (solid red) and triangular honeycomb binary (dash red) lattices compared to that reported for the honeycomb potential [74] (black).

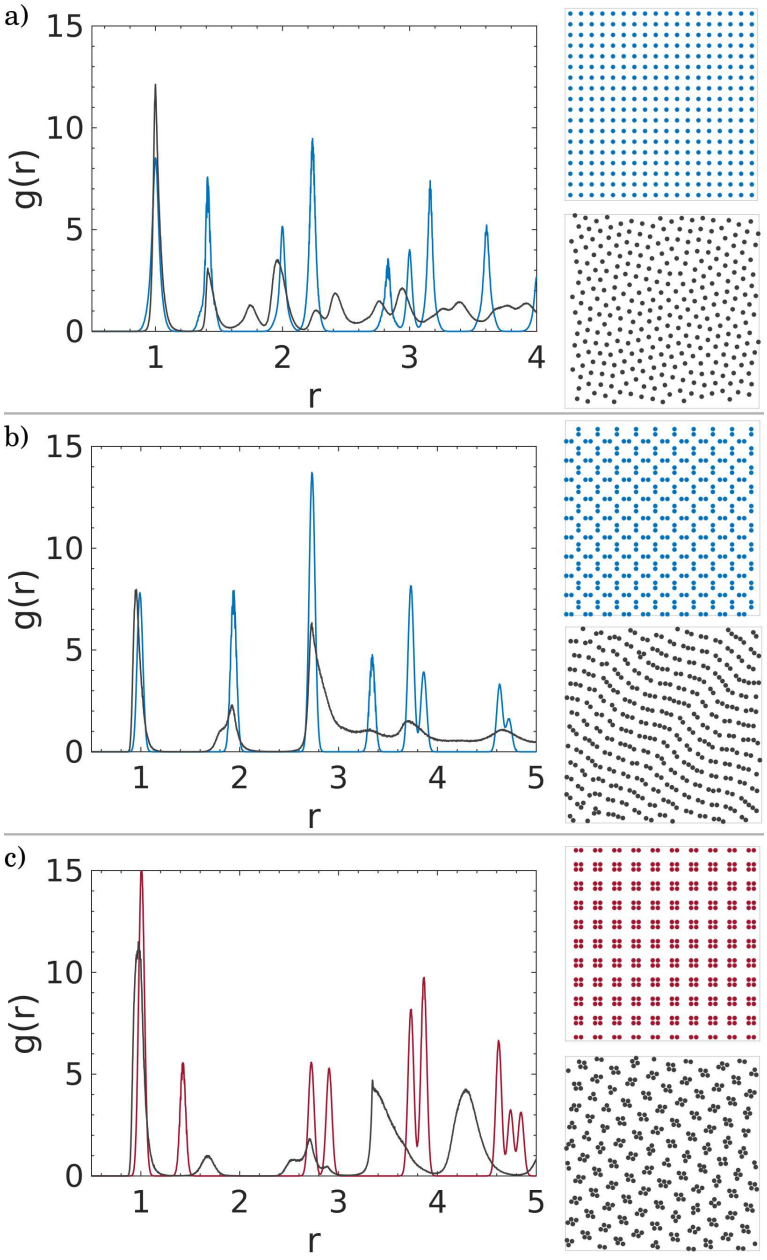

Figure 6.6: Radial distribution functions and configurations of single-component assemblies of particles interacting via optimized binary self interactions (blue or red) versus behavior in the fully optimized binary system (grey) for the a) square binary AA interaction (same as BB by symmetry) b) square truncated hexagonal AA interaction and c) square truncated hexagonal BB interaction.

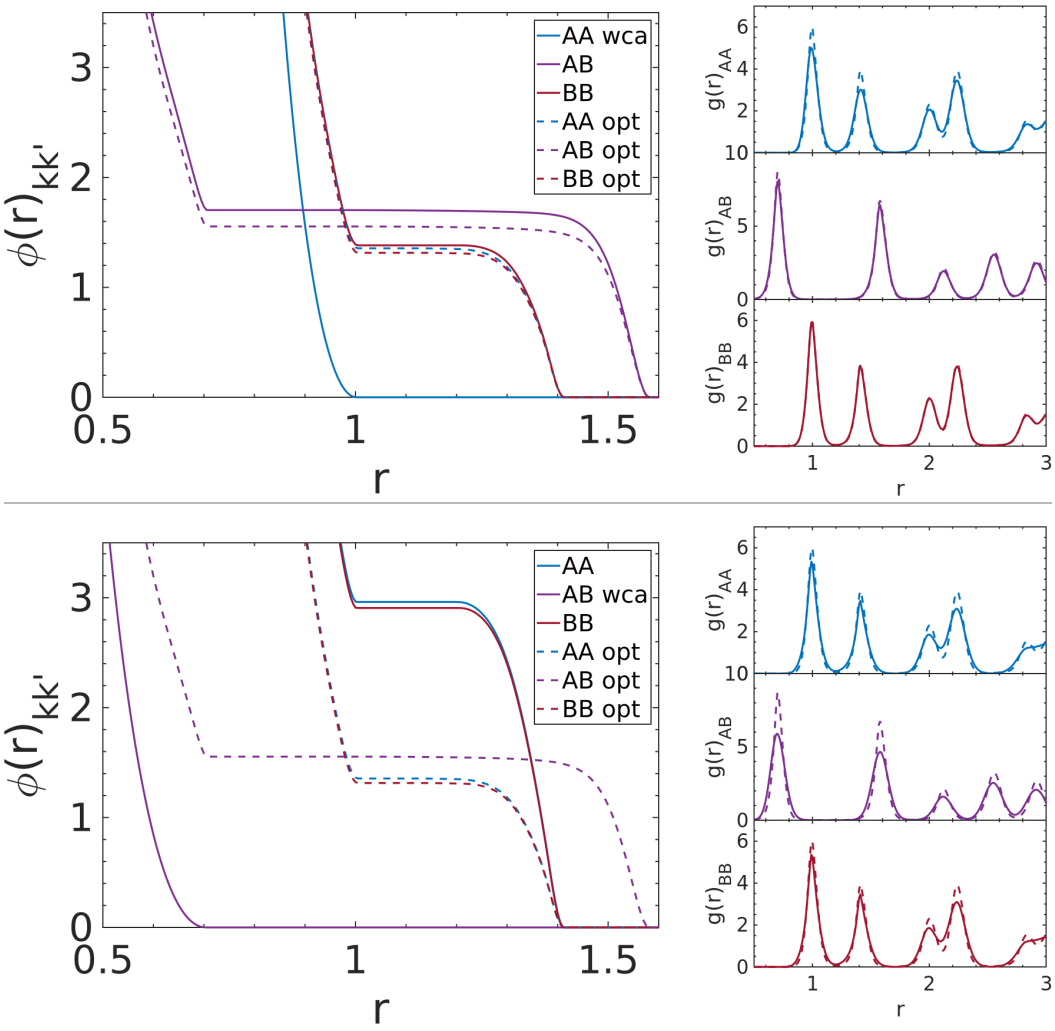

Figure 6.7: Optimized component interaction and radial distribution function comparison for square binary optimizations where the AA (top) and AB (middle) interactions have been fixed to display a simple WCA-like repulsive form described in the text. Note that, for both cases, the square binary assembly with fully optimized interactions leads to sharper RDF peaks at the target temperature.

Chapter 7

Outlook and Future Directions

As discussed throughout this thesis, inverse methodology offers a powerful design strategy for targeted material construction. While presented work suggests many fruitful future lines of study, here we propose three specific outlooks that may be readily applicable to current methods or hold particular scientific promise.

7.1 Application of Realistic Effective Colloidal Interactions for Inverse Design

Self-assembly of physical colloidal systems is ruled by a complex interplay of external and internal physical factors [1, 2] However, establishing a comprehensive link between the complex interactions and a simple but practical effective description of the system is highly non trivial, even in course grained descriptions that focus on the larger colloidal system and dominant pair-body forces (Van der Waals, depletion, electrostatic etc) [26, 28, 31]. As a result, presented work in this thesis yielded model interactions that served as a motivating proof of principle but were nonetheless not broadly amenable to experimental realization. As such, we envision the formulation of realistic physical models – specifically those that make explicit reference to phys-

ically determinable parameters – that may yield effective interaction models for experimentally realizable systems. This could be in the form of spherical nano-particles for which choice of passivating ligand properties, including size, charge, elasticity, amongst others could yield an effective isotropic interaction that promotes specific super-lattice assemblies. It could also apply to more elaborate anisotropic systems, such as domain-partioned "Janus" particles or directional "patchy" particles, whose interactions strengths, directions etc could be optimized for specific structural ordering. Inclusion of other relevant experimental conditions that integrate relevant crystallization methods such as drop casting, or solvent-induced flocculation, or particle size distributions e.g. polydispersity, would further advance the possible kind of 'design rule' insights extractable from the inverse design process. Overall, adapting presented inverse design methods for realistic design parameters would provide a directly relevant guide to experimentalists and holds great promise for achievable targeted structure design.

7.2 Attractive Interactions for Multicomponent Assembly

As presented in chapter 5, effective isotropic interactions for single component systems featuring a single attractive well fell into specific 'design rules'. While a variety of structures were achieved from application of these rules, the resulting interactions were as comparatevely elaborate as the equivalent purely repulsive interactions. In that sense, addition of an attractive well did

not simplify resulting interactions but served to highlight a minimum degree of complexity inherent to particular single component structures. However, as presented in chapter 6, introduction of additional components shows that equivalent structures may be achieved with simpler interactions when partitioned over the additional degrees of freedom of the resulting multi-component system. Furthermore, new interaction leverage is possible through coupled system effects that arise from cross-interactions and can result in simplified local self interactions. These specific multi-component properties, so far only demonstrated for the repulsive system in chapter 6, therefore revive interest in understanding how attractive interactions in the form of a single well may alter, or enhance the accessible design space of a multi-component system. Specifically, while work in chapter 5 demonstrated close parallel between resulting repulsive and attractive interaction profiles in single component systems, it is not clear that this result extrapolates to multi-component systems, specially considering that cross terms have no equivalent in the single component case. In fact, well tuned attractive cross-terms may help simplify resulting system interactions given the explicit binding force that brings components into the correct global structure (indeed, it was precisely a 'binding' analogy that was made to explain the overall global assembly in chapter 6).

Future efforts in this area would therefore seek to systematically investigate the role of attractive interactions in stabilizing multi-component systems. This work would necessarily categorize interaction combinations between systems partitioned to reflect [repulsive/attractive] self, and [attractive/repulsive]

cross interactions, with emphasis placed on achieving a target structure with the simplest interaction set. Implementation of such strategy could be readily achieved following the RE methodology already introduced in chapter 5 and 6. This enhanced design space may then not just help simplify known target interactions, but also help discover novel structures uniquely available to multi-component systems featuring attractions.

7.3 Inverse Methods for Non-equilibrium Assemblies

Assembly phenomena studied in this work has focused exclusively in equilibrium states i.e. self-assembled structures that represent the most stable thermodynamic state. However, target structures need not be limited to a well defined equilibrium configurations and can instead be realized by a variety of dynamic or energy driven processes [24, 124]. Indeed, the hallmark of biological self-assembly is its characterization as a non-equilibrium system that can maintain structure through dynamical couplings e.g. microtubule growth in the cellular membrane [125, 126]. Recently, examples of synthetic non-equilibrium self-assembly have been reported, and while these do not display the level of sophistication typical of natural systems, they nevertheless show it is possible to employ similar principles to achieve particular structures or function [127–129]. The particular promise shown by non-equilibrium self-assembly, however, strongly motivates the need for design strategies that can provide rational control over desirable structures. While fundamental descriptions of the non-equilibrium process are challenging questions of its own, recent

statistical mechanical advances are starting to provide a general foundation for non-equilibrium self-assembly as a design principle [130, 131].

Theoretical studies of synthetic non-equilibrium self-assembly have been recently published, showing that structure is directly controllable by dynamic parameters such as driven forces [132], or chemical/diffusion reactions [133]. Furthermore, most of the assembling structures were shown to be unique for the driven non-equilibrium state and demonstrate how dynamic parameters can expand the available configurational space to achieve novel system structures. In this light, applying an inverse design perspective to non-equilibrium self-assembly may provide a particularly rich opportunity. In particular, any such implementation would necessarily have to include the appropriate level of theory in order to cast dynamic parameters as optimizible decision variables. Further, it must permit for dynamical update of variables using configurational feedback extracted directly from an accurately simulated self-assembling state. In both fronts, the RE method of chapters 5 and 6 may readily provide such optimization framework given that RE is directly expandable from an appropriate theoretical description that allows for "on the fly" optimization of the decision variables. In this manner, non-equilibrium assembly might be amenable to the same kind of inverse design methodology as work presented throughout this thesis, while providing a rational path for dynamic assembly control.

In all, expanding the reach of inverse design methods to exploit non-equilibrium self-assembly is an exciting research direction that may allow rich

understanding of the underlying dynamics as well as open novel opportunities for adaptable material design.

Appendices

Appendix A

Free Parametrization of n-Basis Crystals for Forward Crystal Discovery

In carrying out the forward calculation of the ground-state structures from a pair potential described in chapters 2 - 4, one must determine the optimal values of any possible variable parameters for the lattices that minimize their chemical potential. For example, in the case of a Bravais lattice, one finds optimal values of aspect ratio b/a and primitive vector angle θ. Here, we show a generilization of this scheme and consider free variable primitive vectors with multiple freely parametrized basis.

Concretely, we consider a variable primitive lattice cell with [b/a, θ] and include freely varying basis parameters [b_i/a,θ_i] where i indicates the basis number up n such basis considered. Further, these basis are constrained to avoid superposition (i.e. distances between bases > 0) and to remain within the primitive cell (e.g. $b_i/a \times \sin\theta_i < b/a \times \sin\theta$ etc). Physical quantities (energy, pressure etc) are then computed using standard formulation and the particle configuration that gives the lowest chemical potential found. We note a similar procedure was also used by Batten et al for a comparable forward calculation [107].

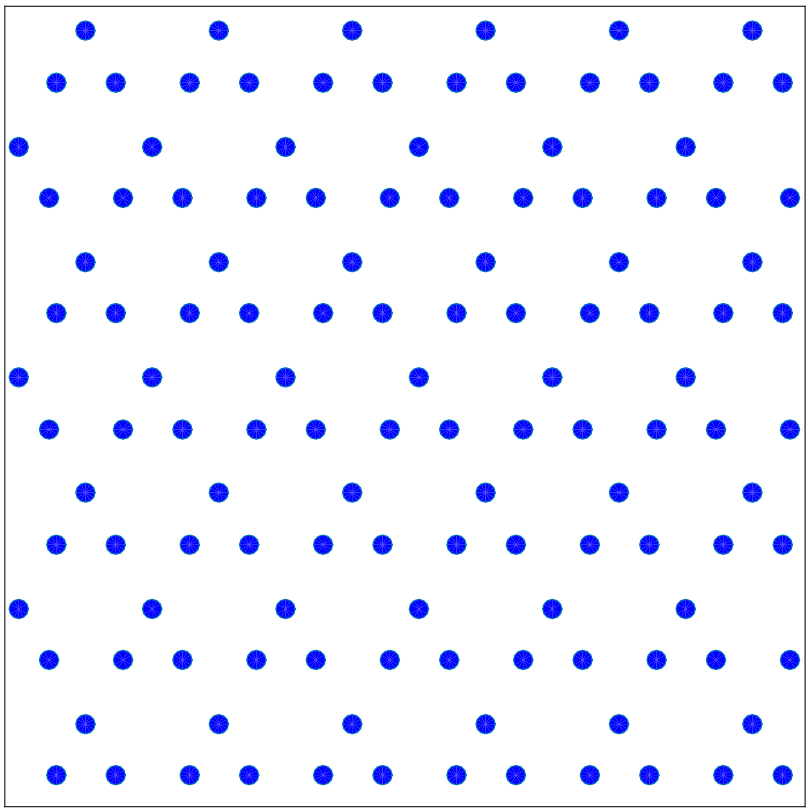

Figure A.1: Illustration of the ‘Kagome-B’ competing structure.

As a representative example, we describe the non-standard lattices found for the kagome and snubquare targets in chapter 3 by this method. Specifically, for the kagome design target this resulted in a distorted honeycomb (2 basis: 1 primitive, 1 additional) with parameters $[b/a = 1.114, \theta = 1.117, b_1/a = 0.877, \theta_1 = 0.663]$; and 'kagome-B', a kagome lattice with non-uniform aspect ratio (3 basis: 1 primitive, 2 additional–see figure A.1 for an illustration) with parameters $[b/a = 1, \theta = \pi/3, b_1/a = 0.447, \theta_1 = 0, b_2/a = 0.447, \theta_2 = \pi/3]$. Similarly for snub square, a distorted snub square was found (4 basis: 1 primitive, 3 additional) with parameters $[b/a = 1, \theta = \pi/2, b_1/a = 0.518, \theta_1 = 1.348, b_2/a = 0.506, \theta_2 = 0.223, b_3/a = 0.865, \theta_3 = 0.796]$.

Appendix B

Potential Shape Sensitivity Analysis

In this appendix we provide a rudimentary sensitivity analysis of the potential forms used in chapters 2-4 in stabilizing the targeted structures. While a comprehensive analysis is outside the scope of this work, it is possible to draw an approximate picture of the sensitivity of the potentials by perturbing specific features of the potential and evaluating the corresponding effects on the target stability. In particular, we consider the force $-\phi'(r/\sigma)$ (i.e. the negative gradient of the potential) where small changes to the potential form are more readily apparent. Given the potential functional in eq. 2.1 introduced in chapter 2 and used in chapter 3, the force can be shown to be

$$-\phi(r/\sigma)' = \epsilon/\sigma\{nA(r/\sigma)^{-n-1} + \sum_{i=1}^{2} k_i l_i \mathrm{sech}(k_i(r-d_i))^2 + f'_{\mathrm{shift}}(r/\sigma)\}H[(r_{\mathrm{cut}}-r)/\sigma]. \tag{B.1}$$

where, σ and ϵ represent characteristic length and energy scales respectively; H is the Heaviside function; $\{A, n, \lambda_i, k_i, \delta_i\}$ are variable parameters; r_{cut} is a cut-off radius; and f_{shift} is a polynomial function of the form $f'_{\mathrm{shift}}(r/\sigma) = (-2Px^2 - Q)$ to ensure $\phi'(r_c/\sigma) = 0$ where r_c is the cut off radius. The expression can be more easily understood by considering each term separately

to understand their respective functional contributions to the total force. As such, the first component consists of the softly repulsive term $nA(r/\sigma)^{-n-1}$ that makes the 'core' of the total force expression; the second is the hyperbolic secant term $k_i l_i \text{sech}(k_i(r-d_i))^2$ which creates pulse-like contributions (negative or positive) and resemble 'steps' (or plateaus) in the total force (see figures 3.1a or 3.4a in chapter 3 for illustrations). The last term, the polynomial f'_{shift}, can take on more complex roles depending on the exact interplay of the steps and core but usually assumes the simpler role of shifting the system up or down to ensure a smooth cut off.

With this in mind, we explore the sensitivity of a given potential form on the target structure by making small perturbations to the parameters comprising the seperate shape features (core or steps) and then carry out a forward calculation to determine the ground state phase diagram. For this initial investigation, we simply compare the target structure across its stable density range against a very large group of standard competitors and their variations (both bravais and non-bravais) for which the target is otherwise the ground state structure. Any instability (i.e. $\mu_t - \mu_l < 0$, where μ_t is the target chemical potential and μ_l is that of a competitor) would thus mark an unstable perturbation of the parameters.

Using this approach, we have carried out a representative sensitivity analysis for the first snub square potential of chapter 3 (i.e. SS-A) by perturbing determining parameters of the core, and step features by a small percentage of their optimal value. First, we perturb parameters A, l_1 and l_2 by $\pm 10\%$

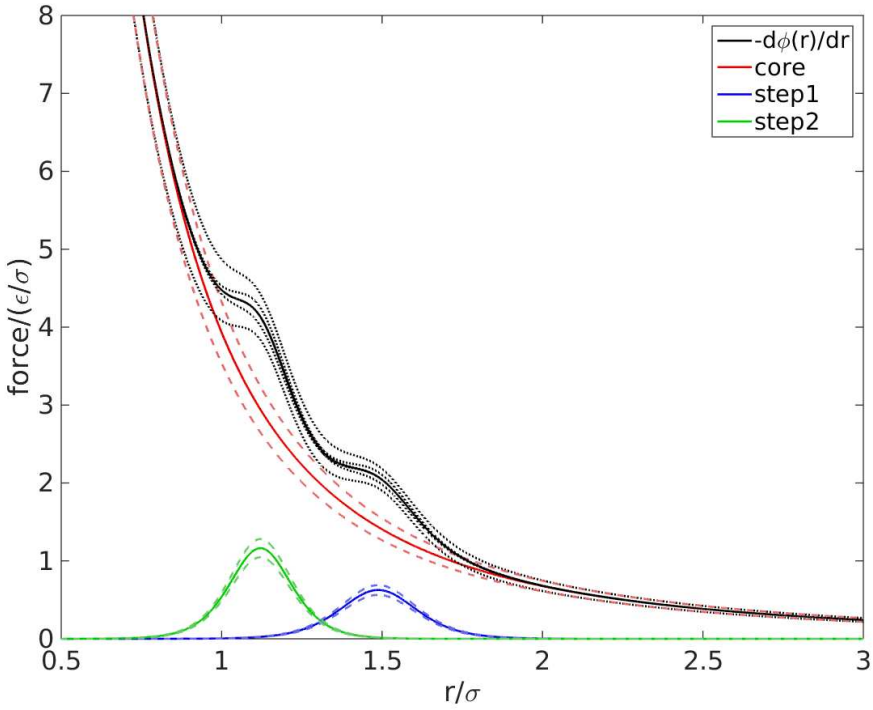

Figure B.1: Total force, individual contributions and variations on the A,l_1, and l_2 parameters by ± 0.1 the optimized value. Shift term f'_{shift} and cut off not shown explicitly for clarity.

which represent the 'amplitudes' of the core and steps respectively. This is shown in figure B.1 where solid lines indicate optimal values and dashed lines perturbations for the core (red), steps (green and blue), and the resulting total forces shown in black. Note that figure B.1 omits the polynomial term f'_{shift} since for this potential it simply shifts the system up and down without altering the final force shape (as long as $r_c \sim\geq 2$). As seen, changing these parameters only alters the relative magnitude of the force but conserves the position and shape of each of its optimal features. As a result, we can expect that

upon renormalization and cut off application through r_c (i.e. $\phi''(r/\sigma) > 0$ and $\phi(1/\sigma) = 1$), the perturbed force will have a small effect on the target structure stability. Indeed, forward calculation of these perturbed forces showed the structure conserved most of its stable density range albeit at a reduced chemical potential advantage $\Delta\mu \sim= 0.006$ at optimization density ρ_o. This result held even if we allowed convexity and/or normalization to be broken by fixing r_c to its optimal value of 2σ. In other words, perturbing the amplitude of the core or steps predictably conserved the overall shape of the force which allowed the target to remain stable for most of its range.

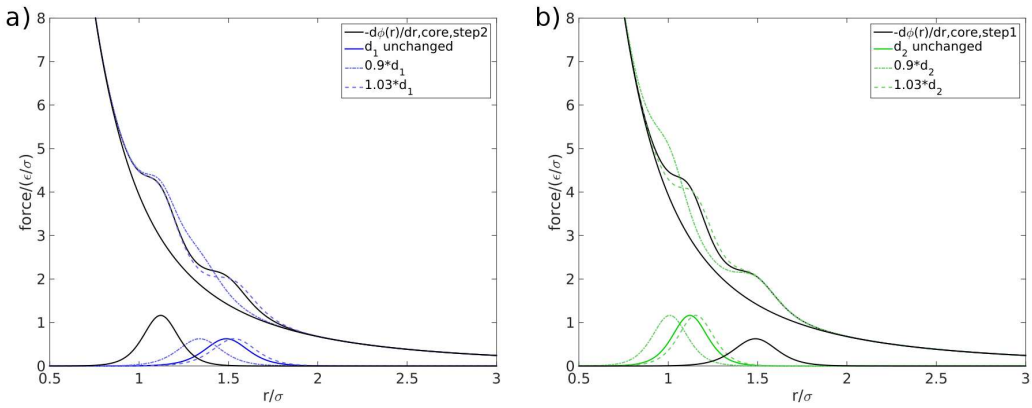

Figure B.2: Total force and variations on a) parameter d_1 and b) parameter d_2. Black solid lines denote force for unchanged parameters.

On the other hand, altering the *position* of these features had drastically different consequences. This is shown in figure B.2 where the steps positions are shifted left by 10% (dash dot lines) and right by 3% (dashed lines) through the parameters d_1 (b) and d_2 (a). As seen, while the perturbations are comparable or smaller to the amplitude perturbations, the effect on

the total force is notable but asymmetrical depending if they are shifted right or left. For instance, while shifting left obscured the step feature, shifting right had the more subtle effect of rapidly destroying convexity. Furthermore, since these perturbations change the step profile so drastically, ensuring convexity of the potential came at expense of the renormalization condition or vice versa (i.e. those that could be easily captured with judicious choice of r_c rather than those requiring change of other potential parameters that would obscure the original perturbation). This also explains the difference in perturbation magnitude beteween left 10% and right 3%, since shifting right had a stronger impact on convexity than what could be remedied through r_c.

Despite the difference in perturbation, the result was the same: complete destabilization of the target across all densities though for different reasons depending on step. For instance, shifting the left step destabilized the target relative to the triangular lattice whose instability depends on penalizing its compact first coordination shell. Similarly, changing the right step destibilized the target relative to the square lattice as a result of changing the shape which penalized square coordination shells at these distances. Both results are consistent with our analysis in chapter 3 where a similar double step form in $\psi(r)$ helped stabilized the snub square structure relative to competitors. This is also similar to the differences between the SS-A and SS-B potential where the latter's shorter ranged features around optimal coordination shell distances at ρ_o achieved a stronger $\Delta\mu$ advantage but at the expense of a reduced stable density range, showing it is the position and length of the plateaus that affect

this difference.

In conclusion, dissecting the potential form to its individual features and perturbing the relevant parameters controlling them shows that our optimized potentials are robust to small changes that conserve the overall *shape* of the force, whereas any changes that rapidly alter its shape have the effect of destabilizing the target structure. This means that the senstivity of these potentials is not tied to its individual parameters values, but to the way parameters control the net interaction features that stabilize the target structure. For this reason the parameter values of the second snub square potential (SS-B) have no apparent similarity to those of SS-A, yet the resulting interaction profile is similar (a double plateau feature shown in chapter 3). Overall, we have qualitatively demonstrated that reported potentials map out general features necessary to stabilize the design target and the resulting ground state stability will be conserved so long as key features are broadly observed.

Appendix C

Binary Mixture Competitor Forward Calculation Formulation

Binary mixture competitor calculation follows directly from a basic treatment of binary phase equilibrium and solved numerically by means of the mathemetical software GAMS. Briefly, we consider a box of constant volume (V), particles (N) and temperature (T). In this canonical ensemble the system may spontaneously phase separate so as to lower the overall system free energy. For our crystal design process, we consider two crystals l_1 and l_2 at respective densities $\rho_1 = N_1/V_1$ and $\rho_2 = N_2/V_2$ inside a box of total volume V and number of particles N (i.e. system density $\rho = N/V$) co-existing in some relative molar fraction $x_2 = N_2/N$ and $x = 1 - x_2$. Since both crystals must occupy the entire box and conserve the total number of particles we can relate x to ρ, ρ_1 and ρ_2 as

$$(1 - x) = \frac{1/\rho - 1/\rho_1}{1/\rho_2 - 1/\rho_1} \tag{C.1}$$

Next, for two phases to co-exist, the common tangent condition states that they must be at equal pressure and chemical potential. This means that

$$P_1 = P_2 \tag{C.2}$$

and

$$U_1 + P_1/\rho_1 = U_2 + P_2/\rho_2 \tag{C.3}$$

where U_i and P_i denote energies and pressures for each crystal l_1 and l_2 respectively. Both of these quantities are computed from standard expressions and the energy is given by

$$U_i = \frac{1}{2}\sum_{i \neq j} \phi(r_{ij}(\rho_i)) \tag{C.4}$$

where $\phi(r)$ is the pair potential given in eq. 1 of the main text and $r_{ij}(\rho_i)$ indicates all pair interactions positions at respective density ρ_i drawn from the ground state radial distribution for each lattice l_i. The pressure is computed from the virial as

$$P_i = -\frac{1}{4}\rho_i \sum_{i \neq j} r_{ij}(\rho_i)\phi'(r_{ij}(\rho_i)) \tag{C.5}$$

where $\phi'(r)$ indicates derivative with respect to r. These equations define the system physics and constitute the bulk of the non-linear problem solved in GAMS. In addition to those equations, we use the following auxiliary equations for each crystal to constrain the range of the possible ρ_i as

$$r_c^2/d_0 > 1 \tag{C.6}$$

where r_c indicates the interaction cut-off radius, and d_0 the nearest neighbor distance for each l_i at ρ_i. Finally, the objective function used to optimize the system is chosen to minimize the net free energy of the system i.e.

$$U_{\text{tot}} = (1 - x)(U_2 - U_1) + U_1 \tag{C.7}$$

In this manner, given some starting $\phi(r)$ interaction and a chosen pair l_1, l_2 (from a large set of combinations of common and specialized lattices), any binary mixture that lowers the free energy of the sytem U_{tot} relative to a desired target is considered a competitor and added to the competitor pool for another target optimization iteration.

Appendix D

Derivation of the Well Minimum Position Update Scheme for a Spline Potential

Consider a knot in the Akima spline whose position is denoted by r_o. Consider further a continuous functional representation of the spline at the ith iteration as f_i with r_o as a parameter, namely $f_i(r-r_o)$. Taking the derivative of f_i with respect to r we define a new function g as

$$g_i(r - r_o) \equiv f_i'(r - r_o) \tag{D.1}$$

Now suppose that the location of the well minimum for the current ith iteration is given by r_o. We can consider small changes around this minimum by doing a Taylor expansion on $g_i(r - r_o)$. Therefore

$$\begin{aligned} g_i(r - r_o) &= g_i(r_o) + g_i'(r_o)(r - r_o) + ... \\ g_i(r - r_o) &\approx m(r - r_o) \end{aligned} \tag{D.2}$$

where for the last equation $g_i(r_o) = 0$ by definition and $m \equiv g_i'(r_o)$, denotes the slope of a line. Consider now the iteration $i + 1$ where the Akima point freely changes by a small value $+\delta g$. From eq. D.2 we then have approximately

$$g_{i+1}(r - r_o) \approx \delta g + m(r - r_o) \tag{D.3}$$

and can determine the new minimum point r_n by setting $g_{i+1}(r_n - r_o) = 0$. Using eq. D.3 and solving for r_n we get

$$r_n = r_o - \delta g/m \tag{D.4}$$

In practice, we work with the negative difference of the Akima spline points for convinience i.e. $-g$. Therefore $m \equiv -m$ and eq. D.4 becomes

$$r_n = r_o + \delta r \tag{D.5}$$

where $\delta r \equiv \delta g/m$. A similar procedure for $-\delta g$ change in the akina knot at r_o yields

$$r_n = r_o - \delta r \tag{D.6}$$

Therefore, the update scheme is implemented as follows. If the Akima spline point r_o which is also the minimum at the ith iteration changes by $+\delta g$ in the next iteration i+1, the new minimum position is defined as $\min(g_{i+1}(r_o), g_{i+1}(r_{o+1}))$ where r_{o+1} indicates the spline point immediately to the right of r_o i.e. the point closest to 0 magnitude is defined as the new minimum for that iteration. The equivalent rule for $-\delta g$ is $\min(g_{i+1}(r_o), g_{i+1}(r_{o-1}))$, where r_{o-1} indicates a spline point immidiately to the left of r_o.

Appendix E

Derivation of relative entropy update scheme for a multicomponent system

In this appendix we provide a brief derivation of the update scheme shown in equation 6.1 in chapter 6. Without loss of generality, consider i independent configurations of a two component system given by coordinates $\mathbf{R_i^{(A)}}$ and $\mathbf{R_i^{(B)}}$. Then in a canonical ensemble the probability of such configuration is given by the product of the Boltzmann factors

$$P(\mathbf{R_i^{(A)}}, \mathbf{R_i^{(B)}}|\boldsymbol{\theta}) = \prod_{i=1}^{M} \exp\left[-\beta U(\mathbf{R_i^{(A)}}, \mathbf{R_i^{(B)}}|\boldsymbol{\theta})\right]/Z(\boldsymbol{\theta}) \tag{E.1}$$

where $U(\mathbf{R_i^{(A)}}, \mathbf{R_i^{(B)}})$ is the configuration energy, $\beta = 1/k_b T$, T is temperature, k_b is the Boltzmann constant, and $\boldsymbol{\theta}$ is a vector of the tunable potential parameters. As explained in detail in previous work [74], given some desired configuration $(\mathbf{R^{(A)}}, \mathbf{R^{(B)}})$, we seek to maximize the likelihood of achieving this target given some parameters $\boldsymbol{\theta}$, i.e. we must maximize $P(\mathbf{R_i^{(A)}}, \mathbf{R_i^{(B)}}|\boldsymbol{\theta})$ with respect to $\boldsymbol{\theta}$. In practice, it is easier to maximize the log of the probability. Applying a log to eq. E.1 and expanding we get

$$\frac{1}{M} \ln P(\mathbf{R_i^{(A)}}, \mathbf{R_i^{(B)}}|\boldsymbol{\theta}) = -\frac{1}{M} \sum_{i=1}^{M} \beta U(\mathbf{R_i^{(A)}}, \mathbf{R_i^{(B)}}|\boldsymbol{\theta}) - \ln Z(\boldsymbol{\theta}) \tag{E.2}$$

We can now partition the system energy as a sum of independent self and cross component interactions as

$$U(\mathbf{R_i^{(A)}}, \mathbf{R_i^{(B)}}|\boldsymbol{\theta}) = \\ U^{(A,A)}(\mathbf{R_i^{(A)}}|\boldsymbol{\theta}^{(A,A)}) + U^{(B,B)}(\mathbf{R_i^{(B)}}|\boldsymbol{\theta}^{(B,B)}) + U^{(A,B)}(\mathbf{R_i^{(A)}}, \mathbf{R_i^{(B)}}|\boldsymbol{\theta}^{(A,B)}) \tag{E.3}$$

where $\boldsymbol{\theta}$ has been similarly split into self and cross parameters $\boldsymbol{\theta} = [\boldsymbol{\theta}^{(A,A)}, \boldsymbol{\theta}^{(B,B)}, \boldsymbol{\theta}^{(A,B)}]$ and plugging back into eq. E.2 we get:

$$\begin{aligned} \frac{1}{M} \ln P(\mathbf{R_i^{(A)}}, \mathbf{R_i^{(B)}}|\boldsymbol{\theta}) = \\ &- \frac{1}{M} \sum_{i=1}^{M} \beta U^{(A,A)}(\mathbf{R_i^{(A)}}|\boldsymbol{\theta}^{(A,A)}) \\ &- \frac{1}{M} \sum_{i=1}^{M} \beta U^{(B,B)}(\mathbf{R_i^{(B)}}|\boldsymbol{\theta}^{(B,B)}) \\ &- \frac{1}{M} \sum_{i=1}^{M} \beta U^{(A,B)}(\mathbf{R_i^{(A)}}, \mathbf{R_i^{(B)}}|\boldsymbol{\theta}^{(A,B)}) - \ln Z(\boldsymbol{\theta}) \end{aligned} \tag{E.4}$$

which can be written

$$\begin{aligned} \langle \ln P(\mathbf{R^{(A)}}, \mathbf{R^{(B)}}|\boldsymbol{\theta}) \rangle_{P_{\text{tgt}}(\mathbf{R^{(A)}}, \mathbf{R^{(B)}})} = \\ &- \langle \beta U^{(A,A)}(\mathbf{R^{(A)}}|\boldsymbol{\theta}^{(A,A)}) \rangle_{P_{\text{tgt}}(\mathbf{R^{(A)}}, \mathbf{R^{(B)}})} \\ &- \langle \beta U^{(B,B)}(\mathbf{R^{(B)}}|\boldsymbol{\theta}^{(B,B)}) \rangle_{P_{\text{tgt}}(\mathbf{R^{(A)}}, \mathbf{R^{(B)}})} \\ &- \langle \beta U^{(A,B)}(\mathbf{R^{(A)}}, \mathbf{R^{(B)}}|\boldsymbol{\theta}^{(A,B)}) \rangle_{P_{\text{tgt}}(\mathbf{R^{(A)}}, \mathbf{R^{(B)}})} \\ &- \ln Z(\boldsymbol{\theta}) \end{aligned} \tag{E.5}$$

where $\langle ... \rangle$ denotes ensemble average. In order to achieve a desired target probability we can optimize component parameters $\boldsymbol{\theta}^{k,k'}$, where $k,\ k' = A$ or

B, using a gradient ascent approach of the form:

$$\boldsymbol{\theta}_{i+1} = \boldsymbol{\theta}_i + \alpha[\boldsymbol{\nabla}_{\boldsymbol{\theta}} \langle \ln P(\mathbf{R}^{(\mathbf{A})}, \mathbf{R}^{(\mathbf{B})}|\boldsymbol{\theta})\rangle]_{\boldsymbol{\theta}_i} \tag{E.6}$$

where α is some scalar constant. Using

$$Z(\boldsymbol{\theta}) \equiv \int \exp[-\beta U(\mathbf{R}^{(\mathbf{A})}, \mathbf{R}^{(\mathbf{B})}|\boldsymbol{\theta})] d\mathbf{R}^{(\mathbf{A})} d\mathbf{R}^{(\mathbf{B})} \tag{E.7}$$

where $d\mathbf{R}^{(\mathbf{A})} d\mathbf{R}^{(\mathbf{B})}$ indicate hyper-volume elements, and computing the gradient we have

$$\begin{aligned}
\boldsymbol{\nabla}_{\boldsymbol{\theta}^{(A,A)}} \langle \ln P(\mathbf{R}^{(\mathbf{A})}, \mathbf{R}^{(\mathbf{B})}|\boldsymbol{\theta})\rangle_{P_{\mathrm{tgt}}(\mathbf{R}^{(\mathbf{A})}, \mathbf{R}^{(\mathbf{B})})} = \\
- \langle \boldsymbol{\nabla}_{\boldsymbol{\theta}^{(A,A)}} \beta U^{(A,A)}(\mathbf{R}^{(\mathbf{A})}|\boldsymbol{\theta}^{(A,A)})\rangle_{P_{\mathrm{tgt}}(\mathbf{R}^{(\mathbf{A})}, \mathbf{R}^{(\mathbf{B})})} \\
+ \langle \boldsymbol{\nabla}_{\boldsymbol{\theta}^{(A,A)}} \beta U^{(A,A)}(\mathbf{R}^{(\mathbf{A})}|\boldsymbol{\theta}^{(A,A)})\rangle_{P(\mathbf{R}^{(\mathbf{A})}, \mathbf{R}^{(\mathbf{B})})}
\end{aligned} \tag{E.8a}$$

$$\begin{aligned}
\boldsymbol{\nabla}_{\boldsymbol{\theta}^{(B,B)}} \langle \ln P(\mathbf{R}^{(\mathbf{A})}, \mathbf{R}^{(\mathbf{B})}|\boldsymbol{\theta})\rangle_{P_{\mathrm{tgt}}(\mathbf{R}^{(\mathbf{A})}, \mathbf{R}^{(\mathbf{B})})} = \\
- \langle \boldsymbol{\nabla}_{\boldsymbol{\theta}^{(B,B)}} \beta U^{(B,B)}(\mathbf{R}^{(\mathbf{B})}|\boldsymbol{\theta}^{(B,B)})\rangle_{P_{\mathrm{tgt}}(\mathbf{R}^{(\mathbf{A})}, \mathbf{R}^{(\mathbf{B})})} \\
+ \langle \boldsymbol{\nabla}_{\boldsymbol{\theta}^{(B,B)}} \beta U^{(B,B)}(\mathbf{R}^{(\mathbf{B})}|\boldsymbol{\theta}^{(B,B)})\rangle_{P(\mathbf{R}^{(\mathbf{A})}, \mathbf{R}^{(\mathbf{B})})}
\end{aligned} \tag{E.8b}$$

$$\begin{aligned}
\boldsymbol{\nabla}_{\boldsymbol{\theta}^{(A,B)}} \langle \ln P(\mathbf{R}^{(\mathbf{A})}, \mathbf{R}^{(\mathbf{B})}|\boldsymbol{\theta})\rangle_{P_{\mathrm{tgt}}(\mathbf{R}^{(\mathbf{A})}, \mathbf{R}^{(\mathbf{B})})} = \\
- \langle \boldsymbol{\nabla}_{\boldsymbol{\theta}^{(A,B)}} \beta U(\mathbf{R}^{(\mathbf{A})}, \mathbf{R}^{(\mathbf{B})}|\boldsymbol{\theta}^{(A,B)})\rangle_{P_{\mathrm{tgt}}(\mathbf{R}^{(\mathbf{A})}, \mathbf{R}^{(\mathbf{B})})} \\
+ \langle \boldsymbol{\nabla}_{\boldsymbol{\theta}^{(A,B)}} \beta U^{(A,B)}(\mathbf{R}^{(\mathbf{A})}, \mathbf{R}^{(\mathbf{B})}|\boldsymbol{\theta}^{(A,B)})\rangle_{P(\mathbf{R}^{(\mathbf{A})}, \mathbf{R}^{(\mathbf{B})})}
\end{aligned} \tag{E.8c}$$

which correspond to three independent equations for each parameter k, k'. Supposing isotropic pair interactions of the form

$$U^{(k,k)}(\mathbf{R}^{\mathbf{k}}|\boldsymbol{\theta}^{(k,k)}) \equiv \frac{1}{2} \sum_{i \neq j}^{N^{(k)}} u^{(k,k)}(r_{i,j}^{(k)}|\boldsymbol{\theta}^{(k,k)}) \tag{E.9}$$

for self and

$$U^{(k,k')}(\mathbf{R}^{(\mathbf{k},\mathbf{k})}|\boldsymbol{\theta}^{(k,k')}) \equiv \sum_{i,j}^{N^{(k)},N^{(k')}} u^{(k,k')}(r_{i,j}^{(k,k')}|\boldsymbol{\theta}^{(k,k')}) \tag{E.10}$$

for cross interactions, we can then reduce the expressions in equation E.8 to pair-density integral expressions given by

$$\boldsymbol{\nabla}_{\boldsymbol{\theta}^{(A,A)}} \langle \ln P(\mathbf{R}^{(\mathbf{A})}, \mathbf{R}^{(\mathbf{B})}|\boldsymbol{\theta})\rangle_{P_{\text{tgt}}(\mathbf{R}^{(\mathbf{A})},\mathbf{R}^{(\mathbf{B})})} = \pi\rho^{(A)}N^{(A)} \int drr[g^{(A,A)}(r|\boldsymbol{\theta}^{(A,A)}) - g_{\text{tgt}}^{(A,A)}(r)]\boldsymbol{\nabla}_{\boldsymbol{\theta}^{(A,A)}}\beta u^{(A,A)}(r|\boldsymbol{\theta}^{(A,A)}) \tag{E.11a}$$

$$\boldsymbol{\nabla}_{\boldsymbol{\theta}^{(B,B)}} \langle \ln P(\mathbf{R}^{(\mathbf{A})}, \mathbf{R}^{(\mathbf{B})}|\boldsymbol{\theta})\rangle_{P_{\text{tgt}}(\mathbf{R}^{(\mathbf{A})},\mathbf{R}^{(\mathbf{B})})} = \pi\rho^{(B)}N^{(B)} \int drr[g^{(B,B)}(r|\boldsymbol{\theta}^{(B,B)}) - g_{\text{tgt}}^{(B,B)}(r)]\boldsymbol{\nabla}_{\boldsymbol{\theta}^{(B,B)}}\beta u^{(B,B)}(r|\boldsymbol{\theta}^{(B,B)}) \tag{E.11b}$$

$$\boldsymbol{\nabla}_{\boldsymbol{\theta}^{(A,B)}} \langle \ln P(\mathbf{R}^{(\mathbf{A})}, \mathbf{R}^{(\mathbf{B})}|\boldsymbol{\theta})\rangle_{P_{\text{tgt}}(\mathbf{R}^{(\mathbf{A})},\mathbf{R}^{(\mathbf{B})})} = 2\pi\rho^{(A)}\rho^{(B)}V \int drr[g^{(A,B)}(r|\boldsymbol{\theta}^{(A,B)}) - g_{\text{tgt}}^{(A,B)}(r)]\boldsymbol{\nabla}_{\boldsymbol{\theta}^{(A,B)}}\beta u^{(A,B)}(r|\boldsymbol{\theta}^{(A,B)}) \tag{E.11c}$$

where dummy position coordinate r indicates the separation between a pair of particles, V indicates system volume, $N^{(k)}$ indicates particle component number, $\rho^{(k)}$ corresponding component number density, and $g^{(k,k')}(r)$ indicate radial distribution functions. Finally, plugging back each corresponding gradient above into eq. E.6 and absorbing all constants in front of each integral as $\alpha^{(k,k')}$, we obtain the parameter update protocol shown as eq. 6.1 in chapter 6.

Appendix F

Additional Results for Chapter 2

F.1 Competing Flag-point Lattices Illustration

In addition to the discussion for competing lattices in chapter 2, we provide a graphical representation in figure F.1 of the Bravais chemical potential contour map as a function of aspect ratio b/a and θ for the pair potential with $\Delta\mu = 0.23$. Inset shows the primitive vectors $\mathbf{v}_1$ and $\mathbf{v}_2$ for a general oblique lattice. Note that here $|\mathbf{v}_2| \equiv 1$. Selected lattices with their corresponding values of $\{b/a, \theta\}$ are denoted by markers. These are triangular (red triangle) $\{1, \pi/3\}$, rectangular(blue diamond–value arbitrary) $\{1.17, \pi/2\}$ and squares (green squares). Square arises multiple times due to the combinatorial redundancy when picking lattice vectors as an oblique primitive (e.g $\{1, \pi/2\}$,$\{\sqrt{2}, \pi/4\}$ etc.). Further note that, as expected from the inverse design process, the square sits at the minimum of the countor plot where it appears.

F.2 Pair Potential Parameters

Tables F.2 and F.3 shows the optimized parameters found for the pair potential function $\phi(r/\sigma)$ for the different accessible values of $\Delta\mu$ used in the

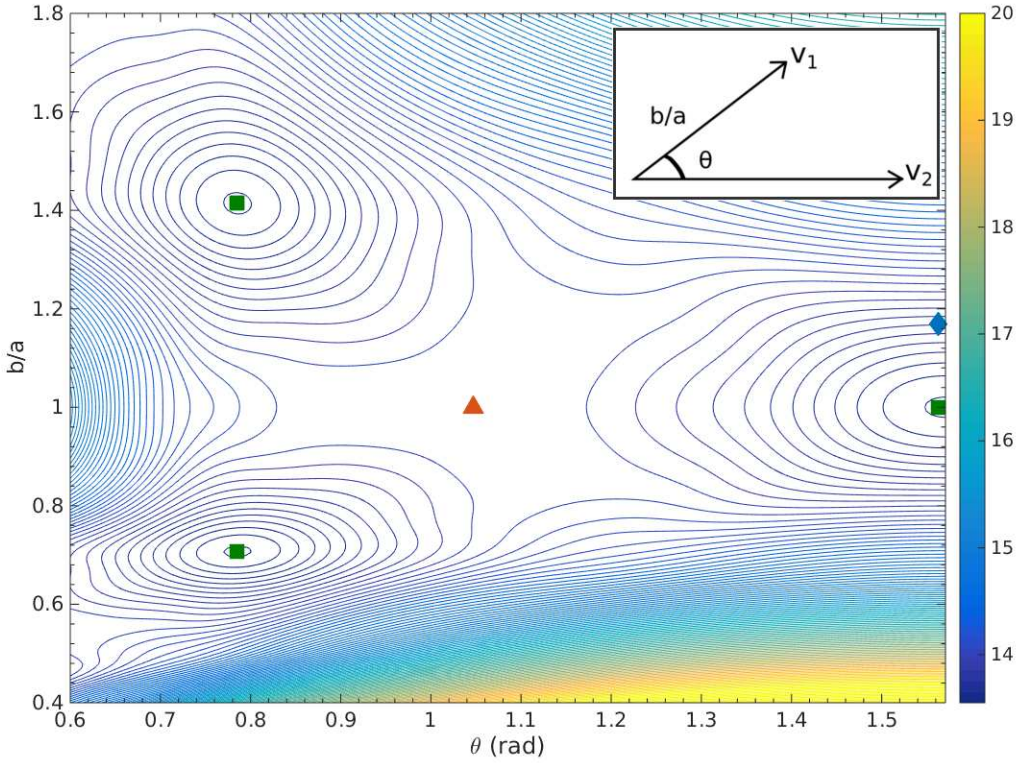

Figure F.1: Chemical potential hypersurface for the Bravais lattice space

inverse design optimization. The potential equation is reproduced below for convinience:

$$\phi(r/\sigma) = \epsilon\{A(r/\sigma)^{-n} + \sum_{i=1}^{2} \lambda_i(1 - \tanh[k_i(r/\sigma - \delta_i)]) + f_{\text{shift}}(r/\sigma)\}H[(r_{\text{cut}} - r)/\sigma]. \tag{F.1}$$

where, σ and ϵ represent characteristic length and energy scales respectively; H is the Heaviside function; $\{A, n, \lambda_i, k_i, \delta_i\}$ are variable parameters, one of which is fixed to ensure $\phi(1) = \epsilon$; r_{cut} is a cut-off radius; and f_{shift} is a polynomial

function of the form $f_{\text{shift}}(r/\sigma) = Px^2 + Qx + R$).

Table F.1: Parameters A and n in $\phi(r/\sigma)$ for different values of $\Delta\mu$

$\Delta\mu$	A	n
0.01	1.1780300	1.7339486
0.04	18.8368434	0.4139247
0.08	3.6544971	1.6881068
0.12	1.7998767	2.8502033
0.16	0.4733474	5.6498762
0.20	0.3853030	6.3785155
0.22	0.1303351	9.6080826
0.23	0.1285017	9.6708850

Table F.2: Parameters l_1,k_1,d_1,l_2,k_2, and d_2 in $\phi(r/\sigma)$ for different values of $\Delta\mu$

$\Delta\mu$	l_1	k_1	d_1	l_2	k_2	d_2
0.01	0.5935303	3.0989433	0.9883350	0.0172194	8.5116789	1.6248183
0.04	-0.0713643	7.2925317	1.3612001	0.0261070	17.9213641	1.0607134
0.08	0.0744250	12.9607205	1.0732352	-0.1943232	4.3827881	1.3322616
0.12	0.3725751	7.1452368	1.0699322	-0.3855424	3.7650882	1.1773588
0.16	-2.3035656	5.1146780	1.1441346	2.8409792	5.0919703	1.1134338
0.20	-2.6753780	5.9413689	1.1281355	3.2237088	5.9500826	1.1065381
0.22	0.2236629	13.7675604	1.1230241	0.5246589	8.4653226	0.9803159
0.23	0.2008297	14.6996242	1.1257123	0.5278173	8.4995375	0.9894431

F.3 Fractional Chemical Potential Coordination Shell Values for Selected Lattices and Potentials

Below we provide coordination shell percentage contribution ($100 \times \mu_{i,l}/\mu_l$) for selected competing lattices using the $\Delta\mu = 0.01$ and $\Delta\mu = 0.23$

Table F.3: Parameters P, Q and R from the f_{shift} shift function in $\phi(r/\sigma)$

$\Delta\mu$	P	Q	R
0.01	-0.1368124	0.8409185	-1.4886581
0.04	-0.7553436	5.8756495	-22.8620452
0.08	-0.3942355	2.4699420	-4.4910442
0.12	-0.1765871	1.0185800	-1.5760138
0.16	-0.0162226	0.0850948	-0.1141791
0.20	-0.0091145	0.0471725	-0.0621800
0.22	-0.0004694	0.0023403	-0.0029432
0.23	-0.0004450	0.0022174	-0.0027869

optimized pair potentials. In all cases, the pressure is equal to that of the target square-lattice structure at $\rho_{t,o} = 1.39$. Note in particular, the increase for second shell contributions for REC-1.17 and ET-1.17 as consistent with our $\psi(r)$ analysis in the main text.

Table F.4: Values of $\mu_{i,l}/\mu_l$ for optimized potentials $\Delta\mu = 0.01$ and $\Delta\mu = 0.23$ and selected lattices up to the third shell.

	$\Delta\mu = 0.01$			$\Delta\mu = 0.23$		
	1st	2nd	3rd	1st	2nd	3rd
Square	61.5	30.5	5.4	83.2	16.2	5.5×10^{-2}
Triangular	83.9	12.8	3.2	99.7	0.25	4.4×10^{-2}
ET-1.23	47.5	23.9	16.8	63.8	26.2	9.8
REC-1.17	33.8	27.9	29.9	59.6	31.3	9.0

Appendix G

Additional Results for Chapter 4

G.1 Truncated Hexagonal Special Competitors

As discussed in the Methods section of chapter 4, we illustrate special truncated hexagonal competitors that emerged during the optimization process in figures G.1 and G.2.

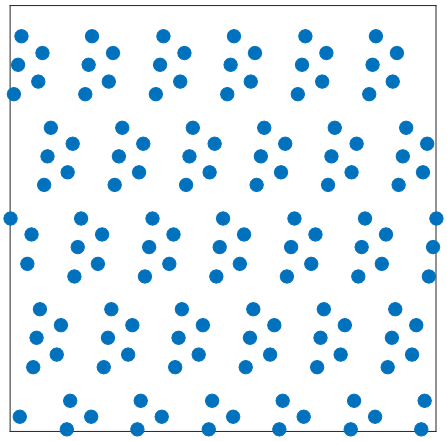

Figure G.1: Special truncated hexagonal competitor consisting of a 5 particle 'cluster' in an oblique lattice

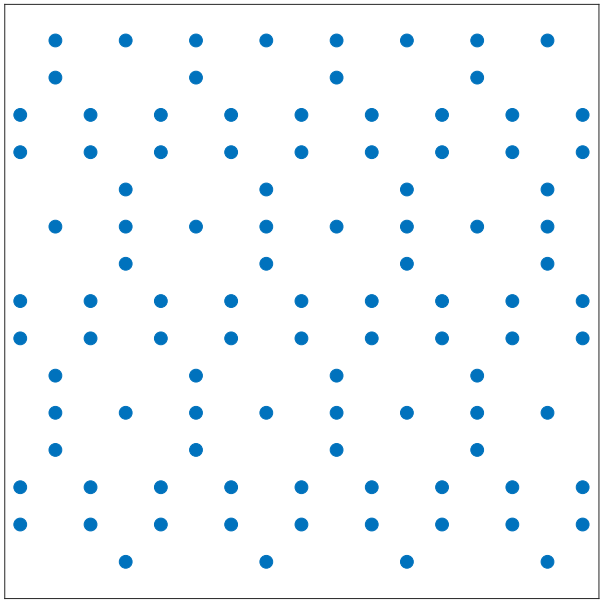

Figure G.2: Special truncated hexagonal competitor consisting of an open decagonal motif with a particle located in the center

G.2 Pair Potential Parameters Optimized for Truncated Square and Truncated Hexagonal Lattice

We list the potential parameters of $\phi(r)$ (see eq. 4.1 in chapter 4) that maximize the stability (as described in the main text) of truncated square and truncated hexagonal crystal structures. These are listed separately as the parameters of the soft repulsive component and cut off radius and the coefficients of the quadratic components of f_{shift} in G.1. The second table G.3 lists the values of λ_i, k_i, d_i in the tanh expression up to the appropriate N_i term.

Table G.1: Parameters A, n, r_{cut} for the convex repulsive pair potential $\phi(r)$ found to favor truncated square (TS) or truncated hexagonal (TH) respectively.

	A	n	r_{cut}
TS	3.44873×10^{-6}	33.447496	3.085443
TH	2.94536×10^{-7}	28.078127	4.0

Table G.2: Parameters λ_i, k_i, d_i for the convex repulsive pair potential $\phi(r)$ found to favor truncated square (TS - $N_i = 2$) or truncated hexagonal (TH - $N_i = 3$) respectively.

	λ_1	k_1	d_1	λ_2	k_2	d_2
TS	2.5	0.831795	1.081669	0.015697	6.357929	2.584218
TH	0.314171	2.447687	1.686265	0.149364	30.0	1.259423

G.3 Truncated Hexagonal Monte Carlo Quench Run

Shown in figure G.3 are the Monte Carlo runs of 24 identical seeded crystal systems over approximately 4.6 million Monte Carlo steps as discussed in the methods section of chapter 4. Configuration energy in units of ϵ.

Table G.3: Continued parameters λ_i, k_i, d_i from table G.3

	λ_3	k_3	d_3
TS	-	-	-
TH	0.047484	30.0	2.472233

Table G.4: Same as table G.1 but for polynomial parameters P, Q, R.

	P	Q	R
TS	-0.218537	1.625857	-3.108286
TH	-0.00009071	0.00076271	-0.00160711

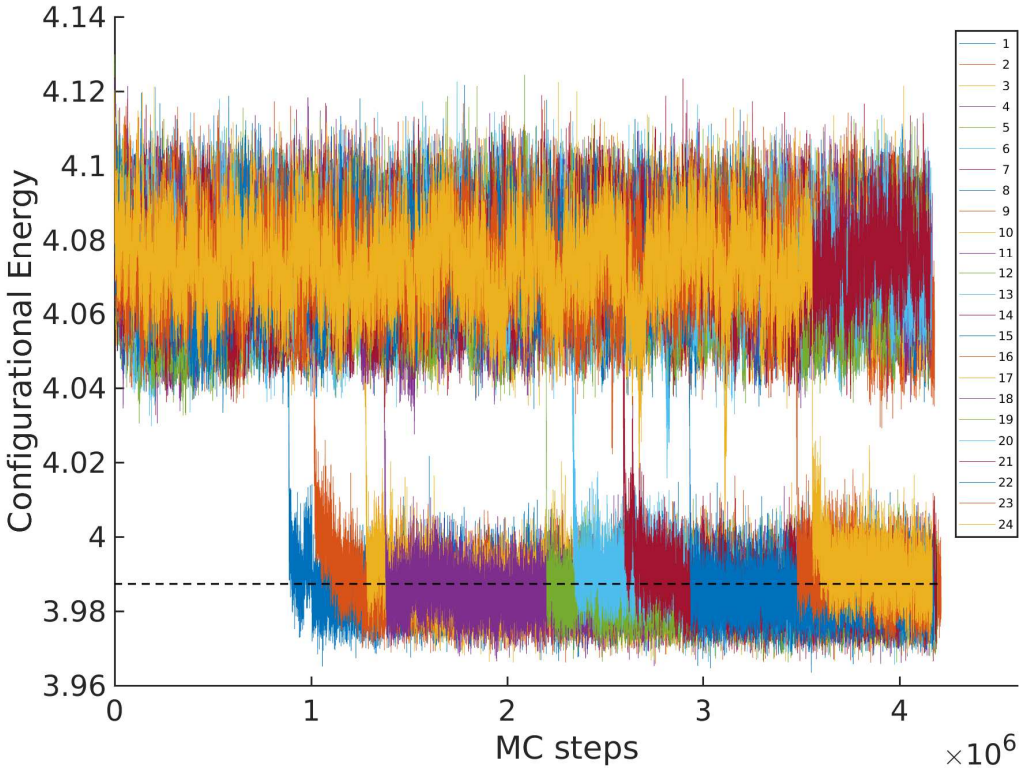

Figure G.3: Monte Carlo quench runs of 24 identical systems using a small frozen crystal seed at $T = 0.06$. Crystallized runs shown sequentially for clarity (15-24). Black dashed line indicates average configuration energy for a perfect crystal at the same temperature.

Appendix H

Additional Results for Chapter 5

H.1 Special Lattice Competitors for Honeycomb and Kagome Ground State Design Targets

As discussed in the Methods section of chapter 5, we illustrate special honeycomb and kagome competitors that emerged during the optimization process in figures H.1 and H.2 below.

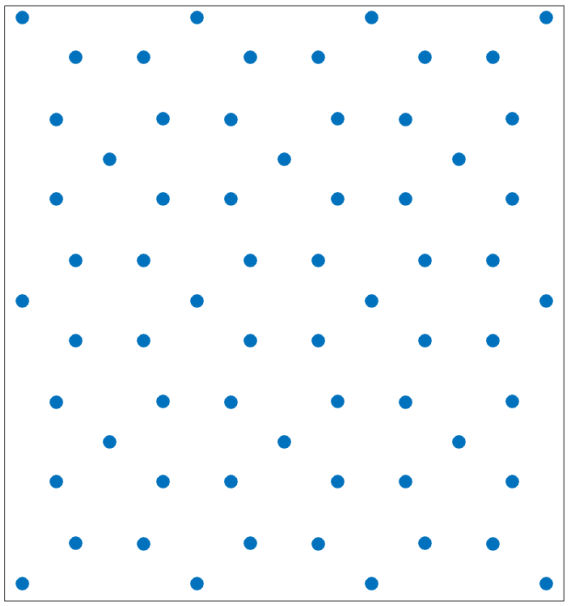

Figure H.1: Special competitor for the design of the honeycomb lattice target. Note that this crystal can be characterized as rows of elongated triangular motifs staggered so as to create intermediate 'pentagonal' motifs between them.

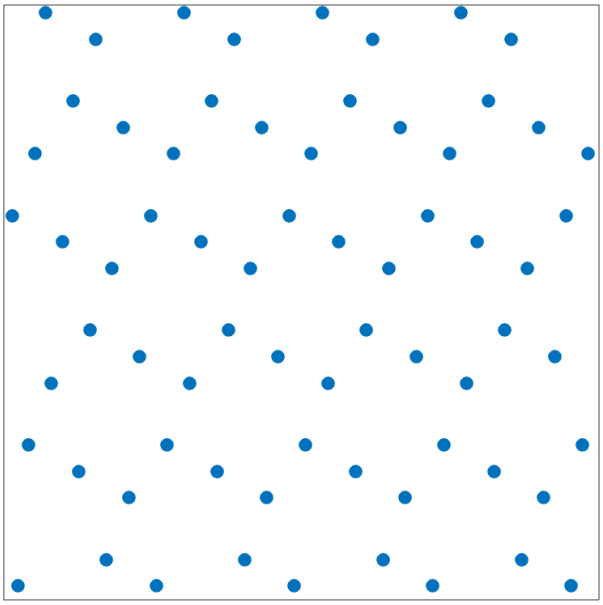

Figure H.2: Special competitor for the design of the kagome lattice target. This crystal resembles a bricked pattern with particles positioned at the outline of each 'brick'. Note further that the 'brick' rows can be related naturally to a kagome lattice row by orthogonalizing the cell from its usual 60° inclination

H.2 Pair Potential Parameters Optimized for the Square, Honeycomb and Kagome Lattices from the Ground state method

We list the potential parameters of $\phi(r)$ (see eq. 5.1 in chapter 5) that maximize the stability of the square, honeycomb and kagome crystal structures. These are listed separately as the parameters of the soft repulsive component, the cut off radius in table H.1 and the coefficients of the quadratic components of f_{shift} in H.4. The tables in H.2 - H.3 list the values of B_i, r_i, σ_i in the exp expressions.

Table H.1: Parameters $A, n, \sigma_0, r_{\text{cut}}$ for the convex repulsive pair potential $\phi(r)$ found to favor square, honeycomb and kagome respectively at density $\rho = 1.22$. Minimum positions r_{min} were fixed at 0.905357,1.375846,1.685060 for square, honeycomb and kagome corresponding to the first, second and third coordination shell for each lattice respectively.

	A	n	σ_0	r_{cut}
Square	2.50683	16.192980	0.457063	1.4624765
Honeycomb	7.28842×10^{-3}	20.071347	1.105417	1.5152092
Kagome	1.12196	8.8883046	0.379738	1.9960410

Table H.2: Parameters B_i, r_i, σ_i for the convex repulsive pair potential $\phi(r)$ found to favor square, honeycomb and kagome.

	B_1	r_1	σ_1
Square	-4.308569	1.376916	0.472360
Honeycomb	-4.290190	1.901628	0.598765
Kagome	-4.389501	1.595781	0.218255

Table H.3: Remaining parameters B_i, r_i, σ_i for the convex repulsive pair potential $\phi(r)$ found to favor square, honeycomb and kagome.

	B_2	r_2	σ_2
Square	0.245501	1.417995	0.0685170
Honeycomb	-1.432023	1.368413	0.0645997
Kagome	0.07949805	1.311123	0.1323579

Table H.4: Parameters P, Q, R for polynomial term in the convex repulsive pair potential $\phi(r)$ for all targets above.

	P	Q	R
Square	-12.072094	35.164883	-21.599134
Honeycomb	16.990788	-45.967663	33.479133
Kagome	18.270237	-75.490356	78.041919

Appendix I

Additional Results for Chapter 6

I.1 Determining the ranges of optimized pair interactions

The pair separation cut offs for AA, AB, and BB interactions that constrain their respective ranges in the optimizations were initially set to span a finite but large number of coordination shells depending on the openness and complexity of the target lattice. If satisfactory assembly was not achieved, this range was increased. However, if assembly was achieved during the initial optimization, then the cut offs for the interactions were individually reduced to include one less coordination shell in a subsequent optimization. This process was repeated until a minimum number of coordination shells spanned equally by all interaction types for successful target lattice assembly was established. At that point, individual interaction ranges were reduced in subsequent optimizations by a single coordination shell, leaving the other cut offs fixed, until a minimum number of coordination shells was determined for each interaction. As an example, for the triangular honeycomb binary lattice, all interaction ranges were initially set to span five coordination shells, but this number was reduced to two coordination shells after a few successful optimizations. Individual interaction ranges were then independently reduced in subsequent runs.

In the end, we found that successful assembly of this lattice could be achieved with cutoffs that included one and two coordination shells for the AA and BB interactions, respectively. The cross interaction cut off was chosen to span the largest number of coordination shells of individual component self interactions (in this case, two).

I.2 Global Target Assembly from Single Component Interactions

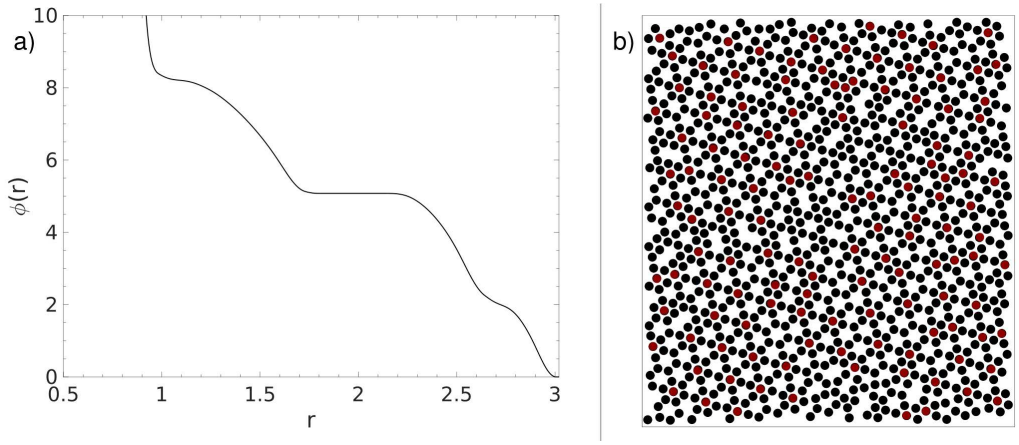

Figure I.1: Single component optimization with global triangular honeycomb as the target structure. The resulting interaction is shown in a) and the corresponding particle self-assembly from the fluid state shown in b). Particles with six neighbors have been colored to aid comparison with the correct local triangular lattice spanned by the A component in the binary structure.

As argued in chapter 6, stabilizing a global structure featuring two distinct lattice sites is more easily achieved with a binary system whose components independently occupy each such site. Such natural portioning then leads to simpler component interactions than those from a single component

system achieving the same equivalent global structure. An example of this argument is shown in figure I.1 where we show the interaction obtained from a single component system optimized to stabilize the triangular honeycomb structure from the main text. As seen in a), the potential displays numerous shoulder features that span a total of five target shells. The corresponding particle assembly, with particles displaying six neighbors colored for contrast, is shown in b). Clearly, while the 'honeycomb' matrix is visible throughout the system, the additional 'triangular' ordering from particles occupying the second site is highly defective. Increasing the optimized interaction range to span as many as nine coordination shells, known to be necessary for other complex single component systems, does not improve ordering and results in assemblies comparable to that shown in figure b). As such, this result provides a substantive example of a single-component system largely failing to stabilize a target that is easily achieved by a binary system using much simpler pair interactions.

I.3 Additional Optimization Results for WCA-like Fixed Interactions

In figure I.2 we show the resulting assemblies when one of the components was fixed to display a WCA-like potential for the STH target. Note that while global assembly fails, local structure can be seen for the non-fixed component such as in a) where BB interactions are optimized and promote assembly of the expected clusters (see Fig. 6.6(middle) in chapter 6) while the A

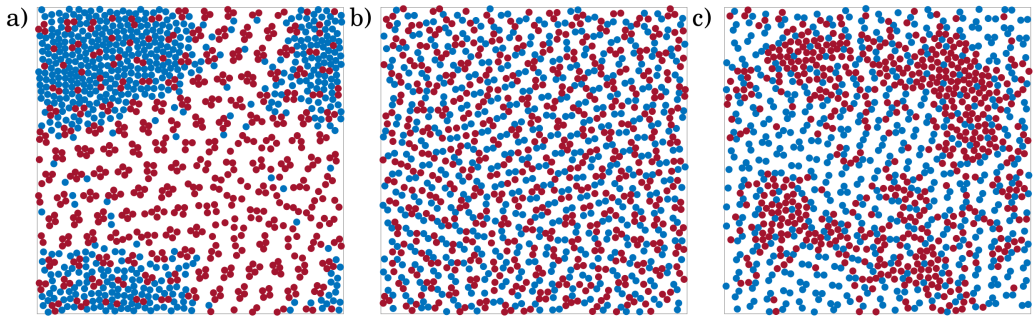

Figure I.2: Assemblies for square truncated hexagonal target (see figure 6.6 bottom in main chapter) where a) AA, b) AB , or c) BB interactions have been fixed to display a simple WCA-like repulsion form while the remaining interactions are fully optimized. Target assembly is not achieved in any of these cases.

component, whose interaction is fixed, simply phase separates. A similar case applies to c) while b) highlights that coupling is necessary for global assembly despite both A and B having optimized self interactions.

I.4 Using Single Component Interactions to Boost Binary Stability

As elaborated in the main text, it is possible to use a pair potential designed to stabilize a lattice in a single component system and replace it for a component interaction that forms the equivalent local lattice in the full binary system. We carried this out for the square binary, where the AA and BB interactions where replaced by the equivalent single component, square lattice forming interaction while keeping the optimized AB interaction for both systems. Equilibrium binary system assembly was then carried out from the fluid state. As seen in figure I.3, replacement of the AA and BB interactions with

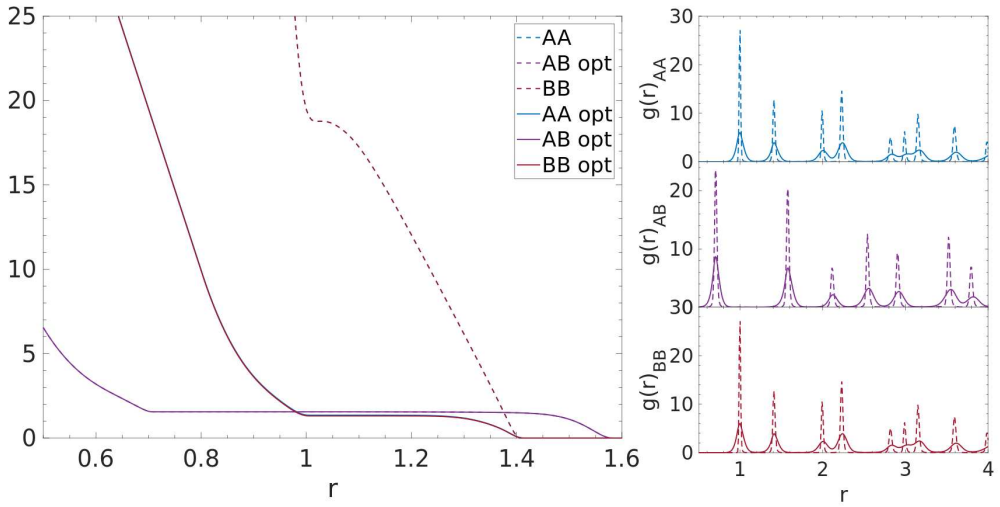

Figure I.3: Potentials for the fully optimized square binary system (solid lines) and an equivalent system but with AA and BB interactions replaced for the single component square lattice forming potential (dashed). Note that potentials AA and BB are identical by symmetry, while the AB opt interactions are kept the same in both systems. Y axis shown in reduced units. The resulting cross and self radial distribution functions for all interactions are compared on the right.

a square lattice forming potential led to dramatic increase in overall binary crystal configurational stability (much sharper peaks in the radial distribution functions). These results therefore directly demonstrate that self interactions can in principle assume the ideal single component forming potential, but need not reach these ideal limits to achieve the full binary system assembly. Instead, as explained in chapter discussion, the local interactions only need to encode necessary local lengthscales while the coupled interactions drive the larger system into the proper global configuration.

I.5 Example of how a Binary System can Assemble a Target Lattice with Simpler Optimized Interactions

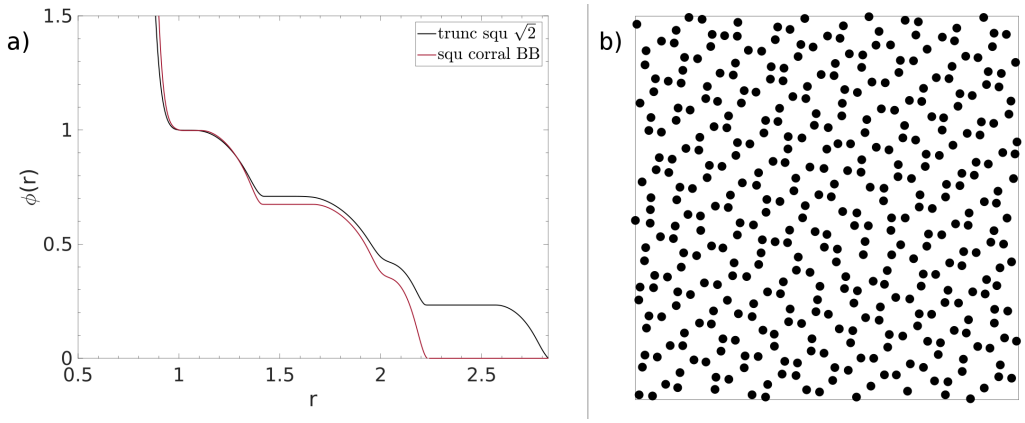

Figure I.4: a)Potentials for the BB square corral interaction (red) and the single component interaction (black) that forms the equivalent local stretched truncated square structure with side ratio $b/a = \sqrt{2}$. Potentials are re-scaled such that $\phi(r)/\phi(1) = 1$. b) Single component particle assembly from the fluid state using the optimized interaction in a).

We provide one example demonstration here for how interactions optimized to assemble a target lattice from a binary system can be simpler than those from a single-component material. We look specifically at the square corral target whose B component forms a stretched truncated square ($b/a = \sqrt{2}$) lattice as its local structure. As shown in figure I.4 a), while for the binary square corral system the equivalent truncated square ordering could be achieved with an interaction spanning four coordination shells, the equivalent single component system required five (i.e. a longer ranged interaction). Additionally, the resulting assembly from the single component system using the longer ranged interaction displayed poorer assembly than the coupled, two-

component counterpart. We expect similar results for other complex targets, like STH, whose local A component target is a more challenging stretched truncated square $b/a \sim 3.15$, but the optimized AA interaction still only needed to span three coordination shells in the binary system to achieve satisfactory assembly.

Bibliography

[1] Fan Li, David P. Josephson, and Andreas Stein. Colloidal assembly: The road from particles to colloidal molecules and crystals. *Angewandte Chemie International Edition*, 50(2):360–388, 2011.

[2] Michael A. Boles, Michael Engel, and Dmitri V. Talapin. Self-assembly of colloidal nanocrystals: From intricate structures to functional materials. *Chemical Reviews*, 116(18):11220–11289, 2016. PMID: 27552640.

[3] Alexey Victorov. Molecular thermodynamics of soft self-assembling structures for engineering applications. *Journal of Chemical Technology and Biotechnology*, 90:1357, 2015.

[4] Stefano Sacanna, David J. Pine, and Gi-Ra Yi. Engineering shape: the novel geometries of colloidal self-assembly. *Soft Matter*, 9:8096–8106, 2013.

[5] Kellar Autumn, Yiching A. Liang, S. Tonia Hsieh, Wolfgang Zesch, Wai Pang Chan, Thomas W. Kenny, Ronald Fearing, and Robert J. Full. Adhesive force of a single gecko foot-hair. *Nature*, 405:681, 2000.

[6] Kellar Autumn, Metin Sitti, Yiching A. Liang, Anne M. Peattie, Wendy R. Hansen, Simon Sponberg, Thomas W. Kenny, Ronald Fearing, Jacob N.

Israelachvili, and Robert J. Full. Evidence for van der waals adhesion in gecko setae. *Proceedings of the National Academy of Sciences*, 99(19):12252–12256, 2002.

[7] Bala Murali Venkatesan and Rashid Bashir. Nanopore sensors for nucleic acid analysis. *Nature Nanotechnology*, 6:615–624, 2011.

[8] David Roll, Joanna Malicka, Ignacy Gryczynski, Zygmunt Gryczynski, and Joseph R. Lakowicz. Metallic colloid wavelength-ratiometric scattering sensors. *Analytical Chemistry*, 75(14):3440–3445, 2003. PMID: 14570195.

[9] Adrian M. Horgan, Jonathan D. Moore, James E. Noble, and Graham J. Worsley. Polymer- and colloid-mediated bioassays, sensors and diagnostics. *Trends in Biotechnology*, 28(9):485 – 494, 2010.

[10] G Q Max Lu and Xiu Song Zhao. *Nanoporous Materials: Science and Engineering*, volume 4 of *Series on Chemical Engineering*. Imperial College Press, 2004.

[11] Helmut Bnnemann, Werner Brijoux, Rainer Brinkmann, Thomas Jouen, Barbara Korall, and Eckard Dinjus. Formation of colloidal transition metals in organic phases and their application in catalysis. *Angewandte Chemie International Edition in English*, 30(10):1312–1314, 1991.

[12] Evelyn Auyeung, William Morris, Joseph E. Mondloch, Joseph T. Hupp, Omar K. Farha, and Chad A. Mirkin. Controlling structure and porosity

in catalytic nanoparticle superlattices with dna. *Journal of the American Chemical Society*, 137:1658–1662, 2015.

[13] Russell E. Morris and Paul S. Wheatley. Gas storage in nanoporous materials. *Angewandte Chemie*, 47:4966–4981, 2008.

[14] O. D. Velev, T. A. Jede, R. F. Lobo, and A. M. Lenhoff. Porous silica via colloidal crystallization. *Nature*, 389:447, 1997.

[15] A. Luque and A. Marti. Photovoltaics: Towards the intermediate band. *Nature Photonics*, 5:137–138, 2011.

[16] Pete Vukusic and John Sambles. Photonic structures in biology. 424:852–5, 09 2003.

[17] R. Armiento, B. Kozinsky, M. Fornari, and G. Ceder. Screening for high-performance piezoelectric using high-throughput density functional theory. *Physical Review B*, 84:014103, 2011.

[18] Y. Xia, B. Gates, Y. Yin, and Y. Lu. Monodispersed colloidal spheres: Old materials with new applications. *Advanced Materials*, 12(10):693–713, 2000.

[19] Alberto Comin and Liberato Manna. New materials for tunable plasmonic colloidal nanocrystals. *Chem. Soc. Rev.*, 43:3957–3975, 2014.

[20] Costas M. Soukoulis and Martin Wegener. Past achievements and future challeneges in the development of three-dimensional photonic metmamaterials. *Nature Photonics*, 5:523–530, 2011.

[21] Shandra J. Corbitt, Mathieu Francour, and Bart Raeymaekers. Implementation of optical dielectric metamaterials: A review. *Journal of Quantitative Spectroscopy & Radiative Transfer*, SelfAssemblyPerspective158:3–16, 2015.

[22] Md Muntasir Hossain and Min Gu. Fabrication methods of 3d periodic metallic nano/microstructures for photonics applications. *Laser Photonics Reviews*, 8:233–249, 2014.

[23] Sumeet Walia, Charan M. Shah, Philipp Gutruf, Hussein Nili, Dibakar Roy Chowdhury, Withawat Withayachumnankul, Madhu Bhaskaran, and Sharath Sriram. Flexible metasurfaces and metamaterials: A review of materials and fabrication processes at micro- and nano-scales. *Applied Physics Reviews*, 2(1):011303, 2015.

[24] George M. Whitesides and Bartosz Grzybowski. Self-assembly at all scales. *Science*, 295(5564):2418–2421, 2002.

[25] Jie Zhang, Erik Luijten, and Steve Granick. Toward design rules of directional janus colloidal assembly. *Annual Review of Physical Chemistry*, 66:581–600, 2015.

[26] Qin Li, Ulrich Jonas, X. S. Zhao, and Michael Kappl. The forces at work in colloidal self-assembly: a review on fundamental interactions between colloidal particles. *Asia-Pacific Journal of Chemical Engineering*, 3(3):255–268, 2008.

[27] C. Wang, Carrie Siu, Jun Zhang, and Jiye Fang. Understanding the forces acting in self-assembly and the implications for constructing three-dimensional(3d) supercrystals. *Nano Research*, 8:2445, 2015.

[28] C. N. Likos. Effective interactions in soft condensed matter physics. *Physics Reports*, 348:267, 2001.

[29] N. Osterman, D. Babič, I. Poberaj, J. Dobnikar, and P. Ziherl. Observation of condensed phases of quasiplanar core-softened colloids. *Phys. Rev. Lett.*, 99:248301, Dec 2007.

[30] A. Yethiraj and A. van Blaaderen. A colloidal model system with an interaction tunable from hard sphere to soft and dipolar. *Nature*, 421:513, 2003.

[31] A. Yethiraj. Tunable colloids: control of colloidal phase transitions with tunable interactions. *Soft Matter*, 3:1099, 2007.

[32] Z. Zhang and Sharon C. Glotzer. Self-assembly of patchy particles. *Nano Letters*, 4:1407–1413, 2004.

[33] Moritz Antlanger, Gnther Doppelbauer, and Gerhard Kahl. On the stability of archimedean tilings formed by patchy particles. *Journal of Physics: Condensed Matter*, 23(40):404206, 2011.

[34] D. Zeb Rocklin and Xiaoming Mao. Self-assembly of three-dimensional open structures using patchy colloidal particles. *Soft Matter*, 10:7569–7576, 2014.

[35] Emanuela Bianchi, Ronald Blaak, and Christos N. Likos. Patchy colloids: state of the art and perspectives. *Phys. Chem. Chem. Phys.*, 13:6397–6410, 2011.

[36] Qian Chen, Sung Chul Bae, and Steve Granick. Directed self-assembly of a colloidal kagome lattice. *Nature*, 469:381–384, 2011.

[37] Ching-Wen Liao, Yeh-Sheng Lin, K. Chanda, Yen-Fang Song, and M. H. Huang. Formation of diverse supercrystals from self-assembly of a variety of polyhedral gold nanocrystals. *Journal of the American Chemical Society*, 135:2684, 2013.

[38] Pablo F. Damasceno, Michael Engel, and Sharon C. Glotzer. Predictive self-assembly of polyhedra into complex structures. *Science*, 337:453–456, 2012.

[39] Jaime A. Millan, Daniel Ortiz, Greg van Anders, and Sharon C. Glotzer. Self-assembly of archimedean tilings with enthalpically and entropically patchy polygons. *ACS Nano*, 8(3):2918–2928, 2014. PMID: 24483709.

[40] Yiyong Mai and Adi Eisenberg. Self-assembly of block copolymers. *Chem. Soc. Rev.*, 41:5969–5985, 2012.

[41] Samson A. Jenekhe and X. Linda Chen. Self-assembly of ordered microporous materials from rod-coil block copolymers. *Science*, 283(5400):372–375, 1999.

[42] Brad M. Rosen, Christopher J. Wilson, Daniela A. Wilson, Mihai Peterca, Mohammad R. Imam, and Virgil Percec. Dendron-mediated self-assembly, disassembly, and self-organization of complex systems. *Chemical Reviews*, 109(11):6275–6540, 2009. PMID: 19877614.

[43] Meijiao Liu, Yicheng Qiang, Weihua Li, Feng Qiu, and An-Chang Shi. Stabilizing the frank-kasper phases via binary blends of ab diblock copolymers. *ACS Macro Letters*, 5(10):1167–1171, 2016.

[44] Timothy M. Gillard, Sangwoo Lee, and Frank S. Bates. Dodecagonal quasicrystalline order in a diblock copolymer melt. *Proceedings of the National Academy of Sciences*, 113(19):5167–5172, 2016.

[45] Yiyong He, Zhibo Li, Peter Simone, and Timothy P. Lodge. Self-assembly of block copolymer micelles in an ionic liquid. *Journal of the American Chemical Society*, 128(8):2745–2750, 2006. PMID: 16492063.

[46] Stephan Kubowicz, Jean-Franois Baussard, Jean-Franois Lutz, Andreas F. Thnemann, Hans von Berlepsch, and Andr Laschewsky. Multicompartment micelles formed by self-assembly of linear abc triblock copolymers in aqueous medium. *Angewandte Chemie International Edition*, 44(33):5262–5265, 2005.

[47] Andr H. Grschel, Felix H. Schacher, Holger Schmalz, Oleg V. Borisov, Ekaterina B. Zhulina, Andreas Walther, and Axel H.E. Mller. Precise hierarchical self-assembly of multicompartment micelles. *Nature Communications*, 3:710, 2012.

[48] Adam F. Hannon, Yi Ding, Wubin Bai, Caroline A. Ross, and Alfredo Alexander-Katz. Optimizing topographical templates for directed self-assembly of block copolymers via inverse design simulations. *Nano Lett.*, 14(1):318–325, 2014.

[49] Heinrich M. Jaeger. Celebrating soft matter's 10th anniversary: Toward jamming by design. *Soft Matter*, 11:12–27, 2015.

[50] Leah K. Roth and Heinrich M. Jaeger. Optimizing packing fraction in granular media composed of overlapping spheres. *Soft Matter*, 12:1107–1115, 2016.

[51] Sean P. Paradiso, Kris T. Delaney, and Glenn H. Fredrickson. Swarm intelligence platform for multiblock polymer inverse formulation design. *ACS Macro Lett.*, 5(8):972–976, 2016.

[52] Jian Qin, Gurdaman S. Khaira, Yongrui Su, Grant P. Garner, Marc Miskin, Heinrich M. Jaeger, and Juan J. de Pablo. Evolutionary pattern design for copolymer directed self-assembly. *Soft Matter*, 9:11467–11472, 2013.

[53] Marc Z. Miskin, Gurdaman Khaira, Juan J. de Pablo, and Heinrich M. Jaeger. Turning statistical physics models into materials design engines. *Proceedings of the National Academy of Sciences*, 113(1):34–39, 2016.

[54] V. Mlinar. Utilization of inverse approach in the design of materials over nano- to macro-scale. *Annalen der Physik*, 527:187, 2015.

[55] Salvatore Torquato. Inverse optimization techniques for targeted self-assembly. *Soft Matter*, 5:1157–1173, 2009.

[56] Avni Jain, Jonathan A. Bollinger, and Thomas M. Truskett. Inverse methods for material design. *AlChE Journal*, 60:2732–2736, 2014.

[57] Fernando A. Escobed. Engineering entropy in soft matter: the bad, the ugly and the good. *Soft Matter*, 10:8388, 2014.

[58] E. Marcotte, F.H. Stillinger, and S. Torquato. unusual ground states via monotonic convex pair potentials. *Journal of Chemical Physics*, 134:164105, 2011.

[59] Avni Jain, J. R. Errington, and Thomas M. Truskett. Dimensionality and design of isotropic interactions that stabilize honeycomb, square, simple cubic and diamond lattices. *Physical Review X*, 4:031049, 2014.

[60] M. C. Rechtsman, F. H. Stillinger, and S. Torquato. optimized interactions for targeted self-assembly: applications to a honeycomb lattice. *Physical Review letters*, 95:228301, 2005.

[61] E. Edlund, O. Lindgren, and M. Nilsson Jacobi. Designing isotropic interactions for self-assembly of complex lattices. *Physical Review Letters*, 107:085503, 2011.

[62] G. Zhang, F. H. Stillinger, and S. Torquato. Probing the limitations of isotropic pair potentials to produce ground-state structural extremes via inverse statistical mechanics. *Physical Review E*, 88:042309, 2013.

[63] Masashi Torikai. Free-energy functional method for inverse problem of self assembly. *Journal of Chemical Physics*, 142:144102, 2015.

[64] Avni Jain, Jeffrey R. Errington, and Thomas M. Truskett. Inverse design of simple pairwise interactions with low-coordinated 3d lattice ground states. *Soft Matter*, 9:3866–3870, 2013.

[65] E. Marcotte, F.H. Stillinger, and S. Torquato. designed diamond ground state via optimized isotropic monotonic pair potentials. *Journal of Chemical Physics*, 138:061101, 2013.

[66] E. Edlund, O. Lindgren, and M. Nilsson Jacobi. Using the uncertainty principle to design simple interaction for targeted self-assembly. *Journal of Chemical Physics*, 139:024107, 2013.

[67] Avni Jain, Jeffrey R. Errington, and Thomas M. Truskett. Phase bevahior of materials with isotropic interactions designed by inverse strategies to favor diamond and simple cubic lattice round states. *Journal of Chemical Physics*, 139:141102, 2013.

[68] David Berber. *Bayesian Reasoning and Machine Learning*. Cambride University Press, 2012.

[69] Andrew L. Ferguson, Athanassios Z. Panagiotopoulos, Ioannis G. Kevrekidis, and Pablo G. Debenedetti. Nonlinear dimensionality reduction in molecular simulation: The diffusion map approach. *Chemical Physics Letters*, 509(1):1 – 11, 2011.

[70] W. G. Noid. Perspective: Coarse-grained models for biomolecular systems. *J. Chem. Phys.*, 139(9):090901, 2013.

[71] Joseph F. Rudzinski and W. G. Noid. Coarse-graining entropy, forces, and structures. *J. Chem. Phys.*, 135(21):214101, 2011.

[72] Aviel Chaimovich and M. Scott Shell. Coarse-graining errors and numerical optimization using a relative entropy framework. *J. Chem. Phys.*, 134(9):094112, 2011.

[73] M. Scott Shell. The relative entropy is fundamental to multiscale and inverse thermodynamic problems. *J. Chem. Phys.*, 129(14), 2008.

[74] Beth A. Lindquist, Ryan B. Jadrich, and Thomas M. Truskett. Communication: Inverse design for self-assembly via on-the-fly optimization. *The Journal of Chemical Physics*, 145(11), 2016.

[75] R. B. Jadrich, B. A. Lindquist, and T. M. Truskett. Probabilistic inverse design for self-assembling materials. *The Journal of Chemical Physics*, 146(18):184103, 2017.

[76] Beth Lindquist, Ryan Jadrich, William Pineros, and Thomas Truskett. Inverse design of self-assembling Frank-Kasper phases and insights into emergent quasicrystals. 12 2017.

[77] R. B. Jadrich, J. A. Bollinger, B. A. Lindquist, and T. M. Truskett. Equilibrium cluster fluids: pair interactions via inverse design. *Soft Matter*, 11:9342–9354, 2015.

[78] Beth A. Lindquist, Sayantan Dutta, Ryan B. Jadrich, Delia J. Milliron, and Thomas M. Truskett. Interactions and design rules for assembly of porous colloidal mesophases. *Soft Matter*, 13:1335–1343, 2017.

[79] E R Dobbs and G O Jones. Theory and properties of solid argon. *Reports on Progress in Physics*, 20(1):516, 1957.

[80] Paul L. Biancaniello, Anthony J. Kim, and John C. Crocker. Colloidal interactions and self-assembly using dna hybridization. *Physical Review Letters*, 94:058302, 2005.

[81] C. Patrick Royall, Ard A. Louis, and Hajime Tanaka. Measuring colloidal interactions with confocal microscopy. *The Journal of Chemical Physics*, 127(4):044507, 2007.

[82] Gianpietro Malescio and Giuseppe Pellicane. Stripe patterns in two-dimensional systems with core-corona molecular architecture. *Physical Review E*, 70:021202, 2004.

[83] Michael Grnwald and Phillip L. Geissler. Patterns without patches: Hierarchical self-assembly of complex structures from simple building blocks. *ACS Nano*, 8(6):5891–5897, 2014. PMID: 24816138.

[84] Mirjam E. Leunissen, Christina G. Christova, Antti-Pekka Hynninen, C. Patrick Royall, Andrew I. Campbell, Arnout Imhof, Marjolein Dijkstra, Ren van Roij, and Alfons van Blaaderen. Ionic colloidal crystals of oppositely charged particles. *Nature*, 437:235–240, 2005.

[85] Elena V. Shevchenko, Dmitri V. Talapin, Nicholas A. Kotov, Stephen O'Brien, and Christopher B. Murray. Structural diversity in binary nanoparticle superlattices. *Nature*, 439:55–59, 2005.

[86] Xingchen Ye, Chenhui Zhu, Peter Ercius, Shilpa N. Raja, Bo He, Matthew R. Jones, Matthew R. Hauwiller, Yi Liu, Ting Xu, and A. Paul Alivisatos. Structural diversity in binary superlattices self-assembled from polymer-grafted nanocrystals. *Nature*, 6:10052, 2015.

[87] E. A. Jagla. Phase behavior of a system of particles with core collapse. *Phys. Rev. E*, 58:1478–1486, Aug 1998.

[88] E.A. Jagla. Minimum energy configuraions of repelling particles in two dimensions. *Journal of Chemical Physics*, 110:451, 1999.

[89] A. Scala, M. Reza Sadr-Lahijany, N. Giovambattista, S. V. Buldyrev, and H.E. Stanley. Waterlike anomalies for core-softened models of fluids: Two-dimensional systems. *Physical Review E*, 63:041202, 2000.

[90] M. Scott Shell. *Thermodynamics and Statistical Mechanics: An Integrated Approach*. Cambridge University Press, 2015.

[91] Santi Prestipino, Franz Saija, and Gianpietro Malescio. The zero-temperature phase diagram of soft-repulsive particle fluids. *Soft Matter*, 5:2795–2803, 2009.

[92] GAMS Development Corporation. General Algebraic Modeling System (GAMS) Release 24.2.3. Washington, DC, USA, 2015.

[93] Joseph O. Hirschfelder, Charles F. Curtiss, and R. Byron Bird. *Molecular Theory of Gases and Liquids*. John Wiley & Sons, 1954.

[94] P. Belotti, J. Lee, L. Liberti, F. Margot, and A. Waechter. Branching and bounds tightening techniques for non-convex minlp. *Optimization Methods & Software*, 24(4-5):597–634, 2009.

[95] BONMIN. http://www.gams.com/dd/docs/solvers/bonmin.pdf, last retrieved 8/29/2014.

[96] A. Wächter and L. T. Biegler. On the implementation of an interior-point filter line-search algorithm for large-scale nonlinear programming. *Mathematical programming*, 106(1):25–57, 2006.

[97] A.B. Belonoshko, N.V. Skorodumova, A. Rosengren, and B. Johansson. Melting and critical superheating. *Physical review E*, 73:012201, 2006.

[98] A.B. Belonoshko, S.Davis, N.V. Skorodumova, P.H. Lundow, A. Rosengren, and B. Johansson. Properties of the fcc lennard-jones crystal model at the limit of superheating. *Physical review B*, 76:064121, 2007.

[99] D. Alfe, C. Cazorla, and M.J. Gillan. the kinetics of homogenous melting beyond the limit of superheating. *the journal of chemical physics*, 135:024102, 2011.

[100] J. Bouchet, F. Bottin, G. Jomard, and G. Zerah. melting curve of aluminum up to 300 gpa obtained through ab initio molecular dynamics simulations. *Physical Review B*, 80:094102, 2009.

[101] Sheng-Nian Luo, Alejandro Strachan, and Damian C. Swift. Nonequilibrium melting and crystallization of a model lennard-jones system. *Journal of Chemical Physics*, 120:11640, 2004.

[102] Sheng-Nian Luo, Thomas J. Ahrens, Tahir Cagin, Alejandro Strachan, William A. Goddard, and Damian C. Swift. Maximum superheating and undercooling: Systematics, molecular dynamics simulations, and dynamic experiments. *Physical Review B*, 68:134206, 2003.

[103] William D. Piñeros, Michael Baldea, and Thomas M. Truskett. Breadth vs depth: Interactions that stabilize particle assemblies to changes in density and temperature. *Journal of Chemical Physics*, 144:084502, 2016.

[104] Daniel Salgado-Blanco and Carlos I. Mendoza. Non-additive simple potentials for pre-programmed self-assembly. *Soft Matter*, 11:889–897, 2015.

[105] John E. Greedan. Geometrically frustrated magnetic materials. *J. Mater. Chem.*, 11:37–53, 2001.

[106] Manuel Pereiro, Dmitry Yudin, Jonathan Chico, Corina Etz, Olle Eriksson, and Anders Bergman. Topological excitations in a kagome magnet. *Nature Communications*, 5:4815, 2014.

[107] Robert D. Batten, David A. Huse, Frank H. Stillinger, and Salvatore Torquato. Novel ground-state crystals with controlled vacancy concen-

trations: From kagome to honeycomb to stripes. *Soft Matter*, 7:6194–6204, 2011.

[108] William D. Piñeros, Michael Baldea, and Thomas M. Truskett. Designing convex repulsive pair potentials that favor assembly of kagome and snub square lattices. *Journal of Chemical Physics*, 145:054901, 2016.

[109] William D. Piñeros and Thomas M. Truskett. Designing pairwise interactions that stabilize open crystals: Truncated square and truncated hexagonal lattices. *The Journal of Chemical Physics*, 146(14):144501, 2017.

[110] J. Chihara and M. Ishitobi. Effective interatomic interactions in liquid metals. *Molecular Simulation*, 12(3-6):187–195, 1994.

[111] Minseok Song, Yajun Ding, Hasan Zerze, Mark A. Snyder, and Jeetain Mittal. Binary superlattice design by controlling dna-mediated interactions. *arXiv:1703.03465*, 2017.

[112] Johannes Bisschop and Alexander Meeraus. On the Development of a General Algebraic Modeling System in a Strategic Planning Environment. In *Applications*, volume 20 of *Mathematical Programming Studies*, pages 1–29. Springer Berlin Heidelberg, 1982.

[113] GAMS Development Corporation, Washington, DC, USA. *GAMS - A User's Guide, GAMS Release 24.2.3*, 2015.

[114] David Van Der Spoel, Erik Lindahl, Berk Hess, Gerrit Groenhof, Alan E. Mark, and Herman J. C. Berendsen. Gromacs: Fast, flexible, and free. *Journal of Computational Chemistry*, 26(16):1701–1718, 2005.

[115] Steve Plimpton. Fast parallel algorithms for short-range molecular dynamics. *Journal of Computational Physics*, 117(1):1 – 19, 1995.

[116] William D. Piñeros, Ryan B. Jadrich, and Thomas M. Truskett. Design of two-dimensional particle assemblies using isotropic pair interactions with an attractive well. *AIP Advances*, 7(11):115307, 2017.

[117] Minseok Song, Yajun Ding, Hasan Zerze, Mark A. Snyder, and Jeetain Mittal. Binary superlattice design by controlling dna-mediated interactions. *Langmuir*, 0(0):null, 0. PMID: 29111738.

[118] Nathan A. Mahynski, Hasan Zerze, Harold W. Hatch, Vincent K. Shen, and Jeetain Mittal. Assembly of multi-flavored two-dimensional colloidal crystals. *Soft Matter*, 13:5397–5408, 2017.

[119] Alexei V. Tkachenko. Generic phase diagram of binary superlattices. *Proceedings of the National Academy of Sciences*, 113(37):10269–10274, 2016.

[120] Avi Ben-Simon, Hagai Eshet, and Eran Rabani. On the phase behavior of binary mixtures of nanoparticles. *ACS Nano*, 7(2):978–986, 2013. PMID: 23281700.

[121] Alex Travesset. Binary nanoparticle superlattices of soft-particle systems. *Proceedings of the National Academy of Sciences*, 112(31):9563–9567, 2015.

[122] Branko Grunbaum and G.C. Shepard. *Tilings and Patterns*. W.H. Freeman and Company, 1987.

[123] William D. Piñeros, Beth A. Lindquist, Ryan B. Jadrich, and Thomas M. Truskett. Inverse design of multicomponent assemblies. *The Journal of Chemical Physics*, 148(10):104509, 2018.

[124] Stephen Mann. Self-assembly and transformation of hybrid nano-objects and nanostructures under equilibrium and non-equilibrium conditions. *Nature Materials*, 8:781, 2009.

[125] Daniel L. Purich and David Kristofferson. Microtubule assembly: A review of progress, principles, and perspectives. volume 36 of *Advances in Protein Chemistry*, pages 133 – 212. Academic Press, 1984.

[126] Marc Kirschner and Tim Mitchison. Beyond self-assembly: From microtubules to morphogenesis. *Cell*, 45:329, 1986.

[127] Dilip Kondepudi, Bruce Kay, and James Dixon. End-directed evolution and the emergence of energy-seeking behavior in a complex system. *Phys. Rev. E*, 91:050902, May 2015.

[128] W. A. Lopes. Nonequilibrium self-assembly of metals on diblock copolymer templates. *Phys. Rev. E*, 65:031606, Feb 2002.

[129] Job Boekhoven, Wouter E. Hendriksen, Ger J. M. Koper, Rienk Eelkema, and Jan H. van Esch. Transient assembly of active materials fueled by a chemical reaction. *Science*, 349(6252):1075–1079, 2015.

[130] Michael Nguyen and Suriyanarayanan Vaikuntanathan. Design principles for nonequilibrium self-assembly. *Proceedings of the National Academy of Sciences*, 113(50):14231–14236, 2016.

[131] Jeremy L. England. Dissipative adaptation in driven self-assembly. *Nature Nanotechnology*, 10:919, 2015.

[132] Michael Grunwald, Simon Tricard, George M. Whitesides, and Phillip L. Geissler. Exploiting non-equilibrium phase separation for self-assembly. *Soft Matter*, 12:1517–1524, 2016.

[133] Mario Tagliazucchi, Emily A. Weiss, and Igal Szleifer. Dissipative self-assembly of particles interacting through time-oscillatory potentials. *Proceedings of the National Academy of Sciences*, 111(27):9751–9756, 2014.

Vita

\begin{vita}

\end{vita}

Permanent address: wdp0@utexas.edu

This dissertation was typeset with LaTeX[†] by the author.

[†]LaTeX is a document preparation system developed by Leslie Lamport as a special version of Donald Knuth's TeX Program.